DYNAMIC MODELING OF A WIND-DIESEL-HYDROGEN HYBRID POWER SYSTEM

MD. MARUF-UL-KARIM

DYNAMIC MODELING OF A WIND-DIESEL-HYDROGEN HYBRID POWER SYSTEM

by

© Md. Maruf-ul-Karim

A thesis submitted to the School of Graduate Studies in partial fulfillment of the requirements for the degree of Master of Engineering

Faculty of Engineering and Applied Science

Memorial University of Newfoundland

July 2010

St. John's Newfoundland Canada

To My Parents

Abstract

A dynamic model of Wind-Diesel-Hydrogen based system corresponding to Ramea electrical power system has been developed in this research. The literature starts with reviewing of a number of research papers similar but not same as what is accomplished by this research work. As the parts of that system, wind turbines, diesel generators, electrolyzers, hydrogen tanks and hydrogen generators have been designed in Matlab Simulink and SimPower environments. The system performances along with the sensitivity analyses have been carried out in Homer followed by the designs of constituents. Further analysis and explanations are depicted with all components in integrated form. All the simulation parameters are tabulated and the output results are portrayed in diagrams. Finally the thesis is concluded with brief summery and future scopes.

Acknowledgement

Firstly the author gratefully remembers the Almighty for being accorded all the encouragement, patience and optimism throughout the research. He would like to thank his parents and siblings for ceaseless mental support during this period.

The author is earnestly beholden to Dr. M. Tariq Iqbal for his kind supervision, inspiration and suggestions in conducting the research work. John Flynn from NL Hydro is highly appreciated for the essential perceptions and documents he provided which assisted this research significantly. The author also would like to mention the names of Howard Richards and Walter Parsons from NL hydro for their assistance. He would like to acknowledge Professor Peter Meckl from Purdue University, Maria Davies, Chris Haraldsen and Leila LaRosa from Northern Power Systems and Rene Mandeville from Hydrogenics Incorporation for thoughtful credentials that contributed the research a lot.

Finally the author is indebted to National Science and Engineering Research Council Wind Energy Strategic Network (WESNet), School of Graduate Studies Fellowship and Faculty of Engineering and Applied Science for their substantial financial supports. Furthermore, the administrative cooperation from Ms. Moya Crocker is highly acknowledged.

Table of Contents

List of Figures

List of Tables

List of Abbreviations

APU	Auxiliary Power Unit
CanWEA	Canadian Wind Energy Association
CCT	Critical Clearing Time
COE	Cost of Energy
C-Pt	Carbon Platinum Catalyst
CSPM	Constant Speed Prime Mover
DDPMSG	Direct Drive Permanent Magnet Synchronous Generator
DSP	Digital Signal Processing
DVR	Dynamic Voltage Regulator
FLC	Fuzzy Logic Controller
FRM	Fuzzy Regression Model
GHG	Green House Gas
HRI	Hydrogen Research Institute
KOH	Potassium Hydroxide
MPPT	Maximum Power Point Tracker
NiO	Nickel Oxide
NLH	Newfoundland and Labrador Hydro
NN	Neural-Net

NPC[1]	Neutral Point Clamped
NPC[2]	Net Present Cost
NRCan	Natural Resources Canada
NREL	National Renewable Energy Laboratory
P&O	Perturbation and Observation
PEMFC	Proton Exchange Membrane Fuel Cell
PMSG	Permanent Magnet Synchronous Generator
PWM	Pulse Width Modulation
RE	Renewable Energy
RESHS	Renewable Energy System with Hydrogen Storage
RFC	Regenerative or Reversible Fuel Cell
SCIG	Squirrel Cage Induction Generator
SOC	State of Charge
TCR	Thyristor Controlled Reactor
THD	Total Harmonic Distortion
TSC	Thyristor Switched Capacitor
UC	Ultra Capacitor
UPFC	Unified Power Flow Control
VSPM	Variable Speed Prime Mover
WDICS	Wind Diesel Integrated Control System
WECS	Wind Energy Conversion System
WT	Wind Turbine

List of Symbols

Wind Energy Conversion Systems

Symbols	Parameters	Units
λ	Flux induced by the permanent magnets of the rotor	V·s
φ_{ds}, φ_{qs}	Stator d and q axis fluxes	Wb
φ'_{dr}, φ'_{qr}	Rotor d and q axis fluxes	Wb
ω_m	Rotor angular velocity	rad/s
ω_r	Electrical angular velocity	rad/s
θ_m	Rotor angular position	rad
θ_r	Electrical rotor angular position	rad
E_l	Induced back EMF	V
f	Frequency	Hz
F	Combined rotor and load viscous friction coefficient	N·m·s
H	Combined rotor and load inertia constant	s
I_l	Stator current	A
i_{ds}, i'_{dr}	d-axis stator and rotor currents	A
i_{qs}, i'_{qr}	q-axis stator and rotor currents	A
I_g, I_d	Generator current and dc link current	A

J	Combined rotor and load inertia coefficient	$kg \cdot m^2$
L_{ab}	Line-line inductance	H
L_{ls}, L'_{lr}	Stator and rotor leakage inductances	H
L_m	Magnetizing inductance	H
L_s, L'_r	Total stator and rotor inductances	H
L_d, L_q	d and q axis inductances	H
n_s	Field rotation in the air-gap	rad/s
p	Number of pole pair	-
R_s, R'_r	Stator and rotor resistances	Ω
T_e	Electromagnetic torque	N·m
T_m	Shaft mechanical torque	N·m
V_1	Stator terminal voltage	V
V_{ds}, V'_{dr}	d-axis stator and rotor voltages	V
V_{qs}, V'_{qr}	q-axis stator and rotor voltages	V
V_g, V_d	Generator terminal voltage and dc link voltage	V
X_{ls}	Stator reactance	Ω

Transformer

Symbols	**Parameters**	**Units**
a	Turns ratio	-
I_{1tr}, I_{2tr}	Primary and secondary side currents	A

N_1, N_2	No. of turns of primary and secondary side coils	-
R_{1tr}, R_{2tr}	Primary and secondary side resistances	Ω
X_{1tr}, X_{2tr}	Primary and secondary side reactances	Ω

Wind Turbines

Symbols	**Parameters**	**Units**
β	Pitch angle	Deg.
λ	Tip speed ratio	-
ω	Turbine rotational speed	rad/s
ρ	Air density	kg/m^3
A	Turbine swept area	m^2
c_1 - c_6	Turbine coefficients	-
C_p	Performance coefficient of the turbine	-
C_q	Torque coefficient of the turbine	-
P_t	Mechanical power generated by the turbine	W
R	Radius of the turbine	m
T_t	Turbine torque	N·m
v_w	Wind speed	m/s

Electrolyzer

Symbols	Parameters	Units
ΔG	Gibb's energy	kJ/mol
ΔH	Change of enthalpy between reactants and products	kJ/mol
η_e	Energy efficiency	-
η_F	Faraday efficiency	-
τ_t	Thermal time constant	s
A	Area of electrodes	m^2
C_{cw}	Thermal capacity of the cooling water	J/K
C_t	Overall thermal capacity of electrolyzer	J/K
f_1	Parameters related to Faraday efficiency	mA^2/cm^4
f_2	Parameters related to Faraday efficiency	-
F	Faraday constant	-
h_{cond}	Parameters related to conduction heat transfer	W/K
h_{conv}	Parameters related to convection heat transfer	W/K/A
I	Current required for the electrolysis	A
LMTD	Log mean temperature difference	K
n_c	Number of electrolyzer cells per stack	-
$\dot{n}_{H2}$	Hydrogen production rate	mol/s
OT	Electrolyzer operating time	s
Q'_{cool}	Rate of auxiliary cooling demand	W
Q'_{gen}	Internal heat generation rate	W
Q'_{loss}	Rate of heat loss to the ambient	W

r	Parameter related to ohmic resistanceof the electrolyte	$\Omega \cdot m^2$
R_t	Overall thermal resistance of the electrolyzer	K/W
s	Over voltage coefficients on electrodes	V
t	Over voltage coefficients on electrodes	m^2/A
T	Temperature of the electrolyzer	K
T_a	Ambient temperature	K
T_{cwi}	Temperature of the inlet cooling water	K
T_{cwo}	Temperature of outlet cooling water	K
T_{ini}	Initial temperature of the electrolyzer	K
V	Cell Voltage	V
VA_{HX}	Overall heat transfer coefficient and area product of heat exchanger	K/W
V_{rev}	Reversible voltage	V
V_{tn}	Thermo neutral cell voltage	V
z	Number of electrons transferred in each reaction	-

Hydrogen Tank

Symbols	**Parameters**	**Units**
k_f	Flow constant of hydrogen	-
M_{H2}	Molar mass of hydrogen	kg/kmol
$\dot{n}_{H2}$	Hydrogen inlet flow rate	mol/s

$\dot{n}_{H2out}$	Hydrogen flow rate out of the tank	mol/s
P_b	Tank pressure at any instant	Pa
P_{bini}	Initial tank pressure	Pa
P_{H2atm}	Hydrogen pressure outside of the tank	Pa
R	Universal gas constant	J/K/mol
T_b	Operating temperature in the tank	K
V_b	Tank volume	m^3
z	Compressibility factor of hydrogen	-

Hydrogen Engine

Symbols	**Parameters**	**Units**
α	Throttle angle	Deg.
τ_d	Delay between fuel intake and torque generation	s
η_i	Thermal efficiency	-
η_{vol}	Volumetric efficiency	-
A_{eq}	Throttle opening area	m^2
c_d	Discharge coefficient	-
f	Fuel fraction in the intake manifold	-
H_L	Lower heating value of the hydrogen gas	MJ/kg
J	Effective inertia	$kg \cdot m^2$

k_{eq}	Equivalent ratio of specific heats of air-fuel mixture	-
$\dot{m}$	Rate of change of total charge mass in the intake manifold	mol/s
M_a, M_f	Molecular weight of air and fuel respectively	gm/mol
m_a, m_f	Mass of air and fuel in the intake manifold	gm
$\dot{m}_{ai}$, $\dot{m}_{fi}$	Air and fuel flow rate over throttle	mol/s
$\dot{m}_{ao}$, $\dot{m}_{fo}$	Air and fuel flow rate into cylinders	mol/s
M_{eq}	Equivalent molar weight of air-fuel mixture	gm/mol
$\dot{m}_i$	Charge flow rate over throttle	mol/s
$\dot{m}_o$	Charge flow rate from the manifold to cylinders	mol/s
n	Engine rotational speed	rpm
P_a	Partial pressure of air in the intake manifold	Pa
P_b	Peripheral load power	W
P_{ext}	External load power	W
P_f	Partial pressure of fuel in the intake manifold	Pa
P_m	Intake manifold pressure	Pa
P_0	Throttle inlet pressure	Pa
P_{pc}	Pumping power correction	W
P_{tf}	Frictional power	W
T_{amb}	Ambient temperature	K
T_i	Inlet charge temperature to the inter-cooler	K
T_m	Intake manifold temperature	K

T_o	Throttle inlet charge temperature	K
V	Manifold and port passage volume	m^3
V_d	Engine displacement	m^3

Hydrogen Generator

Symbols	**Parameters**	**Units**
$\Delta\omega$	Speed variation with respect to the speed of operation	rad/s
$\omega(t)$	Mechanical speed of rotor	rad/s
ω_n	Frequency of electromechanical oscillations	rad/s
ω_0	Speed of operation	rad/s
ω_r	Rotor rotational speed	rad/s
ω_s	Electrical frequency	rad/s
φ_d, φ_q	d and q axis fluxes	Wb
φ'_{kd}, φ'_{kq}	d and q axis damper winding fluxes	Wb
δ	Power angle	Deg.
ζ	Damping ratio	-
H	Inertia constant	s
I_{abc}	Three phase current	A
i_d, i_q	d and q axis currents	A
i'_{kd}, i'_{kq}	d and q axis damper winding currents	A
Kd	Damping factor	-

L'_{fd}, L'_{kd}	d axis field and damper winding inductances	H
L'_{kq1}, L'_{kq2}	q axis damper winding inductances	H
L_l	Leakage inductance	H
L_{md}, L_{mq}	d and q axis magnetizing inductances	H
P_{base}	Three-phase base power	W
Pm	Mechanical power	W
P_{max}	Maximum power transmitted through the reactance	W
R'_{kd}, R'_{kq}	d and q axis damper winding resistances	Ω
R_s	Stator resistance	Ω
Te, Tm	Electromagnetic and mechanical torques	N·m
V_{abc}	Three phase voltage	V
V_{baseLL}	Base line-to-line voltage	V
V_d, V_q	d and q axis terminal voltages	V
V'_{kd}, V'_{kq}	d and q axis damper winding voltages	V

Diesel Generator

Symbols	**Parameters**	**Units**
H_a, H_c	Actuator and Controller transfer functions	-
K	Regulator gain	-
T_1, T_2, T_3	Regulator time constants	s
T_4, T_5, T_6	Actuator time constants	s

Chapter 1

Introduction

1.1 Prospects of Renewable Energy Sources

The World's energy demand has increased dramatically in the past century and it is expected to grow even faster and significantly in the near future. Although today's lifestyle depends immensely on the use and existence of fossil fuels, but due to reducing resource, dependence and transition to Renewable Energy (RE) sources is of great interest. However, this is not the only reason for relying on RE sources, environmental pollution is another issue. Air pollution has become a severe problem in many developing countries. Use of Green Energy sources can also reduce the rate of global warming. Wind, solar, hydro, sea-wave, geothermal and tidal waves are some of the forms of RE sources. Energy can be extracted from these sources according to their consistent availability in certain territories. According to the records of January 2010, fossil fuels provide 66% of world's electricity and 95% of world's total energy demands including

heating, transport, electrical power generation and other uses [1]. Although they are putting adverse effect on the environment it is impossible to stop their use completely. Instead, the penetration level can be increased by exploiting more RE sources.

Like many other RE sources, Canada is blessed with adequate wind resource. Steady and strong winds blow over plenty of locations in Canada. This allows to operate the wind farms more efficiently and economically. Moreover, this country has the world's longest coast-line, second largest landmass and a low population density. As a result, Canada is in a better position than other countries to widen their wind resources. Table 1.1 [2] shows the comparison of annual mean wind speed and wind power density amongst Canada and other leading wind energy countries.

Countries	**Annual Mean Wind Speed (m/s)**	**Wind Power Density (W/m^2)**
Germany	5.5-7.0	200-400
Spain	5.5-8.0	200-600
USA	6.5-9.0	300-800
India	5.5-8.0	200-600
China	5.5-9.0	200-800
Canada	6.5-9.0	300-800

Table 1.1: Wind Quality among Different Countries in the World

Canadian Wind Energy Association (CanWEA) has fixed a target of 20 percent of total load demand to be met by wind energy by the year of 2025 which is about 55,000 MW [2]. Although Canada's present installed capacity is only 3,319 MW, it has been found that if only 0.25 percent [2] of her land mass is used for wind projects that will be able to meet the annual electrical demand of the whole country. Therefore, CanWEA's target is challenging but not unachievable.

There are many scattered islands along with remote isolated Aboriginial communities around the country who are solely depending on diesel powered electricity. In order for encouraging the RE sources, CanWEA has worked with experts and stakeholders to form a Remote Community Wind Incentive Program which would assist in two ways. Firstly, a grant will cover 5% of capital costs for wind energy projects in large cities and industries and 10% of the same for remote villages. Secondly, a power production incentive of 2 cents/kWh for large cities and industries and 10 cents/kWh for remote villages would be paid for the first 10 years of operation.

1.2 Ramea Hybrid Power System

This research focuses on wind-diesel-hydrogen hybrid power system model for a small remote island called Ramea. This island is located 10 km off the South coast of Newfoundland. Ramea is the inhabitant of about 700 people who are mostly old fishermen [3-5]. It is the place where a Wind-Diesel demonstration project has been commissioned in 2004. Before that only the diesel generators, owned and maintained by the Newfoundland and Labrador Hydro (NLH), were delivering electricity to meet the load demand. In Ramea minimum, peak and average loads are 202 kW, 1211 kW and 528 kW respectively and annual energy consumption is 4,556 MWh. The existing six wind turbines, of 65 kW each provide about 10% penetration level in the system, thus reducing the fuel cost for the diesel generators. This also results 750 tonnes/year Green House Gas (GHG) emission reduction and improving the air quality. As a novel RE project, Atlantic Innovation Fund and Natural Resources Canada (NRCan) is financing to test a new Wind

Diesel Integrated Control System (WDICS). Ramea is a wind resourceful region where the annual mean wind speed and wind energy are 7.35 m/s and 466.63 W/m^2 respectively at 30m height [6]. In order to utilize this source, three more 100 kW wind turbines have been installed and hydrogen energy storage has been added to the system. This system is still under construction and is expected to be operational in near future. Figure 1.1 [50] and 1.2 [51] reveal the geographical location and the map of Ramea respectively.

Figure 1.1: Location of Ramea in Newfoundland

Figure 1.2: Geography of Ramea Island (Satellite View)

1.3 Literature Review

Due to the adverse effects of conventional fuel as discussed above, a number of research projects have been carried out during last couple of decades. These efforts received attention when some of the RE sources proved themselves as prominent assets. But still there are some issues to consider when the RE sources are going to be introduced and operated simultaneously with the existing systems. Although there are certain control mechanisms for each of those sources, fluctuation of voltage and frequency are the main problems from the power quality point of view. Moreover, converter size and harmonics are other parameters to investigate. Some of the related recent research works [7-44] will be highlighted next.

1.3.1 Permanent Magnet Synchronous Generator Based WECS

Shuhui Li and Timothy A. Haskew [7] worked on Direct Drive Permanent Magnet Synchronous Generator (DDPMSG) and doubly fed induction generator based variable speed wind turbines. Decoupled d-q vector control approach has been applied to both the generator side converter and the grid side converters. The former converter controls the machine characteristics and the latter converter regulates the dc link voltage and the reactive power absorbed from the grid. By using transient and steady state simulations it has been established that when the impedance between the grid and the converter is purely inductive, d-axis voltage component (V_d) controls the reactive power and q-axis

voltage component (V_q) controls the active power. However, when the line impedance is a series R-L combination, V_d and V_q have contribution to both real and reactive power controls.

Feng Wu, Xiao-Ping Zhang and Ping Ju have proposed [8] different controlling scheme for back to back converters in DDPMSG based wind turbine (WT). Small signal stability analyses have been performed with and without controllers. The simulation results of dynamic responses of single machine system and four machine system are shown as stable. The Critical Clearing Time (CCT) was measured in two different cases and it was recognized that WT with DDPMSG can improve the grid connected system stability.

For a Permanent Magnet Synchronous Generator (PMSG) based WT, output power maximization process has been illustrated by T. Tafticht, K. Agbossou, A. Chériti and M.L. Doumbia [9]. Perturbation and Observation (P&O) technique was used for simulation purposes and a Buck-Boost converter was suggested to connect between the rectifier and the dc bus. This Buck-Boost converter ensures capturing the wind energy for a wide range of wind speeds and hence provides the maximum output power.

Horizontal furling control method for small PMSG based WT has been presented by Md. Arifujjaman, M. Tariq Iqbal, John E. Quaicoe and M. Jahangir Khan [10]. Aerodynamic power extraction by the WT is controlled by a mechanism called "Furling". Tip speed ratio control method and hill climbing control method were examined for maximum power capturing from wind. The authors have applied a step input from 11.5 m/s to 12.5 m/s at t=7 sec and showed that after 17 sec all the parameters came to stable

condition. By using MATLAB-SIMULINK™ comparative simulation results have been shown at the end.

Xibo Yuan, Fred Wang, Rolando Burgos, Yongdong Li and Dushan Boroyevich have performed a research on the dc-link voltage control for a PMSG based WT connected to a weak grid system [11]. Like others, the vector control method was used for generator side converter. The proposed method has been explained with a flow chart. The objective was to determine how the capacitor voltage was changing with load variation by simulation results. Finally a 1.5 kW prototype has been built and the simulation results have been verified by laboratory experiments.

The dynamic response of a stand-alone Wind Energy Conversion System (WECS) has been observed by Bogdan S. Borowy and Ziyad M. Salameh [12]. Here the system is connected with battery bank and effects of wind gust were experimented. The authors have presented the turbine model, generator model and controlled rectifier model. Programming language C++ and the MATLAB were used for simulation and those results have been compared with the values obtained by data acquisition system. It has been reported that the battery current and the generator current are the mostly affected parameters with the change of wind speed.

Shuhui Li and Tim A. Haskew have proposed another very fundamental research on PMSG based WT [13]. Maximum torque control, unity power factor control and constant stator voltage control are the possible control strategies for the generator side converter. By a comparative discussion it has been found that the third procedure has couple of more advantages than the other two. MATLAB and C++ language were used for the characteristic analyses and the following statements have been revealed. The

electromagnetic torque is linearly proportional to d-axis stator voltage (V_{sd}), but does not influenced by q-axis stator voltage (V_{sq}) at all. Keeping the d-q control constant, increment of speed causes reduction of torque. The real power characteristic is same as before but variable speed can not change the real power except for very low speed. Unlike others the reactive power is biased by both stator voltage at d-q frame (V_{s_dq}) and turbine speed. For invariable speed, the more $|V_{s\_dq}|$ will cause more absorption of the reactive power by the generator and vice versa. Furthermore, maintaining the V_{s_dq} steady, reduction of speed results in more reactive power consumption.

Different control mechanisms of multi-pole PMSG based WT have been reported by Anca D. Hansen and Gabriele Michalke [14]. The stiffness of the drive train was considered in the two-mass model which has not been shown by other research works. The damping controller has been proved by the authors to be an essential component as the generator speed and the grid power become unstable without it. The simulation tool DigSILENT was used to show how the pitch angle, generator speed, real and reactive powers were changing with the wind speed variation. It has been recommended to use the voltage controller in conjunction with the whole system such that the grid voltage and the reactive power level remain almost constant.

1.3.2 Squirrel Cage Induction Generator Based WECS

Loraind Szabo, Kairoly Agoston Biro, Cosmina Nicula and Florin Jurca have worked on 3 kW squirrel cage induction generator (SCIG) based WT in autonomous state [15]. It has been recognized that during generation of active power, the SCIG based WT cannot

produce reactive power for self excitation and as a result a capacitor bank is necessary between the generator and the load. An alternative approach has been proposed by the authors that is – instead of a capacitor bank, a PWM inverter can be used which can provide leading or lagging reactive power and at the same time it can keep the system stable in wind speed and/or load variation. Load current, output voltage, active and reactive powers were compared in no load and loaded conditions by simulation results and laboratory experiments.

A new idea of back to back Neutral Point Clamped (NPC) converter interface has been implemented by Emilio J. Bueno, Santiago Cobreces, Francisco J. Rodriguez, Alvaro Hernandez and Felipe Espinosa [16]. DSP based control mechanism has been employed to overcome the voltage dip or any other voltage imbalances in the grid. Mean phase voltage Total Harmonic Distortion (THD) of 19.5% has been reported for 3.5% of mean imbalances with this particular topology.

Yuri Ulianov Lopez and Jose Antonio Dominguez Navarro performed small signal stability analysis utilizing the Kundur's theory for grid connected constant speed WT [17]. Stability analysis toolbox in MATLAB named PSAT was used to obtain the characteristics of six Eigen values. System stability has been discussed with different values of wind speed, generated voltage and the load demand.

Adaptive interfacing and control strategies for three mostly used WT generators (DFIG, PMSG and SCIG) have been proposed by Alexander Hamlyn, Helen Cheung, Lin Wang, Cungang Yang and Richard Cheung [18]. IEEE-1547 standard has been followed for interface designing. The proposed configuration is resistant to fault condition and it is possible to monitor hundreds of feeder nodes of the distribution systems.

A novel PWM switched Dynamic Voltage Regulator (DVR) driven by a Tri-loop Dynamic Error driven PI controller was developed to improve the power quality in the distribution system and this procedure has been illustrated in the proposal of T. Aboul-Seoud and A. M. Sharaf [19]. The variation of voltage, power factor and reactive power were examined with and without DVR in this literature. Finally it has been concluded that by using the DVR the power quality can be extensively improved in the distribution network.

R. Jayashri and R.P. Kumudini Devi have claimed that the conventional FACTS controllers such as SVC or STATCOM can improve the voltage ride-through of the induction generators but incapable to damp the speed oscillations [20]. In order to alleviate this problem, the authors proposed the Unified Power Flow Control (UPFC). This UPFC comprises of shunt-series type controllers which can control various electrical parameters along with the generator speed. The experiment has been carried out with 11-bus radial system and the simulation results showed how the system active power, reactive power and the speed level have been stabilized with this specific approach.

Another approach for terminal voltage regulation of self excited induction generator has been devised in the research work by Tarek Ahmed, Osamu Noro, Eiji Hiraki and Mutsuo Nakaoka [21]. A Fixed Excitation Capacitor Bank (FC), a Thyristor Switched Capacitor (TSC), a Thyristor Controlled Reactor (TCR) along with some controllers is the main components of the intended architecture. In terms of turbine, both Constant Speed Prime Mover (CSPM) and Variable Speed Prime Mover (VSPM) have been thought-out. A feasible prototype has been built and tested in the laboratory comparing the experimental results with the simulation results. In case of VSPM with

specific torque coefficient and speed coefficient, the change in terminal voltage has been observed with the variation of terminal excitation capacitance. Comparatively with the same conditions, a very little frequency variation has been found. On the other hand, for CSPM the torque and speed coefficients were fixed at 120 Nm and 133 Nm respectively and experiments have been conducted with three different capacitor values 194μF, 244μF and 294μF. The terminal voltage was dropping with the increment of load power and the terminal voltage behaved reverse way with the rise of prime mover speed. Moreover, the terminal voltage and the frequency have been characterized with the change of excitation capacitance. The results were the terminal voltage went up with capacitance same as VSPM, but the frequency was completely independent of capacitance. The wind turbine prototype gave almost same terminal voltage characteristics as the simulated or reference one. The authors also were keen to show the change of voltage and thyristor triggering angle with inductive load disparity for different composition of SVC, sometimes with FC and TCR, sometimes FC, TSC and TCR.

1.3.3 Economic and Cost Analysis of Hybrid Energy Systems

A wind-hydrogen hybrid energy system for a remote isolated load has been described in [22]. D.A. Bechrakis, E.J. McKeogh and P.D. Gallagher have considered a wind resourceful island near Northeastern Greece for conducting their investigation. In this research the load demand represents the energy consumed by a 10-room typical hotel. The whole year has been divided into high season and low season according to apparent existence of the visitors and the weather conditions. Being the main energy source, the

time series wind data has been computed near to the northern Aegean Sea for the wind turbines. For this region the Weibull distribution parameters have been found as k = 1.96 and c = 7.69. Westwind^{TM} 20 kW wind turbine has been generating power to the system. It has been reported that storing the produced hydrogen by a high pressure electrolyzer in gaseous form at ambient pressure is more convenient than storing it by low pressure electrolyzer with a compressor set and at higher pressure. Moreover, Cost and economic assessment have been carried out with two scenarios; one with 8 kW electrolyzer and 600 Nm^3 hydrogen tank and another with 6 kW electrolyzer and 900 Nm^3 tank. These arrangements were simulated in conjunction with wind turbine and fuel cell of similar capacities. The later mentioned set has been proved to ensure the cheapest electricity cost for that hotel that is $1.05/kWh.

Hybrid energy storage system performance was investigated with a model comprising of a photovoltaic electric generation system with combined hydrogen and battery energy storage [23]. S.R. Vosen and J.O. Keller made a comparison between battery and hydrogen based storage systems in their research. System performance with individual and combined storage technique has also been illustrated. Battery state of charge (SOC) and neural-net (NN) based control system have been adopted which were programmed to learn over time to use system resources more efficiently by adjusting the energy storage strategy to variations in power production and demand. Hydrogen can be stored in gas phase, liquid phase or in metal hydride form and it has been examined that H_2 storage costs one seventh for the same amount of energy storage in battery. However, it has been proved that combining a battery with a hydrogen energy storage in the proposed system using NN control can significantly reduce the storage cost even lower

than either a hydrogen-only or a battery-only storage device. Although the NN control and SOC control result in the same distributed generation efficiency, the former one can make a cost saving of storage components around 30% over the latter mentioned algorithm.

Wind-PV-Fuel Cell based hybrid power system simulated in HOMER has been planned by Mohammad Saad Alam and David W. Gao [24]. The control scheme of the power flow was also designed by the authors. The results showed that the fraction of power generations from PV array, WT and the FC system were respectively 29.29%, 70.15% and 0.56%. Unmet Load and Capacity Shortage are expected to be as low as possible for a well designed system and the figures found in this proposal were only 254 kWh/Yr and 368 kWh/Yr.

1.3.4 Operation and Performance of Hybrid Energy Systems

Optimum power management in a hybrid power system is very imperative for remote regions where no grid connection is possible. Wind, solar with battery storage topology is so far common approach. More recently hydrogen has been proved as better storage medium over the battery system in some points. Kodjo Agbossou, Mamadou L. Doumbia and Adil Anouar have proposed such a hybrid RE power system where the hydrogen production efficiency was improved [25]. After determining the characteristics of WT and electrolyzer systems, controlling of the buck converter was intended; this was placed between the dc bus and the electrolyzer. A numerical control multiphase technique was developed and programmed in the processor to control this converter in such a way that

required amount of energy can be flown towards the electrolyzer which is in turn related to hydrogen production efficiency. This proposal contains two case studies in terms of DC bus voltage level. When the bus voltage was around 55V, the electrolyzer operated with adequate current resulting good hydrogen production efficiency. On the contrary, when the bus voltage was below 50V, the current became smaller and the electrolyzer ran with poor efficiency during the initial operating hours. The designed electrolyzer efficiency ranges from 60% to 65%, where the same of buck converter varies from 92% to 96%. It has also been experimented that the performance of hydrogen production and storage gets better with higher power levels.

Nowadays wind-diesel hybrid system has received profound attraction compared to other alternative RE sources for remote island communities. Due to the high energy conversion efficiency and low installation and operational ($/kWh) cost more and more research works are being executed in this arena. Tomonobu Senjyu, Eitaro Omine, Daisuke Hayashi, Hideomi Sekine and Toshihisa Funabashi have worked on the decentralized controllers to reduce the fluctuation of frequency, terminal voltage and hydrogen volume [26]. In the proposed system a 20 MW diesel generator and a 4 MW WT supply power to 10 MW load. Aqua electrolyzer and the fuel cell system have been utilized to ensure system stability. Decentralized control systems of all components have been conferred along with the singular value plots. The authors modeled a centralized controller aside of decentralized controllers and showed that if the communication delay is ignored, both the controllers would provide the same stability to the system. However, in other instance 18ms time delay was considered for centralized controller resulting unstable condition, the voltage exceeded the maximum allowable range (5%) and

frequency too lost its consistency. Since the decentralized controllers have been placed near each facility, there was no time delay for them and could retain the stability.

A small wind-fuel cell hybrid energy system has been proposed by M.J. Khan and M.T. Iqbal [27]. The model developed by the authors comprised a WT, a fuel cell, an electrolyzer, an ultra-capacitor, a power converter and PID controllers. Dynamic simulation model of each component has been generated by MATLAB SIMULINK™. The simulation results showed how the voltage, current, power and pressure were deviating with the corresponding input change. In the 48V system voltage variation has been ranged from 43V to 65V. In order to maintain the stability, suitable controllers and power electronic mechanisms have been suggested.

A simple and low-priced regenerative solution to perform preliminary analysis on Photo Voltaic and Proton Exchange Membrane Fuel Cell (PV-PEMFC) has been examined by Vincenzo Cataliotti, Giorgio Graditi and Giuseppe Scrivano [28]. Anode pressure and external temperature have been studied to realize their effects on system performance. It has been found that the external temperature had the significant effect compared to the anode pressure. In order to validate the miniaturized (6W) hybrid model, temperature should be kept between 10 ^{o}C to 40 ^{o}C. With the obtained simulation results, it has been decided that this model could be the cheaper way to conducting experiments for the larger hybrid systems.

An Integrated and automated hydrogen based small Auxiliary Power Unit (APU) has been presented by Guillaume Doucet, Claude Etievant, Christophe Puyenchet, Serguey Grigoriev, Pierre Millet [29]. According to the scheme the wind or solar energy is being used to power the remote community and the surplus energy is stored in the form

of metal hydride. If the RE deficit occurs the stored hydrogen will be used to generate electricity. Electrolyzer and fuel cell were projected to hydrogen (H_2) production and hydrogen usage functionality. Both of them were Proton Exchange Membrane (PEM) types. Maximum H_2 flow rate by electrolyzer and maximum output power of FC have been recorded as 1 Nm^3/hr and 1 kW respectively. All the metal hydrides discussed here have the same isothermal thermodynamic characteristics. The H_2 system has been manufactured by "Kurchatov Institute" in Moscow and has stationary applications as well as hydrogen refueling station for scooters.

Th.F. El-Shatter, M.N. Eskandar and M.T. El-Hagry have planned about a simple PV/Electrolyzer/Fuel Cell hybrid system which can be utilized for delivering energy at night or pumping for irrigation [30]. The Maximum Power Point Tracker (MPPT) proposed by the authors has been made based on Fuzzy Regression Model (FRM). A control system was employed which could monitor the state of the system and disperse the energy and H_2 flow. The whole system has been modeled by MATLAB SIMULINK™ and results have been computed in four different seasons of the year. During the winter the least amount of power was reported due to small solar insolation. The output voltage – current density profile has been pointed in the proposal as well.

Electrolyzer is a device used to split the bonding of water (H_2O) and produce hydrogen (H_2) and oxygen (O_2) electrochemically. The produced O_2 can be used for life support, in fuel cells, sustainable energy systems and usage of H_2 can be for corrosion control, gas chromatograph sensors, metal forming, welding etc. Very few applications use both the H_2 and O_2 which are more than 99% pure. Most of the cases this H_2 is in use with renewable sources, refueling stations and other industrial applications too. Therefore

Electrolyzers are often called the H_2 Generators. Depending on the water inlet position the electrolyzers are classified in anode feed and cathode feed type systems. Since the anode feed technology has been adopted by industries and become popular in military sectors, hence this particular type PEM electrolyzer has been studied by Haluk Görgün [31]. Anode ancillary, cathode ancillary, membrane ancillary, voltage ancillary and storage ancillary are presented with successful modeling. Finally the dynamic performances such as bottle pressure, hydrogen flow over time have been shown in simulation results.

Nowadays the most remarkable example of H_2 refueling station is the Munich Airport. The FMG, Munich Airport operating company, is trying to enhance the use of alternative fuels. Recently the first E85 bio-ethanol station has been launched for business. A number of ramp vehicles in the FMG fleet have already been converted to run on the new fuel [32]. This is the electrolyzer which essentially produces H_2. Although there have been some major research concentration on PEM electrolyzers, but their cost is still too high compared to the Alkaline type Electrolyzers and more research is demanded to cut the cost down. Being subjective with simple working principle and cost competitiveness of latterly mentioned electrolyzer, Øystein Ulleberg has presented a comprehensive dynamic model with simulation results [33]. This research work has been carried out based on the PHOBUS plant in Jűlich whose operating pressure is 7 bar and temperature is up to 80 °C. The extensive behavior of this electrolyzer has been explained by thermodynamic, electrochemical and thermal models. In order to realize the inherent characteristics the comparison between a variable current electrolyzer and a fixed current electrolyzer has been made. The fixed current electrolyzer exhibited more frequent on/off

switching. As a consequence low average run time, less H_2 production, less year-end H_2 pressure in the storage have been found. In contrast, in a solar-H_2-battery system the variable current electrolyzer drew a large fraction of current from the PV array to run itself and minimized the battery usage. Battery discharging energy has been reduced up to 50% by employing the variable current electrolyzers.

A straight forward dynamic simulation of a hybrid power system has been studied in [34] by Hung-Cheng Chen, Jian-Cong Qiu and Chia-Hao Liu. Very simple models of solar cell, wind turbine, electrolyzer, fuel cell and ultra capacitor have been presented. The transient behaviors of generated powers, currents and voltages were depicted with the change of load and resource availability.

A Fuzzy Logic Controller (FLC) based wind-solar-hydrogen-battery based hybrid power system has been proposed by A. Bilodeau and K. Agbossou [35]. Several objectives have been emphasized in this literature. First, reduction of energy transfer from the short term storage (battery) to the long term storage (hydrogen) or vice versa was ensured. Second, limiting the abusive use of the batteries, i.e. they were constrained to be discharged too deeply or for long time in order to increase their life time. The input variables of the FLC are net power flow and battery state of charge (SOC) and the output variable is power set point. The FLC is designed in such a way that when the output is positive, the set point is sent to the boost converter causing the fuel cells to start. On the other hand, when the output is negative, the set point is sent to the buck converter and electrolyzer will start. Furthermore, if the set point value is less than 500 W both the fuel cell and the electrolyzer will be stopped. It has been described showing simulation results

that the FLC was functioning well by switching the electrolyzer and the fuel cell appropriately and keeping the SOC of battery more than 50% all the time.

Generating a novel power flow controller, a PV/FC/UC hybrid power system has been offered by M. Uzunoglu, O.C. Onar and M.S. Alam [36]. For a stand alone micro-grid system, PV alone can not be the solution because the solar insolation is available at day time only. However sometimes odd weather during the day results inadequate irradiation. In order to meet the load consistently, FC and UC have been introduced to the main system along with a precise main controller. The dynamic behavior of this system has been experimented based on real world data.

Chun-Hua Li, Xin-Jian Zhu, Guang-Yi Cao, Sheng Sui and Ming-Ruo Hu have worked on stand-alone PV system with hybrid energy storage technique [37]. Addition to observing the dynamic behaviors, sizing optimization and cost analysis has been explained too. The proposed system comprises of solar cells, fuel cells, electrolyzer cells, hydrogen compressor, storage and battery. With the discussion of energy management strategy, it has been intended to ascertain the minimal system configuration. Three different combinations of components have been chosen for performing a comprehensive comparison. Out of PV/battery, PV/FC and PV/FC/battery hybrid systems, the latest mentioned system proved itself more potential in terms of cost and efficiency.

Similar kind of strategy of modeling the hybrid power system and computing the dynamic characteristics have been followed by Mamadou Lamine Doumbia, Kodjo Agbossou and Évelyne Granger [38]. This research work dealt with the real time data of wind speed, solar insolation and load consumption in the months of January and July. Wind, solar, electrolyzer and fuel cell powers along with the dc bus current were

simulated. Finally the authors validated the results by Hydrogen Research Institute (HRI) test bench.

Equivalent circuit approach has been employed for modeling of variable speed WT, hydrogen based hybrid power system [39]. The researchers of this plan, R. Chedid, F. B. Chaaban and R. Shihab were dealing with 1.5 kW BWC permanent magnet synchronous generator based WT, 1 kW Stuart Electrolyzer and 1 kW PEM Fuel Cell. The average load was approximated as 80 W and the wind speed was considered changing between 10 m/s to 25 m/s. The WT was modeled based on power coefficient versus tip speed ratio curve and the generator was designed with the help of park transformation. Moreover, both the electrolyzer and the fuel cell have been replaced by the equivalent circuits consist of a DC voltage sources and a linear resistances. The hydrogen tank volume was imagined as large as to accommodate any amount of hydrogen. Component currents, hydrogen production and consumption and power generation and demand have been analyzed by simulation results. Although the proposed system configuration is quite simple, the amount of unmet load in certain period is unexpectedly high.

Another thought has come out from O.C. Onar, M. Uzunoglu and M.S. Alam regarding the generation of hybrid power system [40]. Besides modeling the WT, electrolyzer, FC, UC and hydrogen tank, a robust an extensive control strategy has been discussed in this literature. Wind generator output voltage and frequency are of fluctuating nature. The FC/UC system also delivers irregular amplitude DC voltage. In order to get the fixed DC voltage, power conditioning is essential. A 12-pulse AC/DC Thyristor controlled double bridge rectifier was used with the WT output and a Boost

DC/DC converter was used with the FC/UC system output. The DC bus voltage is maintained at 400V and the generated power was further fed to the load through 5 kHz IGBT PWM inverters. The simulation results showed that the load demand had been met appropriately by the combined system.

A Renewable Energy System with Hydrogen Storage (RESHS) has been illustrated with dynamic models of each component [41]. Both the battery and the hydrogen were used for energy storage application. A ten-stage simulation algorithm has been developed. The model validation has been done with more realistic residential energy consumption scenario. The electrolyzer and the fuel cell operations have been regulated by the energy levels of the battery. The authors have set the threshold values for experimental observations. In such instance the electrolyzer would be operating when the battery energy is ranging from 7.7 kWhr to 8.25 kWhr. On the other hand, the fuel cell would operate while this level lied between 7.15 kWhr to 7.7 kWhr. Thus the research work ensures the energy flow associated with the load demand effectively.

Regenerative or Reversible Fuel Cell (RFC) system operation as a part of hybrid power system has been outlined in [42]. This novel approach has been established by James D. Maclay, Jacob Brouwer and G. Scott Samuelsen where the objective was to sizing the PV based system so that it can handle the load aptly. The RFC has been illustrated as a single electrode pair device which is bi-functional, i.e. it works both as fuel cell mode and electrolyzer mode. This arrangement has the similarity with rechargeable batteries too. Different size combinations of components have been observed how they perform feeding the residential load. Both the stand alone and grid connected operations were examined too. Finally the authors concluded that the system

with 2 kW fuel cell and 7.3 kW electrolyzer connected with the grid would increase the fuel cell efficiency by 16% and total system efficiency by 26%. The lead acid batteries have mere impact on system performance.

A small 500 W wind/fuel cell hybrid energy system has been presented by M.T. Iqbal [43]. According to the proposal the wind turbine was characterized by a transfer function. The modeling of electrolyzer, fuel cell and controllers has been discussed precisely. System responses have been analyzed by employing different loads and wind speeds.

A comprehensive control scheme for a two generator power plant system has been developed in [44]. Alejandro J. del Real, Alicia Arce and Carlos Bordons have demonstrated the model consisting of two generating units. The PV served as the primary source whereas the FC ran as the secondary source. The control strategy has got the key importance in the literature. Depending on the electricity cost, grid capacity, hydrogen storage capacity and desired solar radiation, two-level control algorithm was proposed. Grid power, radiation and stored hydrogen are the first level input parameters. On the other hand, power consumed by the electrolyzer, power generated by the fuel cell, fuel cell stacks and the switch states are the input references to the second level. The first two has been noted as continuous and the rest two have been referred to as the discrete references. In order to reduce the complexity of the nonlinear model, power conditioning devices have been overlooked. Finally it has been proved that the outputs followed the reference inputs as expected with two reference power levels.

Above literature reviews reveal that some of the research are converged outlining the control mechanisms, fault recovery and dynamic performances of wind turbines, some

of them elucidate the individual dynamic behavior of each component of different configured hybrid energy systems. In fact none of them has appended wind speed responsive WECS modeling as covered in this research. No literature constitutes Wind-Diesel-Hydrogen based hybrid energy system simulation results and how the conventional and green energy sources take part in fulfilling the load demand. However, economic aspects of such hybrid energy system and the cost analyses have been found inanimate in the above recounted research works.

1.4 Scope of this Research

Ramea is a wind resourceful island in Newfoundland, Canada and presently the energy demand is met by the Wind-Diesel system only. No storage mechanism has been employed so far. However, a dump load is introduced to handle the over energy production condition. In order to exploit wind resource properly, three more wind turbines have already been installed on site. Instead of using conventional battery storage system, energy is planned to be stored in the form of hydrogen. Therefore, electrolyzers and hydrogen generators along with the hydrogen storage tanks are soon going to be added to the existing system. This study contains interpretation of dynamic behaviors of each component of Ramea hybrid power system and their combined response while connected to 4.16 kV AC bus. The overall infrastructure of Ramea power system is depicted with simple blocks in Figure 1.3.

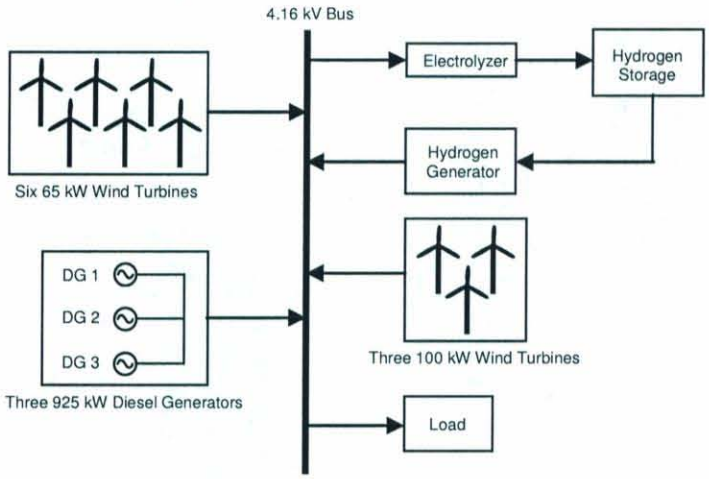

Figure 1.3: Block Diagram of Ramea Hybrid Power System.

HOMER [45] is used for sizing of components of hybrid energy systems. Besides the cost analysis, several electrical issues can be revealed by this tool. As the Wind-Diesel system is already operating and further modifications will be executed very shortly, power system sizing has got the less priority. This research is emphasizing on examining the electrical behaviors of sources and load characteristics such as energy production, excess electricity, unmet load, capacity shortage, renewable fraction, capacity factor of each WT, wind penetration, green house gas emissions etc. The cash flow analysis and system cost summary can be highlighted as well. However, sensitivity analysis is another feature of HOMER tool and performed by various primary loads, wind speed and diesel price data.

Before establishing the dynamic behaviors of the combined system, the steady state models are developed. By using Matlab/Simulink^{TM} and SimPower block-sets, a number of mathematical and empirical expressions are implemented for this purpose. These generated models are intended to operate such that their characteristics match with

the manufacturers' specification sheets. Finally they are connected to a 4160V AC bus and their responses are observed by varying wind speed and consumed load.

1.5 Thesis Organization

This literature is comprised of six chapters. Following the introductory annotations and the whole power system overview in Chapter 1, anticipations on the electrical performances are made based on HOMER simulations and sensitivity analyses in Chapter 2. After that the steady state models of both types of wind energy conversion systems are generated. The electrical power output from the generators are perceived corresponding to each wind speed. A comparative discussion is made regarding the examined power curve and the power curve provided by the manufacturing companies in Chapter 3. Hydrogen storage correlates to the electrolyzer and the hydrogen generator systems. In Chapter 4 the partial dynamic natures of these components are expounded. At the last stage, the WECS, diesel generator, electrolyzer, storage tanks, hydrogen generators and loads are combined and their dynamic responses are analyzed in Chapter 5. The culminating remarks, contribution and future experimentations are delineated in Chapter 6.

The reference section contains sources of information with the available web links. Furthermore, the Matlab subsystem models are presented in Appendix A for easier understanding.

Chapter 2

Analysis of Ramea Hybrid Power System

2.1 Overview of the System

Ramea power system is comprised of three diesel generators, six squirrel cage induction generator based wind turbines, three permanent magnet synchronous generator based wind turbines, an electrolyzer, three hydrogen storage tanks, five hydrogen generators and time varying loads. This is a remote island near the south coast of Newfoundland and its latitude and longitude are 47.519525°N and 57.4011889°W respectively. HOMER is a tool which is used to size the off-grid or grid connected power system as well as analyze the system economics and electrical performances. This tool has been being used since 1993 by many individuals, incorporations, NGOs, government institutions and universities throughout the world [45]. National Renewable Energy Laboratory (NREL) has developed this software and allowed free downloading. As illustrated in Chapter 1, the wind-diesel system is already in operating mode and further expansion is soon going

to be accomplished, hence the sizing of Ramea power system has reached beyond discussion. Therefore, the electrical characteristics of the above mentioned system necessitate to be highlighted. As the wind speed and consumed load profile exhibit time varying nature, this system can be recounted to a small extent economical point of view. Figure 2.1 shows the hybrid power system configuration of Ramea in Homer.

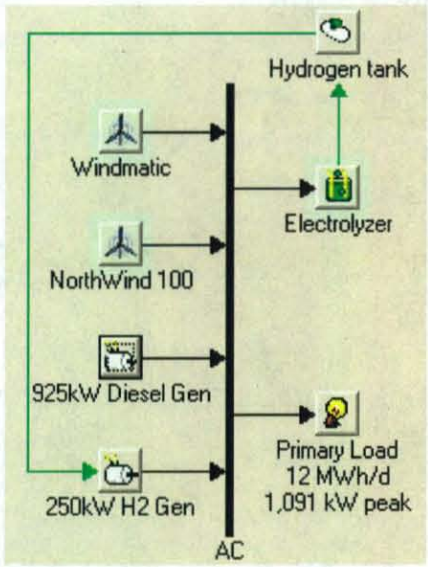

Figure 2.1: Ramea Power System simulation in HOMER

2.2 Components of Hybrid Power System

As shown in Figure 2.1, two kinds of wind turbines, diesel and hydrogen gensets, hydrogen tanks, electrolyzer and primary load are the parts of the hybrid energy system. The ratings and numbers of operating components have already been decided by the NL Hydro. Hence the capital cost, replacement cost, operation and maintenance (O&M) cost and operation period have to be assigned. Following sections will reveal the employed

component parameters ascription, resource availability, optimized results and sensitivity analysis. It should be noted that, this system has only AC bus at 4.16 kV.

2.2.1 Windmatic Wind Turbines

Six WM15S wind turbines have been selected for this site. The capital cost, replacement cost and O&M cost are as $ 90,000, $ 70,000 and $ 1,200 per year respectively for each unit. All these cost information have been obtained from Newfoundland Hydro [46]. This 66 kW AC wind turbine has the hub height of 25 m and operating life time of 20 years. This information has also been found from [22-24 and 47]. From the power curve in Figure 2.2, it can be seen that the cut-in, rated and cut-out wind speeds are 4 m/s, 15 m/s and 23 m/s respectively. It is important to mention here that the capital cost includes the shipping and installation cost of $ 30,000 for each unit.

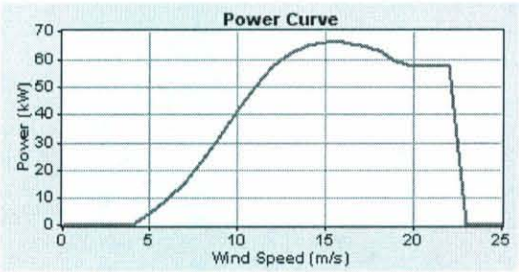

Figure 2.2: Windmatic Wind Turbine Power Curve

2.2.2 NorthWind 100 Wind Turbine

NW100 is a 103 kW AC power generating wind turbine which is manufactured by Northern Power Incorporation. Its operating life span is 20 years and hub height is 37 m.

The power curve of this wind turbine provided by the manufacturer is depicted in Figure 2.3. The capital cost (including transportation and installation cost) and replacement costs are $ 550,000 and $ 480,000 respectively obtained from NL Hydro. The O&M cost is chosen as $ 3,600 per year having idea from [22-24 and 47]. Three such turbines are input to the Ramea power system. Figure 2.3 expresses the power curve of NorthWind 100.

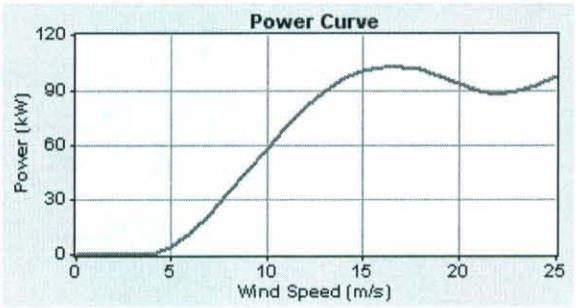

Figure 2.3: NorthWind 100 Wind Turbine Power Curve

2.2.3 Diesel Generator

Although there are three diesel generators on site, one of them is running continuously and the rest two are kept in standby mode. Therefore only one 925 kW is selected as the considered size. The capital and replacement cost are $ 100,000 and $ 80,000 respectively for single unit. From [47], the O&M cost has been found as $ 5 per hour. Its operating time is culled as 10,000 hours from the same reference. However, 30% is taken as the minimum load ratio which represents that minimum 277.5 kW load is required for appropriate functioning of diesel generator. In order to define the generator efficiency, two parameter values should be assigned; one is intercept coefficient and another is slope.

The intercept coefficient means the no load fuel consumption divided by its rated capacity and the slope is referred to as the marginal fuel consumption of the generator. Their numerical expressions are 0.01949 L/hr/rated-kW and 0.2292 L/hr/output-kW respectively. The generator efficiency curve is depicted in Figure 2.4.

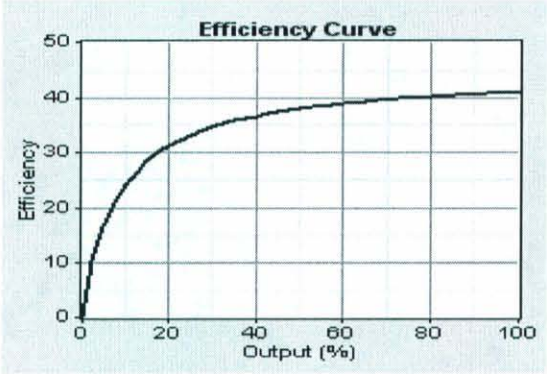

Figure 2.4: Diesel Generator Efficiency Curve

2.2.4 Hydrogen Generator

There are four hydrogen generators, each of 62.5 kW rated power, planned to be operated and one will be kept as standby. Their fuel is the compressed hydrogen coming from the tank. The 250 kW hydrogen generators' capital, replacement and O&M cost are $ 200,000, $ 150,000 and $ 5 per hour respectively. Like the diesel generator the lifetime and minimum load ratio of the hydrogen generators are 10,000 hours [47] and 30%. Furthermore, the values of intercept coefficient and the slope have been gleaned as 0.003238 L/hr/rated kW and 0.1629 L/hr/output kW. After considering all these values the efficiency of the hydrogen generators become similar to Figure 2.5 as follows.

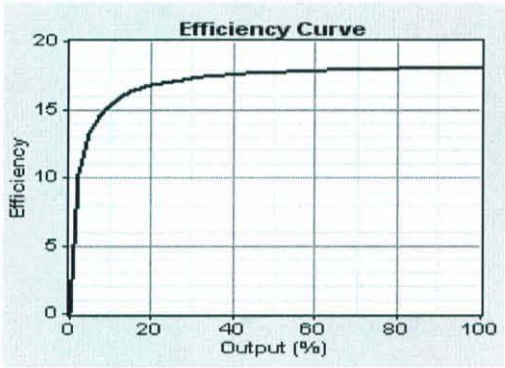

Figure 2.5: Hydrogen Generator Efficiency Curve

2.2.5 Electrolyzer

A 200 kW rated electrolyzer is soon going to be brought into operation on site. The life span of electrolyzer is recorded as 5 years [22-24], efficiency is 75% and minimum load ratio is 30% have been chosen. Being reported by NL Hydro [46], the capital, replacement and the O&M costs have been written as $ 150,000, $ 120,000 and $ 600 per year. As this device is connected to the AC bus, the AC type electrolyzer has been picked.

2.2.6 Hydrogen Tanks

Three hydrogen tanks have already been set up in Ramea. Their collective volume is 1000 Nm^3 and hydrogen storage capacity is 84 kg. Their capital and replacement cost are $ 100,000 and $ 70,000 respectively and no expenditure for O&M [46]. 10 years has been culled as their operation duration [22-24]. In HOMER, it has been considered that there is

no hydrogen initially in the tank. However, there is no requirement for maintaining the year-end tank level.

2.2.7 Primary Load

Ramea is place of around 700 inhabitants. Approximately 300 settlements have been found including houses, school, church, fish plants, commercial institutions and recreational spots. The hourly load data throughout the year have been found from [46] and input to HOMER tool. The primary load window reveals that the daily average energy consumption is 11,728 kWh. Moreover, the average and peak load of this region are recorded as 489 kW and 1091 kW sequentially. The property of load variability can be elucidated by two terminologies; one is day-to-day variability and another is time step-to-time step variability. The former term represents the standard deviation in the sequence

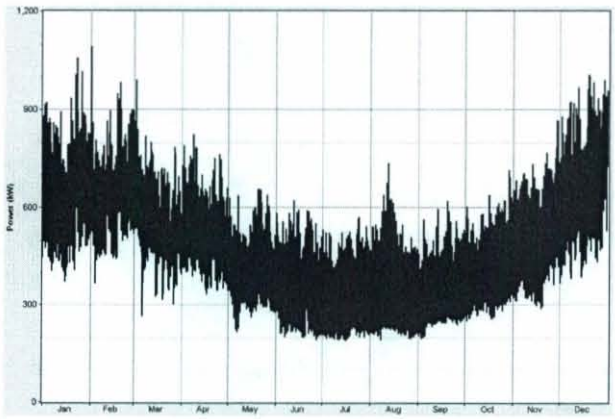

Figure 2.6: Hourly Load Profile

of daily averages and the latter term recounts the standard deviation in the difference between the hourly data and the average daily profile. They can be expressed numerically as 8.14% and 7.86% respectively. The load factor is reported as 0.448 and can be defined as the ratio of average load demand to the peak load. Besides the average daily energy consumption, additional four nearby values such as 10,500 kWh/d, 11,000 kWh/d, 12,000 kWh/d and 12,500 kWh/d have been considered for sensitivity analysis. The hourly load profile and the scaled daily profiles are shown in Figure 2.6 and 2.7 respectively.

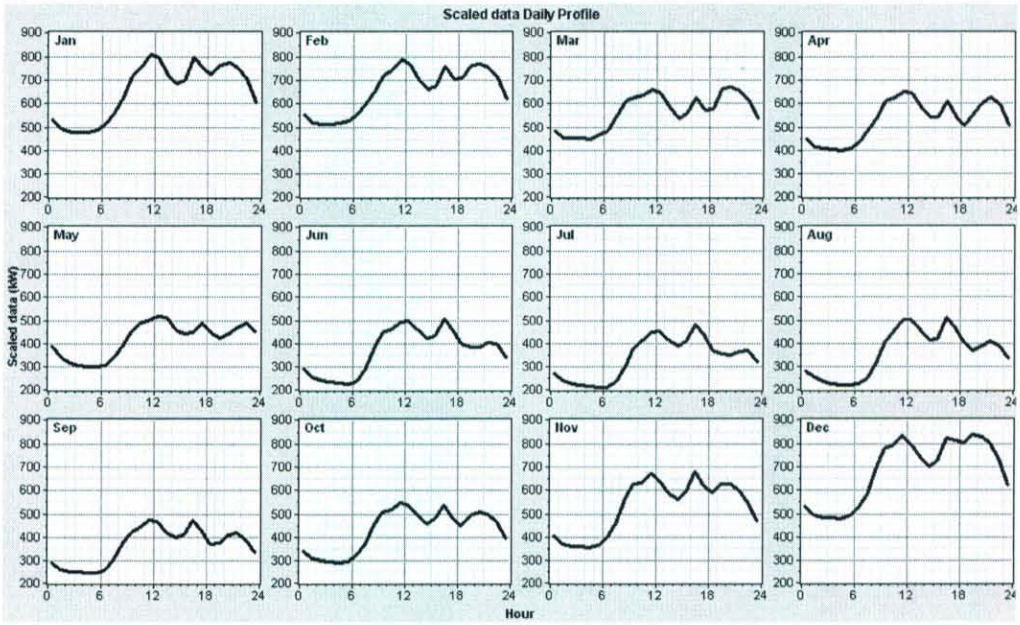

Figure 2.7: Daily Load Profile of Each Month of the Year

2.3 Available Resources

The only renewable resource used for the energy production in Ramea is wind. No other green energy source proves more potentiality than wind in or nearby to this region. The daily solar insolation in this territory has been found as 3.174 kWh/m^2 and the clearness

index as 0.453 [45] which are inadequate and infeasible. As a consequence, no PV panel has been set up for utilizing the solar energy. Figure 2.1 unveils that wind, diesel and hydrogen are the fuels for three types of generation. Hydrogen is produced by the electrolyzer which behaves like a load for the power generation systems. This section will explicate the wind and diesel as external sources to the power system. However, internally generated hydrogen will come up in further discussion.

2.3.1 Wind Energy

The 8760 data points of hourly wind speed throughout the year have been extracted from [46]. These data points can be validated considering two factors, such as the altitude of Ramea and the anemometer height from ground. In this occasion, the altitude of Ramea is reported as 0 m (above sea level) [48] and the anemometer height is set at 10 m. After inserting all the data, HOMER automatically calculates the annual average wind speed as 6.08 m/s. In order for sensitivity analysis 5.5 m/s and 6.5 m/s have been introduced. Weibull shape factor (k), autocorrelation factor, diurnal pattern strength and hour of peak wind speed are the terminologies belong to the advanced parameters and play important roles controlling the conversion of 8760 hourly values from 12 monthly values in the table. The k denotes the width of the wind speed distribution over the year. The autocorrelation factor indicates the dependency of one hour's wind speed with that of the previous hour. The diurnal pattern strength refers to the relationship between the wind speed and the time of the day. The hour of peak wind speed simply means the time of the day when it remains the windiest on average throughout the year. In this instance the

values of these advanced parameters are 2.02, 0.947, 0.0584 and 16 respectively. Several wind resource profiles are uncovered through Figure 2.8 – 2.11 as follows.

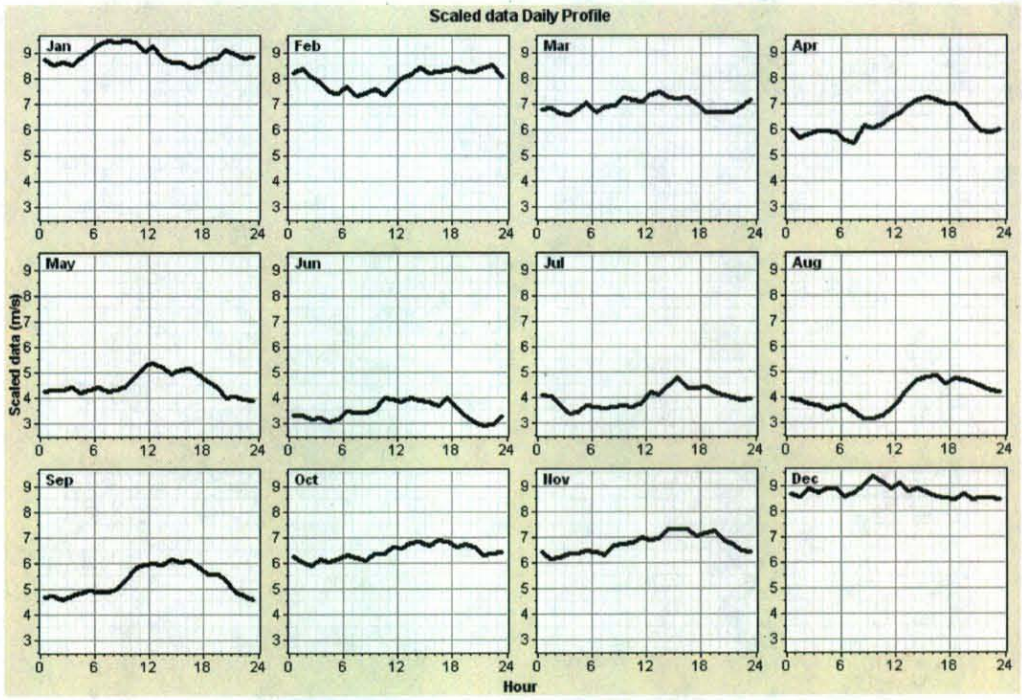

Figure 2.8: Daily Wind Speed Profile of Each Month of the Year

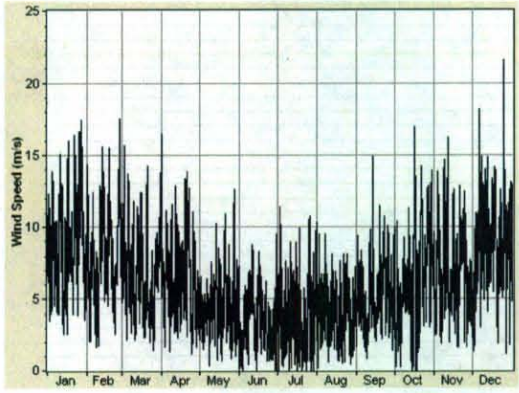

Figure 2.9: Hourly Wind Speed Profile

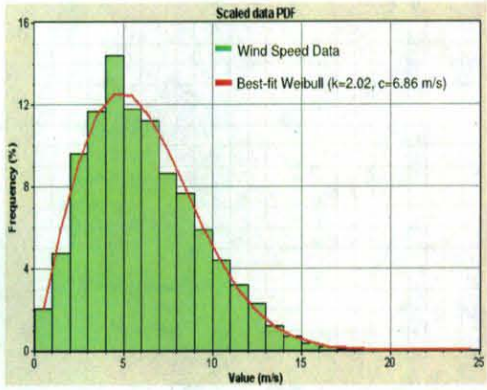

Figure 2.10: Wind Speed Probability Distribution Function

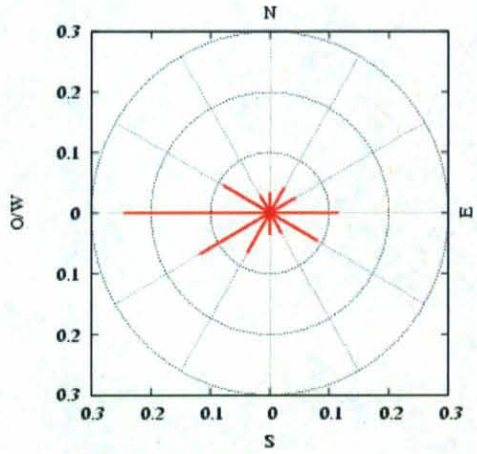

Figure 2.11: Annual Wind Rose [6]

2.3.2 Diesel Energy

Although diesel has harmful emissions, it has been a versatile used fuel so far. Its most important advantage is, it has a large energy density. The regular diesel price can be found from any gas station but most likely the diesel is cheaper when bought in a bulk amount to feed the generator. The realistic diesel price has been found from [46] as $ 1 per Litre. But for performing the sensitivity analysis other quantities such as $ 0.8 per Litre, $ 1.2 per Litre and $ 1.4 per Litre have been considered. Lower heating value, density, carbon content and sulfur content are the parameters used to elucidate the properties of any kind of fuel in HOMER software. In the case of diesel those values are designated as 43.2 MJ/kg, 820 kg/m^3, 88% and 0.33% sequentially.

2.4 Sensitivity Analysis

Three different values of wind speeds, five values of primary energy consumptions and four values of oil prices have been assigned as discussed in the previous section to execute the sensitivity analyses. As the numbers of components, their sizes and ratings have already been decided, it is nugatory to determine the types of optimal systems for various applied conditions. Rather it is more convincing to explicate and contemplate the results relating the sensitivity variables with other variables of interest with the help of surface plots. Some of the significant relationships are established and shown from Figure 2.12 to 2.16.

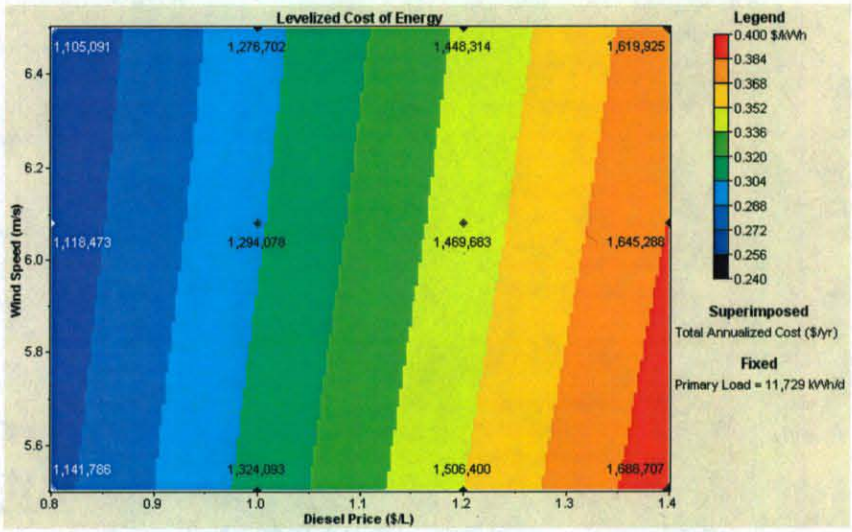

Figure 2.12: Surface Plot with Levelized Cost of Energy and Total Annualized Cost

In Figure 2.12, the wind speed and the diesel price are chosen as axes parameters keeping the primary load constant at 11,729 kWh/d. The states of levelized cost of energy and annualized cost are recounted. As seen from the above figure the wind speed has a little impact on levelized cost of energy but within the specified range of diesel price the levelized cost may rise from 0.256 to 0.4. Similarly, the superimposed parameter

(Annualized Cost) increases rapidly with diesel price but reduces gradually with the wind speed.

In Figure 2.13 the axes parameters are retained as before and the consumed energy also remains same. In this occasion the Net Present Cost (NPC) changes little with the variation of wind speed. On the contrary, the oil price has a greater influence on NPC. However, the total O&M cost behaves independent with the diesel price and escalate slightly with upraise of wind speed.

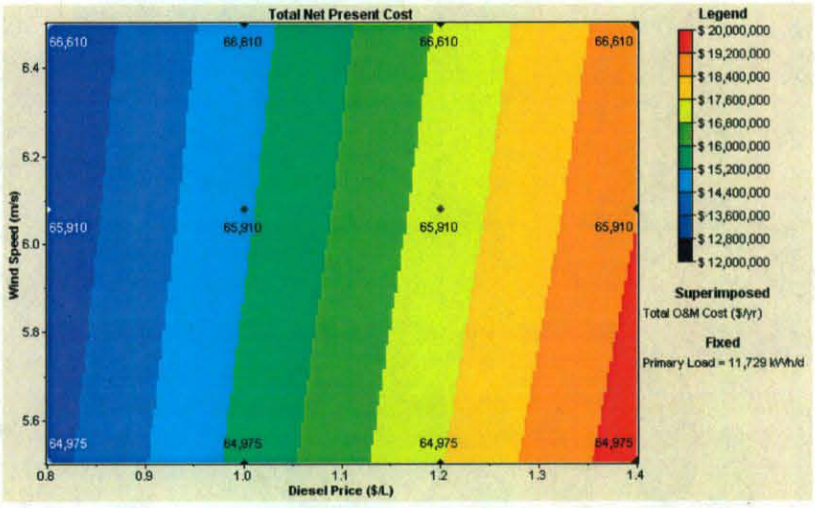

Figure 2.13: Surface Plot with Net Present Cost and Total O&M Cost

Similar kind of surface plot has been achieved while analyzing the total operating cost and the fuel cost. Figure 2.14 uncovers that the total operating cost uplifts sharply with the diesel price. On the other side, the fuel cost is considerably proportional to the diesel price whereas, it declines with elevated wind speed.

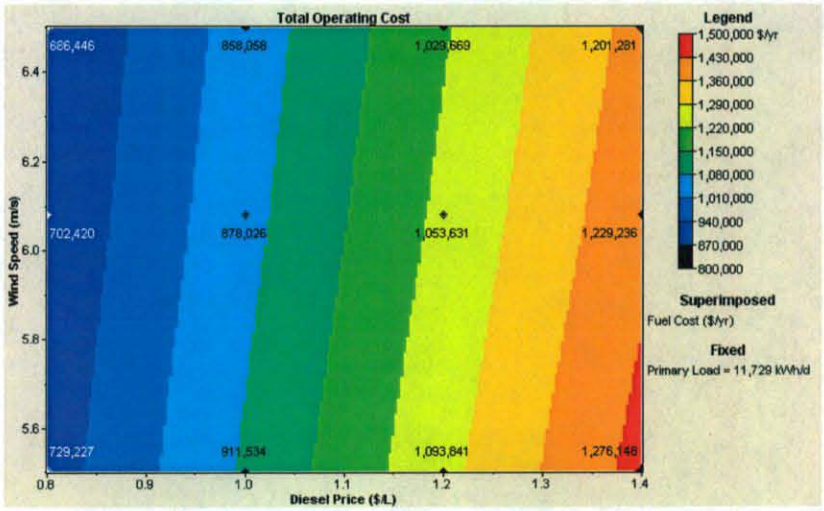

Figure 2.14: Surface Plot with Total Operating Cost and Fuel Cost

Figure 2.15 portrays the total electrical energy production and the diesel consumption with the sensitivity variables wind speed and primary load. Here the diesel price has been fixed at present practical value as $ 1 per Litre. It is evident that with the increment of primary load or wind speed, the energy production will also increase and this fact is reflected from the figure. On the other hand the diesel consumption follows the load with increment and decrement and behaves reverse way to the wind speed, i.e. with the rise of wind speed the fuel consumption gets slumped.

Another diagram depicts the relationship between the same sensitivity variables with the harmful gas emissions. The diesel fuel contains mostly of carbon and nitrogen. Figure 2.16 reveals that in a year the Ramea power system emits maximum 2,550,000 kg of carbon dioxide and 55,434 kg of nitrogen oxides which is really deleterious. The maximum emission occurs at low wind speed and high load demand. Most likely the diesel generator supplies with the major part of energy at that time. But when the wind

speed increases and load demands become smaller, the rate of harmful gas discharge reduced drastically.

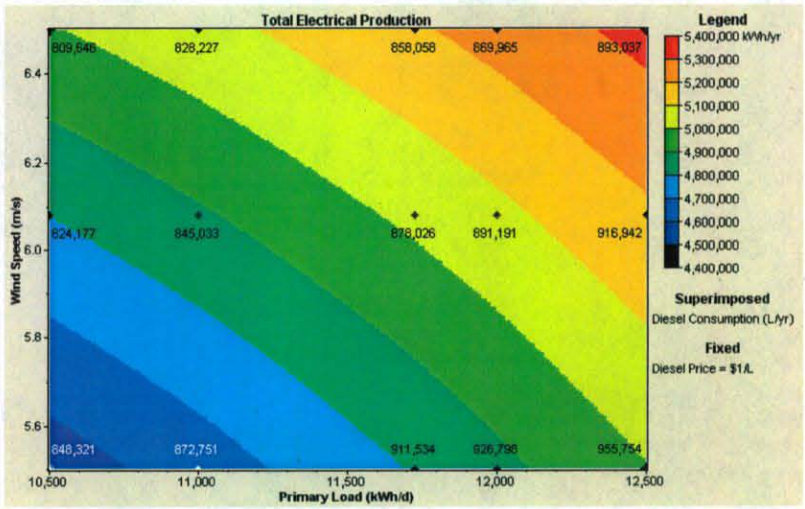

Figure 2.15: Surface Plot with Total Electrical Energy Production and Diesel Consumption

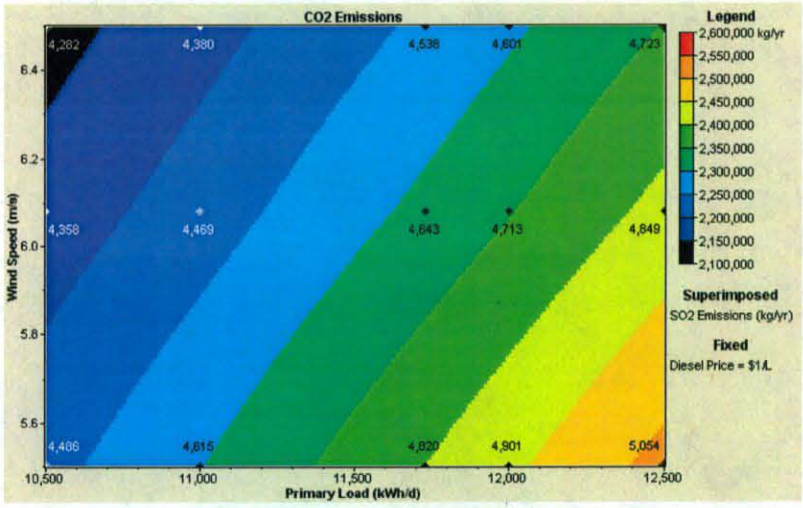

Figure 2.16: Surface Plot with CO_2 and NO_2 Emission

2.5 Optimization Results

Optimization Results imply to choosing the best combination of electrical devices which offers the least Cost of Energy (COE). The former discussion unveils that executing such kind of analysis is beyond the scope of this research. This, in other words, incorporates the performance of each component of Ramea power system. The following sections will outline a number of features of these components.

2.5.1 Cost Summary

The total system or project expenditure can be identified by the Net Present Cost (NPC). Figure 2.17 and 2.18 explain the system NPC by pointing out the capital, replacement, operating, fuel costs and salvage values of individual components. As the diesel generator runs continuously 8760 hours in a year, it consumes lots of diesel. Therefore, the fuel cost is remarkably high for the diesel generator. Like fuel cost, the O&M cost is again highest for the diesel genset. The following two figures delineate that the NorthWind 100 wind turbines capital cost is exceptionally high due to being brand new from the industry. Unlike the NW100 wind turbines, the WM15S wind turbines are not that much costly, one of the reasons might be these are refurbished one. The salvage value refers to the amount that can be compatible to market price at that instant of any component or the whole system after a certain years of operation. In order to determine the whole project cost, this salvage amount is deducted from the capital, replacement, O&M and fuel costs altogether. Moreover, the Cost of Energy (COE) of this system has been reported as 0.302 $/kWh.

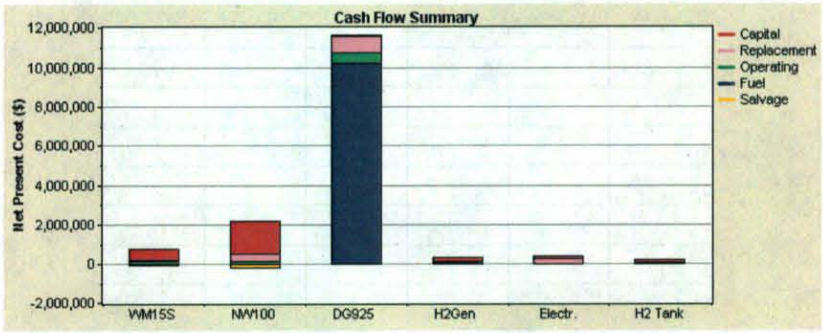

Figure 2.17: Bar Chart of Net Present Cost of Ramea Power System

Component	Capital ($)	Replacement ($)	O&M ($)	Fuel ($)	Salvage ($)	Total ($)
Windmatic	540,000	108,536	83,906	0	-58,038	674,403
NorthWind 100	1,650,000	372,123	125,859	0	-198,989	1,948,993
925kW Diesel Gen	100,000	799,520	510,427	10,232,138	-1,474	11,640,613
250kW H2 Gen	200,000	57,216	40,904	0	-6,771	291,349
Electrolyzer	150,000	221,064	6,992	0	0	378,056
Hydrogen Tank	100,000	53,674	0	0	-6,449	147,225
System	2,740,000	1,612,133	768,087	10,232,138	-271,721	15,080,637

Figure 2.18: Breakdown of Net Present Cost of Ramea Power System

2.5.2 Electrical Performance of System Components

As discussed in Section 2.2.1 and 2.2.2, six WM15S and three NW100 wind turbines are employed to capture wind energy to meet the load. The former mentioned six turbines run 6832 hours producing 1,022,662 kWh energy in a year. Their combined mean power output is 117 kW. The capacity factor and the wind penetration level exhibited by these turbines are 29.5% and 23.9% respectively. Their individual levelized cost has been reported as 0.0566 $/kWh. On the other hand, collective generation of the latter mentioned wind turbines is 805,500 kWh while running 7,003 hours in a year. The mean output power and individual levelized cost have been found respectively as 92 kW and 0.208 $/kWh. Furthermore, in Ramea's environment these wind turbines show the

capacity factor as 29.8% and the wind penetration as 18.8%. Figures 2.19 and 2.20 reveal these quantitative characteristics of both kinds of wind turbines. Also the hourly power generation by them throughout the year is depicted in Figure 2.21.

Quantity	Value	Units
Total rated capacity	396	kW
Mean output	117	kW
Capacity factor	29.5	%
Total production	1,022,662	kWh/yr

Quantity	Value	Units
Minimum output	0	kW
Maximum output	396	kW
Wind penetration	23.9	%
Hours of operation	6,832	hr/yr
Levelized cost	0.0566	$/kWh

Figure 2.19: Electrical Characteristics of WM15S Wind Turbines

Quantity	Value	Units
Total rated capacity	309	kW
Mean output	92	kW
Capacity factor	29.8	%
Total production	805,500	kWh/yr

Quantity	Value	Units
Minimum output	0	kW
Maximum output	308	kW
Wind penetration	18.8	%
Hours of operation	7,003	hr/yr
Levelized cost	0.208	$/kWh

Figure 2.20: Electrical Characteristics of NW100 Wind Turbines

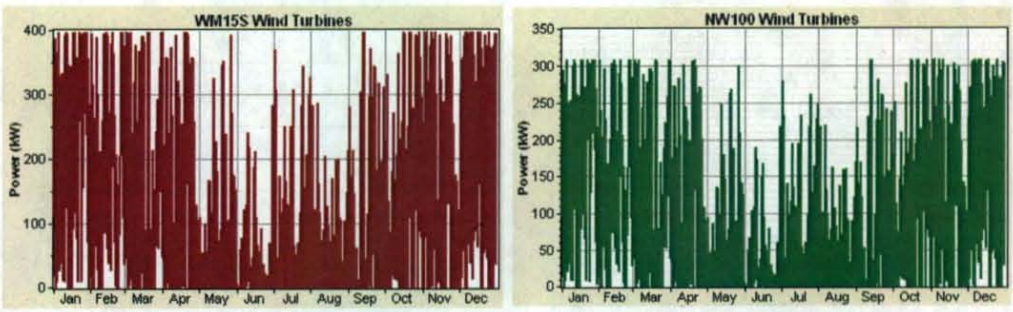

Figure 2.21: Hourly Generated Power of WM15S and NW100 Wind Turbines

The diesel generator has been serving all 8760 hours in a year while producing 3,141,887 kWh of energy. During this time it consumes total of 878,026 Litres of diesel. Minimum, maximum and average powers exhibited from the diesel generator are 278 kW, 925 kW and 359 kW respectively. The year-round marginal generating cost has been

reported as 0.229 $/kWh. Figures 2.22 and 2.23 show all necessary data and hourly power generation from January till December associated with this generator.

Quantity	Value	Units
Hours of operation	8,760	hr/yr
Number of starts	1	starts/yr
Operational life	1.14	yr
Capacity factor	38.8	%
Fixed generation cost	31.0	$/hr
Marginal generation cost	0.229	$/kWh

Quantity	Value	Units
Electrical production	3,141,887	kWh/yr
Mean electrical output	359	kW
Min. electrical output	278	kW
Max. electrical output	925	kW

Quantity	Value	Units
Fuel consumption	878,026	L/yr
Specific fuel consumption	0.279	L/kWh
Fuel energy input	8,639,772	kWh/yr
Mean electrical efficiency	36.4	%

Figure 2.22: Electrical Characteristics of 925 kW Diesel Generator

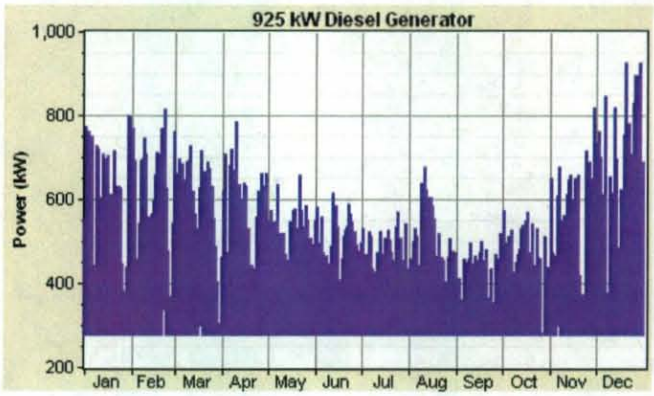

Figure 2.23: Hourly Generated Power of 925 kW Diesel Generator

Unlike diesel generator, the hydrogen generators run only 702 hours in a year. Therefore their operating life span is as large as 14.2 years. Hydrogen consumption by the generators is 9,162 kg/yr and their specific fuel consumption is recorder as 0.174 kg/kWh. The minimum, maximum and average power associated with these hydrogen gensets are 75 kW, 93.6 kW and 75.1 kW respectively. Characteristics of generators and hourly power generation throughout the year are expounded in Figure 2.24 and 2.25.

Quantity	Value	Units
Hours of operation	702	hr/yr
Number of starts	702	starts/yr
Operational life	14.2	yr
Capacity factor	2.41	%
Fixed generation cost	20.0	$/hr
Marginal generation cost	0.00	$/kWh

Quantity	Value	Units
Electrical production	52,752	kWh/yr
Mean electrical output	75.1	kW
Min. electrical output	75.0	kW
Max. electrical output	93.6	kW

Quantity	Value	Units
Hydrogen consumption	9,162	kg/yr
Specific fuel consumption	0.174	kg/kWh
Fuel energy input	305,384	kWh/yr
Mean electrical efficiency	17.3	%

Figure 2.24: Electrical Characteristics of 250 kW Hydrogen Generator

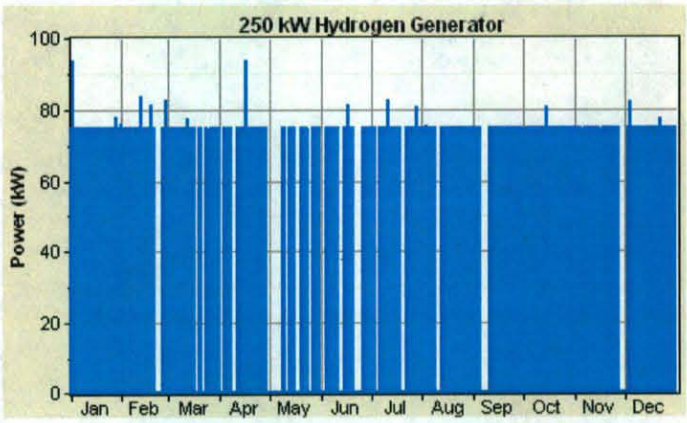

Figure 2.25: Hourly Generated Power of 250 kW Hydrogen Generator

The electrolyzer produces hydrogen only when some additional energy exists after feeding the load. This device uses DC current after converting the AC current from the grid. The 200 kW electrolyzer associated with this research produces 9,171 kg of hydrogen in a year. Hence the levelized cost of hydrogen becomes $ 141 per kg. The input and output behaviors of the electrolyzer are portrayed in Figure 2.26. Moreover, the dynamics of three hydrogen tanks with total capacity of 84 kg and volume of 1,000 Nm^3 is elucidated in Figure 2.27.

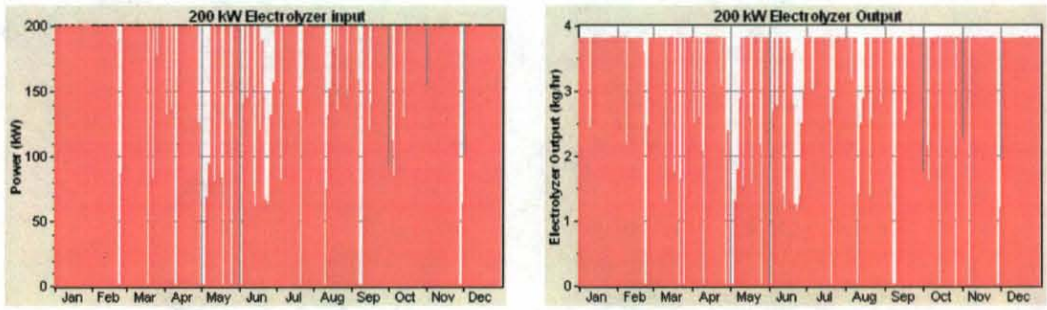

Figure 2.26: Hourly Input Power and Generated Hydrogen of 200 kW Electrolyzer

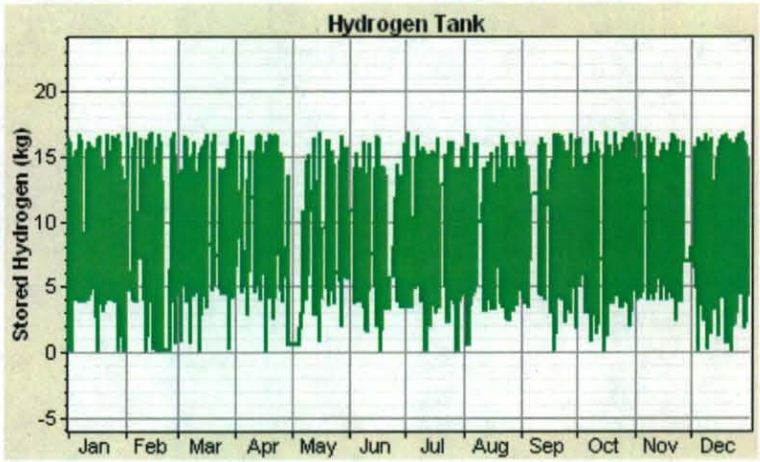

Figure 2.27: Hourly Stored Hydrogen in the Hydrogen Tank

2.5.3 Electrical Performance of Overall System

After determining the performance of each individual component, it is necessitated to ascertain the overall characteristics of the system. Figure 2.28 and 2.29 unveil those features. It can be seen that the contribution to the year-round energy production of wind and diesel are 36% and 63% respectively. Remaining 1% is produced by the hydrogen. The electrolyzer itself offers a load to the AC bus which is about 10% of the total year-round load demand. Besides the energy production and consumption, the effects of excess

electricity, unmet load and capacity shortage can not be overlooked. Figure 2.30 gives the idea about excess electricity and the unmet load in a year. Yearly excess energy from the whole system is 259,549 kWh which can be used for space heating, water heating, water pumping etc. Unmet load and capacity shortage have been recorded as 302 kWh and 704 kWh respectively. However, the renewable fraction of the system is found as 37.4% which is quite appreciable to the fact that it assists reducing diesel consumption and hence green house gas emissions.

Production	kWh/yr	%
Wind turbines	1,828,162	36
925kW Diesel Gen	3,141,887	63
250kW H2 Gen	52,752	1
Total	5,022,801	100

Consumption	kWh/yr	%
AC primary load	4,280,795	90
Electrolyzer load	482,333	10
Total	4,763,128	100

Quantity	kWh/yr	%
Excess electricity	259,549	5.17
Unmet electric load	302	0.01
Capacity shortage	704	0.02

Quantity	Value
Renewable fraction	0.374

Figure 2.28: Electrical Characteristics of Ramea Hybrid Power System

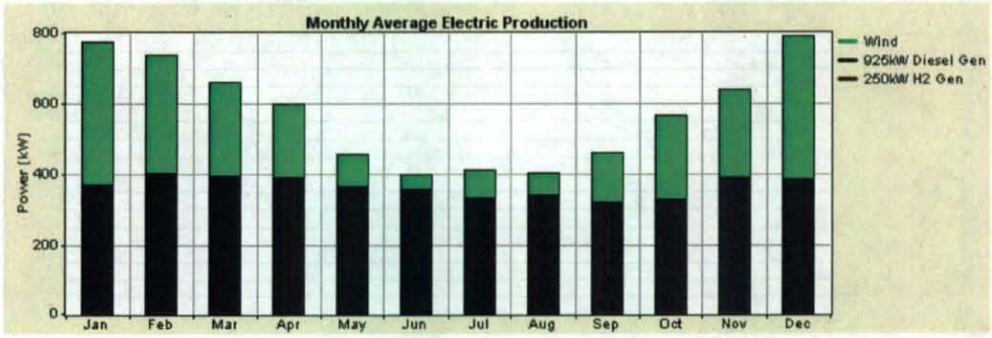

Figure 2.29: Monthly Energy Production by Wind, Diesel and Hydrogen

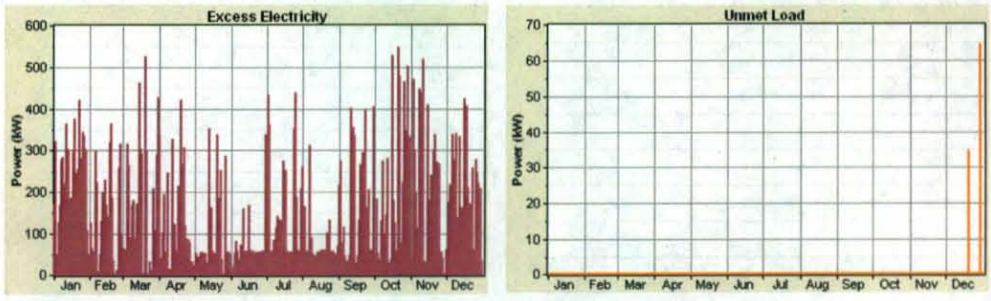

Figure 2.30: Excess Electricity and Unmet Load of Ramea Hybrid Power System

2.5.4 Green House Gas Emissions by Hybrid Power System

Green House Gas (GHG) emission has become an important issue nowadays. The foremost objective of exploiting the renewable resources and introducing hybrid power systems is to ensure healthier environment. Before utilizing the three 100 kW wind turbines and electrolyzer, hydrogen tank and hydrogen gensets, the condition was far worse in terms of pollutant quantity. After introducing those components the condition has been improved to some extent, although the carbon dioxide emission is too high and reported as 2,312,130 kg/yr. The second highest pollutant is nitrogen oxides and the quantity is 50,925 kg/yr. Other GHGs have comparatively little impact on environment. Figure 2.31 displays all pollutants and their emission levels.

Pollutant	Emissions (kg/yr)
Carbon dioxide	2,312,130
Carbon monoxide	5,707
Unburned hydrocarbons	632
Particulate matter	430
Sulfur dioxide	4,643
Nitrogen oxides	50,925

Figure 2.31: GHG Emissions by Ramea Hybrid Power System

2.6 Summary

This chapter focuses on explicating the economics and electrical performances of Ramea Wind-Diesel-Hydrogen hybrid energy system by using the HOMER tool. Most of the essential data have been provided by Newfoundland Hydro. Capital, replacement and O&M costs are assigned for each component along with their lifetime. In fact those three

costs are the primary inputs the HOMER deals with. In order to establish the internal combustion generators' efficiency curve, a number of associated parameters have been designated. Furthermore, the abundant availability of wind energy has been outlined as the most obtrusive renewable resource at Ramea. Wind speed, diesel price and consumed energy have been considered as the parameters which are subject to change over time. Hence their effects of changes on other parameters have been highlighted with surface plots. The latter part of this chapter is affiliated with the hourly transient behaviors of power system components. It is worth to mention that in the existing Wind-Diesel system, wind turbine is taking part of generating around 10% of total community consumption [3, 49]. However the prospective plan including new wind turbines and hydrogen system will have 37.4% of renewable fraction which is far better than desired level. Optimization results show that the unmet load and the capacity shortage in a year are quite negligible compared to the whole generation. The addition of renewable energy generation to the system will reduce the diesel consumption having positive impact on environment. This, in other way, must be an appreciable approach towards the worldwide increasing oil price conditions.

Chapter 3

Modeling of Wind Energy Conversion Systems

3.1 Wind Power Plants

The principle components of a modern wind power plant are the tower, the rotor and the nacelle, which accommodates the transmission mechanisms and the generator, and for horizontal-axis devices, the yaw system for steering in response to changes in wind direction. Switching and protection systems, lines and may be also transformers and networks, will be required for supplying end users or for storage. In response to the external influences, a unit for operational control and regulation must adapt the flow of energy in the system to the demands placed upon it. The following sections provide details and models of the components of wind energy conversion system.

3.2 Functional Structure of Wind Turbines

The block diagram given in Figure 3.1, showing the links between the most important components and the associated energy conversion stages, may serve as the basis for later detailed sections. This figure also gives an idea of how operation can be influenced by control and supervisory actions. Moreover, the central position occupied by the generator becomes particularly significant. The following section will explicate the physical behavior of a wind energy extraction system and conversion of the mechanical energy to the electrical energy by means of generators.

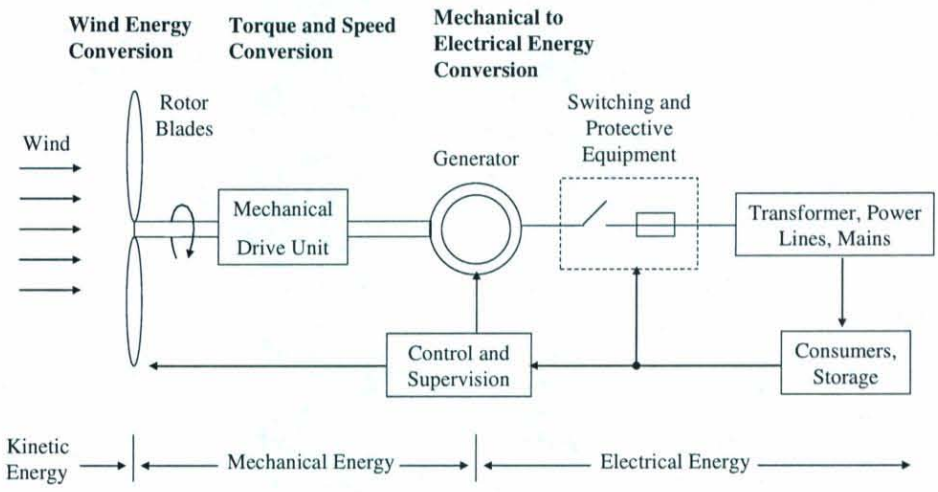

Figure 3.1: Energy Transfer in a Wind Power Plant [52]

3.3 Components of Wind Power Plants

This research includes determining the dynamic models of WM15S and NW100 wind turbines. The former one is a 65 kW two squirrel-cage induction generators based wind turbine and latter one is 100 kW direct-drive permanent synchronous generator based

wind turbine. Before analyzing the dynamic behavior, it is more practical to compute their steady state behaviors first and then incorporating them with other components. Following texts will cover the constituents of wind power plants.

3.3.1 Rotor Blades

Aluminum, steel, titanium, fiber composite material (glass, carbon and aramide fibers) and wood [53] are some of the examples of materials used for building wind turbine blades. The most important material properties for wind turbine blades are specific weights, strength limit, modulus of elasticity, tearing length, modulus of elasticity related to the specific weight and allowable fatigue stress after 10^7 to 10^8 load cycles. However, material cost, production cost and cost of development involved are also significant factors.

From the specification sheets collected from manufacturer websites [54-55], it has been found that the wind turbines in Ramea have fiber reinforced composite blades. These materials are currently being used in almost all lightweight structures. Even in large commercial aircraft, fiber reinforced materials increasingly prevail. Glass, carbon and organic aramide fibers are presently available materials found in the marketplace. The fibers are available in highly varying qualities, from high-quality aero-space quality down to low-grade fiber material for simple fairing structures. The fatigue strength of organic aramide fibers has not been tested yet completely and hence they cannot be taken into consideration for rotor blades. The most widely used fiber is glass fiber.

3.3.2 Rotor Shaft and Bearings

There are three rotor shaft and bearing arrangements found so far [53]. Those are as follows,

- Rotor shaft with separate bearings,
- Rotor shaft integrated into the gear box and
- Rotor bearing assembly on a fixed support axle.

There are numerous realizations which have characteristics belonging to the one or the other concept. For instance, in some wind turbines the rotor is mounted on the load-carrying, front nacelle structure via a live-ring bearing, whereas the rear bearing is integrated into the gearbox. This solution also avoids a long rotor shaft and saves weight. Figure 3.2 reveals the assembly of three point suspension of the rotor shaft-gearbox where the rear bearing is integrated into the gearbox.

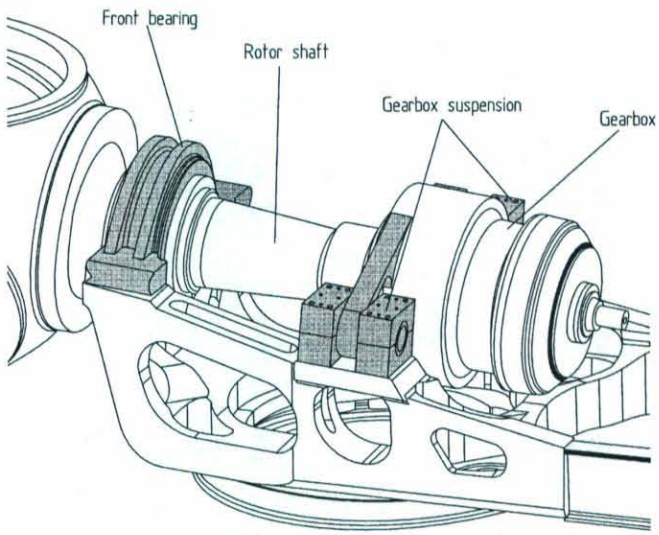

Figure 3.2: Three Point Suspension of the rotor shaft / Gear box Assembly [53]

3.3.3 Rotor Brakes

The functionality of the turbine rotor brakes can be classified into parking braking and operating braking. The primary role of the brake is restricted to mere arresting function during rotor standstill. In small and medium wind turbines, a mechanical rotor brake, which in cases of emergency prevents rotor over-speed, has proven extraordinarily successful and is largely common practice. Very often the task of the rotor brake is restricted to the function of mere parking brake in large turbines. When the position of the rotor brake is concerned, both the alternatives have been common practices for the rotor brakes to be on the slow or on the fast rotating side of the gearbox, although they have some advantages and disadvantages. Brakes are basically part of safety system therefore their dynamic modeling in not done in this research.

3.3.4 Gearbox

Gearboxes are manufactured in two different forms. One is the parallel shaft or spur gear system and other is the technically more complex planetary or helical gearing. Spur gear stages are built with a gear ratio of up to 1:5, whereas the planetary stages of up to 1:12. Wind turbines normally require more than one stage; two and three stages with different assembly are more common. It is remarkable that the three stage planetary design has only a fraction of the overall mass of a comparable parallel shaft system and the cost is reduced by about half. That is why the wind turbines erected in Ramea have three-stage gearboxes.

3.3.5. Electrical Generation Systems

Different kinds of generators are used in wind energy conversion systems. Depending on manufacturer the provisions of generators are doubly-fed induction generator, permanent magnet synchronous generator, squirrel cage induction generator etc. All of them have got popularity and being used in number of wind farms. WM15S and NW100 wind turbines used in Ramea employ squirrel cage induction generator and permanent magnet synchronous generator respectively. Following sections will explicate the basic principles of those generators.

3.3.5.1 Squirrel Cage Induction Generator

A three phase squirrel cage induction generator has three identical windings that are symmetrically distributed around the inner surface of a laminated cylindrical shell called the stator. The laminated rotor inside carries a winding consisting of bars connected to two shorting rings at both ends. This rotor can be characterized to be adapted to any number of stator poles. When the balanced stator windings wound for p number of pole pairs and displaced in space by 120 electrical degrees and the applied torque creates a field rotation in the air gap, n_s, then a three phase voltage will be induced in the stator winding having frequency, f. The relationship between pole pairs, frequency and the field rotation can be expressed as follows [56]

$$n_s = \frac{f}{p} \qquad (3.3.1)$$

Here n_s is expressed in rad/s and is known as the synchronous speed of the induction generator.

The resultant air-gap flux, φ_m is set up by the combined action of the stator and the rotor magneto-motive force (mmf). This synchronous rotating flux induces a counter emf E_1 in the stator phase winding. The stator terminal voltage V_1 differs from this counter emf E_1 by the stator leakage impedance drop. The stator emf phasor equation is then

$$\overrightarrow{V_1} = \overrightarrow{E_1} + \overrightarrow{I_1}(R_s + jX_{ls}) \qquad (3.3.2)$$

The circuit representation of equation 3.3.2 is shown in Figure 3.3. The stator winding current I_1 can be resolved into an exciting component I_0 and a compensating load component current I'_2. The load component current I'_2 counteracts the rotor mmf, thereby demanding power from source. The exciting component I_0 can be resolved into a core loss component I_c, in phase with the stator induced emf E_1 and a magnetizing component I_m, lagging behind the induced emf E_1 by 90°. This is the magnetizing component which sets up the air gap flux φ_m.

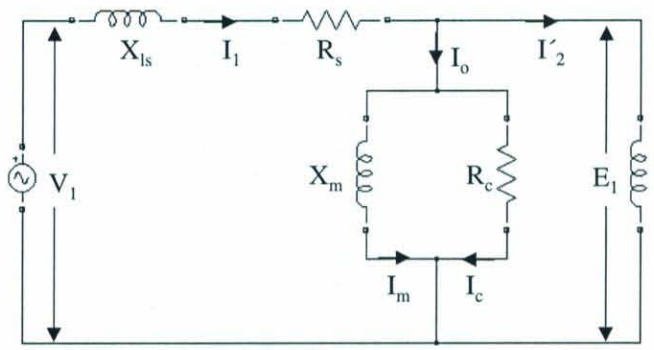

Figure 3.3: Per-phase Stator Circuit Model of a Three Phase Induction Motor [53]

The asynchronous machine block in MATLAB/SimPower Systems/Machines library operates either in motor or generator mode. The mode of operation is dictated by the sign of the mechanical torque. For positive T_m the block acts as a motor and for negative T_m it operates as a generator. The electrical part of the machine is represented by a fourth order state space model and the mechanical part by a second order system. All electrical parameters and variables are referred to the stator. These are denoted by the prime signs in the machine equations. All stator and rotor quantities are in the arbitrary two axis d-q reference frame.

The expressions related to d-q axis representation of an asynchronous generator are stated below [57].

$$V_{qs} = R_s i_{qs} + \frac{d}{dt}\varphi_{qs} + \omega\varphi_{ds} \tag{3.3.3}$$

$$V_{ds} = R_s i_{ds} + \frac{d}{dt}\varphi_{ds} - \omega\varphi_{qs} \tag{3.3.4}$$

$$V'_{qr} = R'_r i'_{qr} + \frac{d}{dt}\varphi'_{qr} + (\omega - \omega_r)\varphi'_{dr} \tag{3.3.5}$$

$$V'_{dr} = R'_r i'_{dr} + \frac{d}{dt}\varphi'_{dr} - (\omega - \omega_r)\varphi'_{qr} \tag{3.3.6}$$

$$T_e = \frac{3}{2} p(\varphi_{ds} i_{qs} - \varphi_{qs} i_{ds}) \tag{3.3.7}$$

Where

$$\varphi_{qs} = L_s i_{qs} + L_m i'_{qr} \tag{3.3.8}$$

$$\varphi_{ds} = L_s i_{ds} + L_m i'_{dr} \tag{3.3.9}$$

$$\varphi'_{qr} = L'_r i'_{qr} + L_m i_{qs} \tag{3.3.10}$$

$$\varphi'_{dr} = L'_r i'_{dr} + L_m i_{ds} \tag{3.3.11}$$

$$L_s = L_{ls} + L_m \tag{3.3.12}$$

$$L'_r = L'_{lr} + L_m \tag{3.3.13}$$

The mechanical part can be represented by the following equations

$$\frac{d}{dt}\omega_m = \frac{1}{2H}(T_e - F\omega_m - T_m) \tag{3.3.14}$$

$$\frac{d}{dt}\theta_m = \omega_m \tag{3.3.15}$$

The topology of the asynchronous generator in d-q axis frame is depicted as follows.

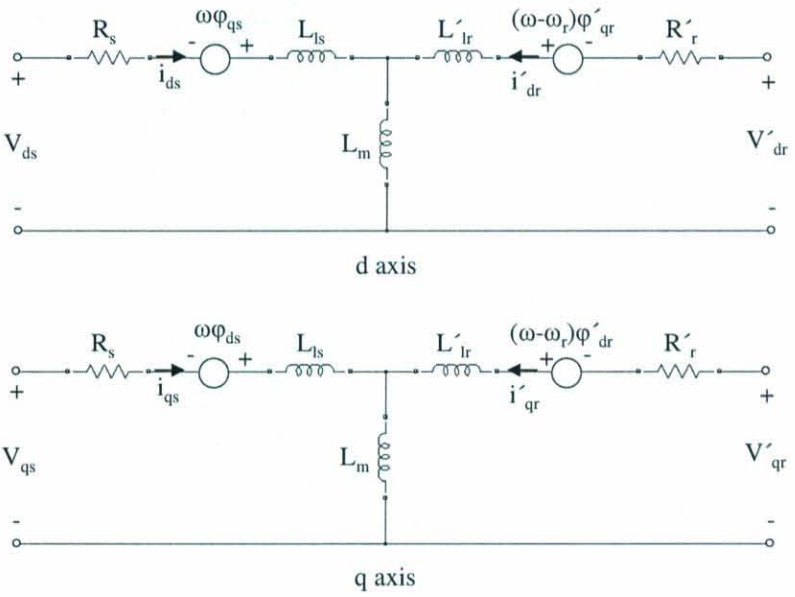

Figure 3.4: Asynchronous Generator Representation in d-q axis Frame

3.3.5.2 Permanent Magnet Synchronous Generator

The basic wind energy conversion requirements of a variable speed permanent generator are almost the same as those for a wound-field synchronous generator. The permanent generator dispenses with the need for external excitation. Therefore, the output voltage, under variable speed operation, varies both in frequency and in magnitude. As a consequence, the DC-link voltage changes in an uncontrolled manner. The control, however, is realized via the DC-AC converter on the grid side.

The turbine shaft speed is controlled by the opposing reaction torque of the generator. The optimum values of the DC voltage and current can be obtained from equations 3.3.16 and 3.3.17. With the diode bridge, assuming ripple-free DC-link current, the generator terminal voltages and currents are as follows [56].

$$V_g = \frac{\pi}{3\sqrt{6}} V_d \tag{3.3.16}$$

$$I_g = \frac{\sqrt{6}}{\pi} I_d \tag{3.3.17}$$

It is noteworthy that for any particular DC-link voltage, there is a minimum speed below which there is no generation. For any wind speed, there exists an optimum turbine speed at which maximum power can be extracted from the wind.

The permanent magnet synchronous generator block exists in MATLAB/ SimPower Systems/Machines library. Like the asynchronous machine, these machines have two operating modes. The sign of T_m determines whether it will run as motor mode or generator mode. Electrically these machines are characterized as sinusoidal model and

trapezoidal model. The sinusoidal model assumes that the flux established by the permanent magnets in the stator is sinusoidal, which implies that the electromotive forces are sinusoidal. For the trapezoidal machines, the model assumes that the flux established by the permanent magnets produce three trapezoidal back EMF waveforms. This research is focused on the sinusoidal model only. The electrical model of such generator is implemented by the following equations [57].

$$\frac{d}{dt}i_d = \frac{v_d}{L_d} - \frac{R_s i_d}{L_d} + \frac{L_q}{L_d} p\omega_r i_q \tag{3.3.18}$$

$$\frac{d}{dt}i_q = \frac{v_q}{L_q} - \frac{R_s i_q}{L_q} - \frac{L_d}{L_q} p\omega_r i_d - \frac{\lambda p \omega_r}{L_q} \tag{3.3.19}$$

$$T_e = \frac{3}{2} p\left[\lambda i_q + \left(L_d - L_q\right)\cdot i_d i_q\right] \tag{3.3.20}$$

The L_d and L_q inductances represent the relationship between the phase inductance and the rotor position due to the saliency of the rotor. For example, the inductance measured between phase a and b is given as follows.

$$L_{ab} = L_d + L_q - \left(L_d - L_q\right)\cos\left(2\theta_e + \frac{\pi}{3}\right) \tag{3.3.21}$$

The following diagram uncovers how the line-line inductance varies as a function of electrical angle of the rotor.

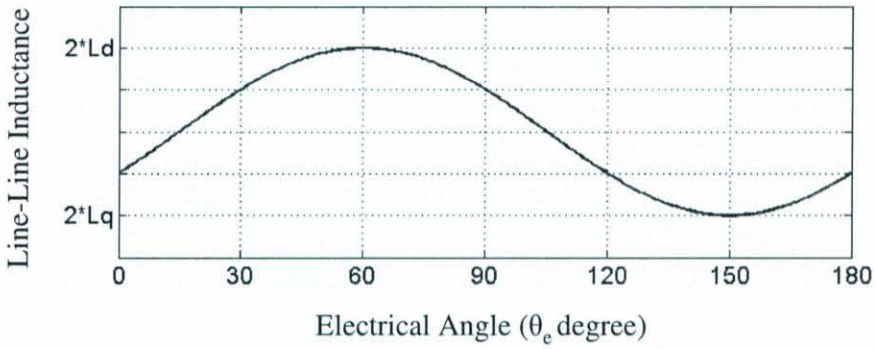

Figure 3.5: Change of Line Inductance with Rotor Positions

For permanent magnet synchronous generator, the rotor might be of either round or salient-pole type. The relationship between d-q frame inductance and line inductance will differ according to their types.

Condition for round rotor:

$$L_d = L_q = \frac{L_{ab}}{2} \tag{3.3.22}$$

Conditions for salient pole rotor:

$$L_d = \frac{\max(L_{ab})}{2} \text{ and } L_q = \frac{\min(L_{ab})}{2} \tag{3.3.23}$$

The mechanical behavior of this machine is same as described in section 3.3.5.1 referring to the equations 3.3.14 and 3.3.15.

3.3.6 Transformer

At Ramea, the magnitude of the voltage associated with the energy produced by the wind turbines is 480 V. This three phase voltage is stepped up to transmit that to the grid substation. All the transformers employed in this region are 480V/4160V Y-Δ type. For consumer applications, this higher magnitude of voltage is again stepped down to a suitable magnitude of the voltage. Therefore, three phase transformer is very important to increase or decrease the voltage magnitude. These transformers can be made either three single phase transformers connected together in a three phase bank or three windings wound in a common core. The former one is cheaper, smaller and lighter than the latter one [58].

The primary winding draws a current when it is connected to an alternating voltage source. This current produces a flux in the transformer core. When the flux moves through the magnetic core and cuts it by the both windings a voltage will be induced in the primary and the secondary windings. From Figure 3.6, the instantaneous emf induced in the primary winding is as follows.

$$e_1 = -N_1 \frac{d\varphi}{dt} = N_1 \omega \varphi_m \cdot \sin(90 + \omega \cdot t) \tag{3.3.24}$$

The maximum value of e_1 is,

$$E_{m1} = N_1 \omega \varphi_m \tag{3.3.25}$$

Now the effective value of the primary emf is,

$$E_1 = \frac{E_{m1}}{\sqrt{2}} = 4.44 f \varphi_m N_1 \tag{3.3.26}$$

Similarly, the emf of the secondary winding is,

$$E_2 = 4.44 f \varphi_m N_2 \qquad (3.3.27)$$

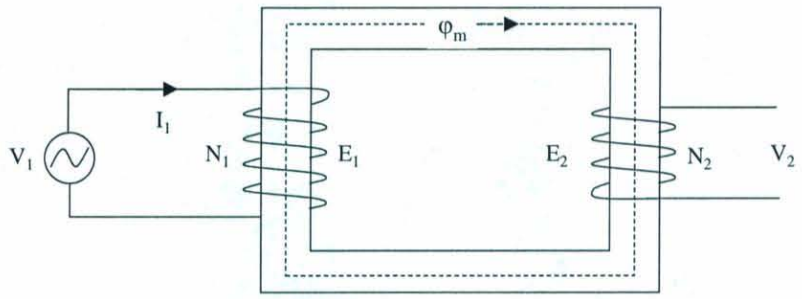

Figure 3.6: An Ideal Transformer

In a two winding transformer, the windings are magnetically coupled and it is hard to analyze. Therefore, the ideal transformer is converted to its equivalent circuit for the purpose of easy computation. The parameters like resistance, reactance, voltage and current can be transferred either from primary to secondary or from secondary to primary in the equivalent circuits. The magnitude of no-load circuit current is very small and it is less than 5% of the rated primary current. Hence in the equivalent circuit the no-load circuit can be neglected without making any serious error. The two winding ideal transformer is shown in Figure 3.7.

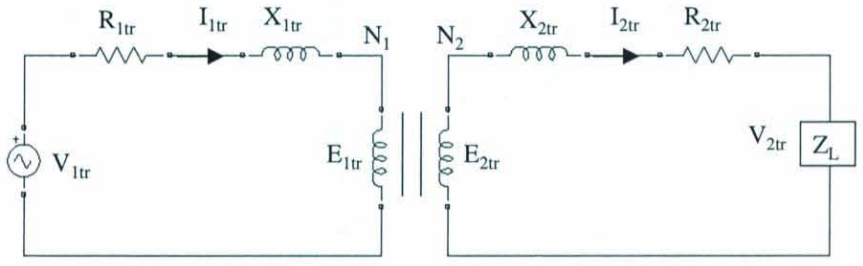

Figure 3.7: A Two-Winding Transformer

The equivalent circuits referred to primary and secondary are depicted in Figure 3.8 and 3.9 respectively. In the case of former one, all parameters are transferred from secondary to primary. These parameters are,

$$R'_{2tr} = a^2 R_{2tr} \tag{3.3.28}$$

$$X'_{2tr} = a^2 X_{2tr} \tag{3.3.29}$$

$$Z'_L = a^2 Z_L \tag{3.3.30}$$

$$I'_{2tr} = \frac{I_{2tr}}{a} \tag{3.3.31}$$

Combined resistance referred to primary,

$$R_{01} = R_{1tr} + R'_{2tr} = R_{1tr} + a^2 R_{2tr} \tag{3.3.32}$$

Combined reactance referred to primary,

$$X_{01} = X_{1tr} + X'_{2tr} = X_{1tr} + a^2 X_{2tr} \tag{3.3.33}$$

The voltage across load,

$$V'_{2tr} = aV_{2tr} \tag{3.3.34}$$

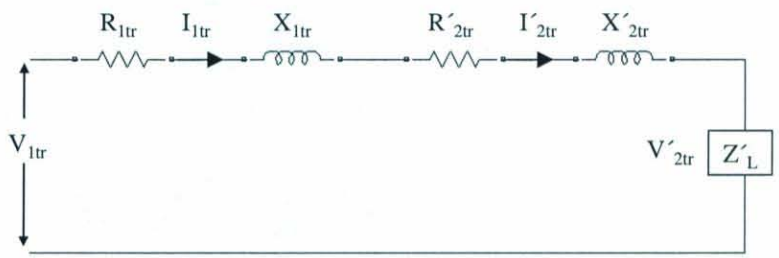

Figure 3.8: Equivalent Circuit Referred to Primary

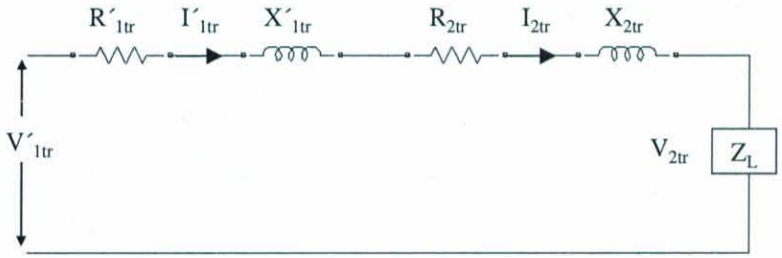

Figure 3.9: Equivalent Circuit Referred to Secondary

In the similar fashion, it is possible to express all the parameters transferred from primary to secondary side to form the equivalent circuit referred to secondary. These shifted parameters are,

$$R'_{1tr} = \frac{R_{1tr}}{a^2} \tag{3.3.35}$$

$$X'_{1tr} = \frac{X_{1tr}}{a^2} \tag{3.3.36}$$

$$I'_{1tr} = aI_{1tr} \tag{3.3.37}$$

$$V'_{1tr} = \frac{V_{1tr}}{a} \tag{3.3.38}$$

Total resistance referred to secondary,

$$R_{02} = R_{2tr} + R'_{1tr} = R_{2tr} + \frac{R_{1tr}}{a^2} \tag{3.3.39}$$

Total reactance referred to secondary side,

$$X_{02} = X_{2tr} + X'_{1tr} = X_{2tr} + \frac{X_{1tr}}{a^2} \tag{3.3.40}$$

Where "a" is the turns ratio and expressed as,

$$a = \frac{N_1}{N_2} = \frac{V_{1tr}}{V_{2tr}} = \frac{I_{2tr}}{I_{1tr}} \tag{3.3.41}$$

3.3.7 Capacitor Bank

Due to being cheap, simple and robust in design, the squirrel cage induction generators based wind turbines have received a great attention for operating in stand-alone conditions. Although they are capable of generating active power, their limitation is that they are unable to produce reactive power needed for their own excitation. In order to mitigate this problem, a capacitor bank is connected to the system between the generator and the load or grid. Each of the 65 kW Windmatic wind turbines at Ramea has employed a 35 kVAR rated capacitor bank. As the three phase capacitor bank is connected to the induction generator, an emf is induced to the machine windings due to the self excitation provided by the capacitors. The magnetizing requirements of the machines are met these capacitors. In order to create the self excitation by this capacitor bank, the following two conditions should be fulfilled [15, 59].

i. The rotor of the machine should have sufficient residual magnetism and

ii. The three phase capacitor bank should be of sufficient value.

After satisfying the above conditions an emf will be induced in the machine windings due to the excitation provided by the capacitors. This phenomenon is known as "Capacitor Self-Excitation". If the induced emf is sufficient, leading currents through the capacitors will circulate.

3.4 Power Extraction from the Wind

In WECS energy conversion takes place in two levels. At first, the wind energy is converted to mechanical energy and WT rotor does this conversion. Finally, this mechanical energy is fed to the generator which produces the electrical energy. After that different schemes, composed of converter/inverter sets, chopper circuit and power electronic switches, are deployed for power shaping or maximum power extraction. Assuming not yaw misalignment, wind turbine's energy conversion technique is governed by equation (3.4.1) as follows [9, 12].

$$P_t = \frac{1}{2}\rho A C_p(\lambda, \beta) v_w^3 \tag{3.4.1}$$

where P_t is the mechanical power generated by the turbine, ρ is the air density, A is the turbine swept area, C_p is the performance coefficient and v_w is the wind speed. This equation reveals that C_p is a function of the Tip Speed Ratio (TSR), λ and the pitch angle β. The pitch angle is fixed for both the turbines and the mechanical power depends on C_p-λ curve. C_p-λ relationship is characterized by following two equations

$$C_p(\lambda, \beta) = c_1\left(\frac{c_2}{\lambda_1} - c_3\beta - c_4\right)e^{\frac{-c_5}{\lambda_1}} + c_6\lambda \tag{3.4.2}$$

$$\frac{1}{\lambda_1} = \frac{1}{\lambda + 0.08\beta} - \frac{0.035}{\beta^3 + 1} \tag{3.4.3}$$

where c_1 - c_6 are the coefficients. TSR can be measured by the ratio of the rotor speed at the tip to the wind speed. Mathematically it is expressed by the following equation.

$$\lambda = \frac{\omega R}{v_w} \tag{3.4.4}$$

where ω is the rotational speed and R is the radius of the turbine. When the wind blows over the cut-in speed, the turbine rotates and the same time it produces some torque which is associated with produced mechanical energy. This behavior is articulated by

$$T_t = \frac{P_t}{\omega} \tag{3.4.5}$$

where T_t is the turbine torque.

More generalized equation of turbine torque can be formulated after combining equations (3.4.1), (3.4.4) and (3.4.5) as follows

$$T_t = \frac{1}{2}\rho AR\frac{C_p(\lambda,\beta)}{\lambda}v_w^2 = \frac{1}{2}\rho ARC_q(\lambda,\beta)v_w^2 \tag{3.4.6}$$

Here C_q is the torque coefficient and is defined as

$$C_q(\lambda,\beta) = \frac{C_p(\lambda,\beta)}{\lambda} \tag{3.4.7}$$

3.5 Modeling and Simulation of WM15S Wind Turbines

It has been mentioned early that, at Ramea there are six squirrel cage induction generator based fixed speed wind turbines operating at present. Each of these WECS supports dual-speeds, i.e. this system has two parallel generators connected to the rotor shaft. One is rated at 65 kW and other is at 13 kW. The system is arranged in such a way that if the wind speed exceeds 8m/s, the larger generator will run and smaller one will operate for

the wind speed below 8m/s. This analogy is described in Figure 3.10. In such a topology the larger and the smaller generators rotate at 1212 rpm and 1230 rpm respectively.

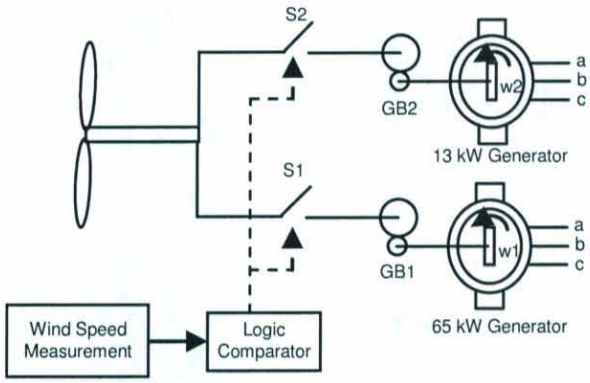

Figure 3.10: The 65 kW wind generator and control

The mechanical components and the electrical characteristics of this WECS have been illustrated thoroughly in section 3.3. The further specifications obtained from [46, 55] are outlined in Table 3.1.

Basically a steady state model has been developed here in this section and it is intended to compute that how the energy is being produced with different levels of wind speeds. The 65 kW WECS shown in Figure 3.11 includes the turbine, generator and other mechanical accessories as of the practical systems. The detailed components of this subsystem belong to Appendix A. Table 3.2 unveils the parameters used in the simulation model. Finally, the power from WECS at different wind speeds and the speed characteristics of the generators will be recounted in Figure 3.12 and 3.13 as follows. It has been found that at 5 m/s wind speed the power generated from the wind turbine is 0.245 kW. At the base wind speed (8 m/s) and the rated speed (15 m/s) the energy

productions become 23.95 kW and 65.76 kW respectively. It is perceptible that when the wind speed belong to the range from the cut-in speed to below 8 m/s, the smaller generator will operate and the larger generator will run at or greater than 8 m/s wind speed. Moreover, the smaller and the larger generator speeds have been recorded as 1203 rpm and 1228 rpm sequentially from the simulations.

Parameters	Value/Specification	Parameters	Value/Specification
Connection to Mains		**Nacelle**	
Voltage	480 V	Cover Material	Aluminium
Frequency	60 Hz	Mass	3990 kg
Performance		**Main Bearings**	
Cut-in Wind Speed	3.5 m/s	Number	2
Wind Speed for Max. Power	15 m/s		
Cut-out Wind Speed	25 m/s	**Operation Brake**	
Maximum Electric Power	66 kW	Type	Disc Brake
		Location	Turbine Shaft
Turbine		Operation	Hydraulic
Type	3 blades, Stall Regulated, Upwind		
Diameter	15.5 m	**Gearbox**	
Rotational Speed	40-41 rpm / 57-58 rpm	Number of Stages	3
Tilt Angle	5 Degree	Gear Ratio	1:20.83
Cone Angle	0 Degree		
Mass	1180 kg	**Generator**	
		Type	Asynchronous with Squirrel Cage
Blades			
Beam Material	Reinforced fiber-glass polyester with steel root	**Small Generator**	
Shell Material	Reinforced fiber-glass polyester	Rated Electrical Power	13 kW
Aerofoil	NACA 63-200	Rated Speed	1230 rpm
Pitch	Fixed		
		Large Generator	
Aerodynamic Brakes		Rated Electrical Power	66 kW
Type	Spoilers	Rated Speed	1212 rpm

Table 3.1: Specifications of WM15S Wind Turbines

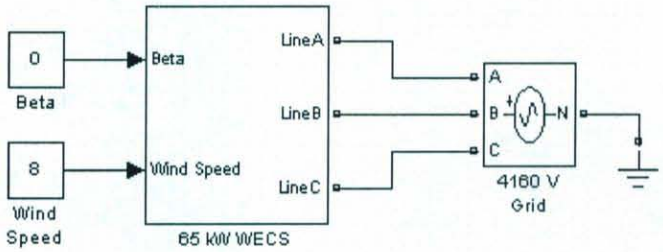

Figure 3.11: The Steady State model of 65 kW wind generator

Parameters	Values		Parameters	Values
Turbine			**65 kW Machine**	
Nominal Mechanical Output Power	65 kW		Stator Resistance	0.0414 Ω
Base Power of the Electrical Generator	65 kVA		Stator Inductance	1.04 mH
Base Wind Speed	8 m/s		Rotor Resistance	0.1872 Ω
Pitch Angle	0 Degree		Rotor Inductance	1.19 mH
			Mutual Inductance	32.36 mH
3-φ Transformer			Inertia	0.834 kg-m2
Nominal Power	225 kVA		Pole Pairs	3
Primary Winding Voltage	480 V			
Primary Winding Resistance	0.01 pu		**13 kW Machine**	
Primary Winding Inductance	0.01 pu		Stator Resistance	0.105 Ω
Secondary Winding Voltage	4160 V		Stator Inductance	7.427 mH
Secondary Winding Resistance	0.01 pu		Rotor Resistance	1.12 Ω
Secondary Winding Inductance	0.01 pu		Rotor Inductance	7.427 mH
Magnetization Resistance	0.5 pu		Mutual Inductance	80 mH
Magnetization Inductance	0.2 pu		Inertia	0.4248 kg-m2
			Pole Pairs	3

Table 3.2: Parameters of 65 kW WECS Used for Simulation

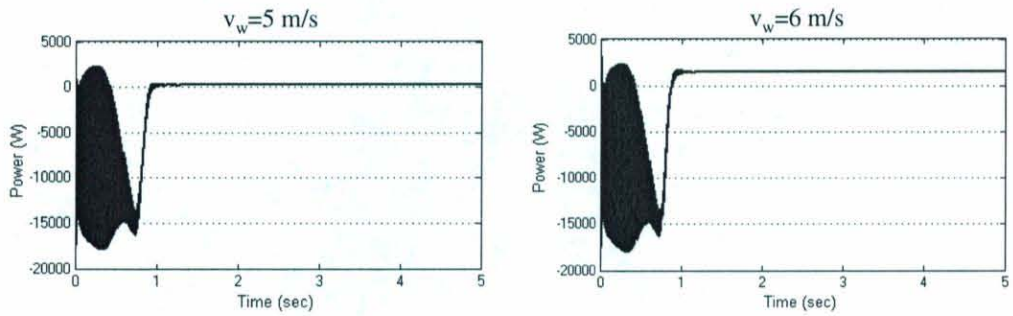

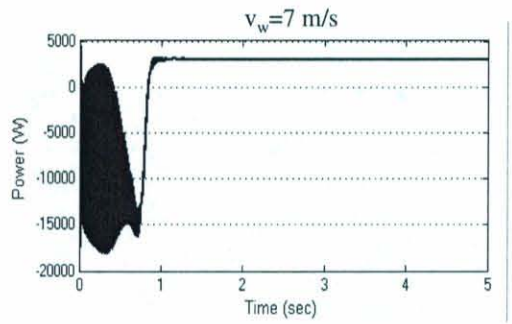
v_w=7 m/s
Power (W)
Time (sec)

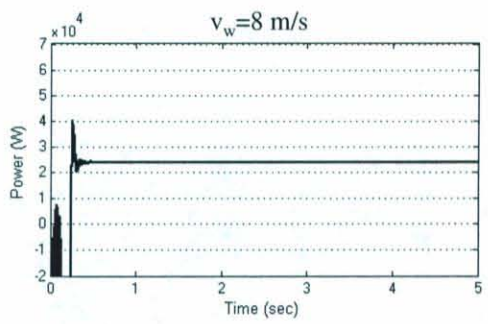
v_w=8 m/s
Power (W)
Time (sec)

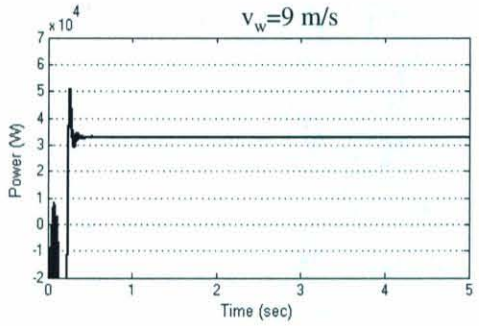
v_w=9 m/s
Power (W)
Time (sec)

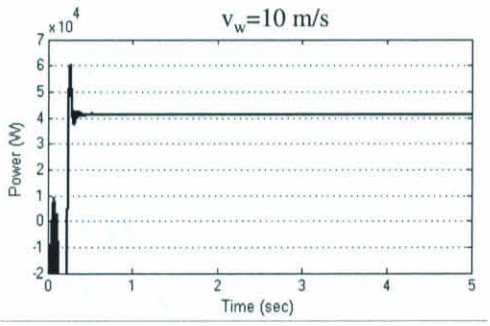
v_w=10 m/s
Power (W)
Time (sec)

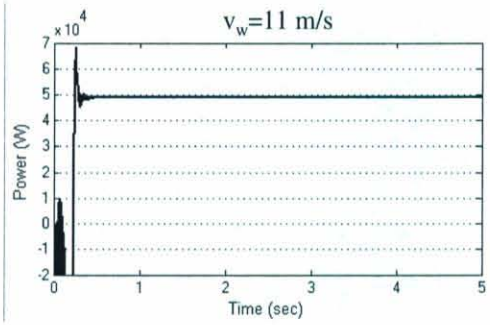
v_w=11 m/s
Power (W)
Time (sec)

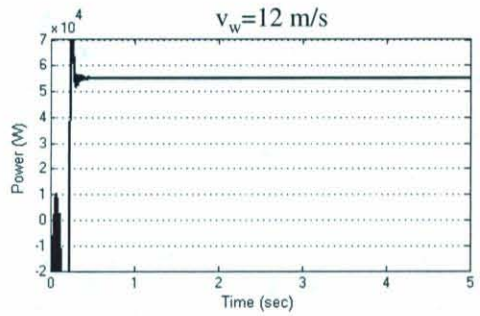
v_w=12 m/s
Power (W)
Time (sec)

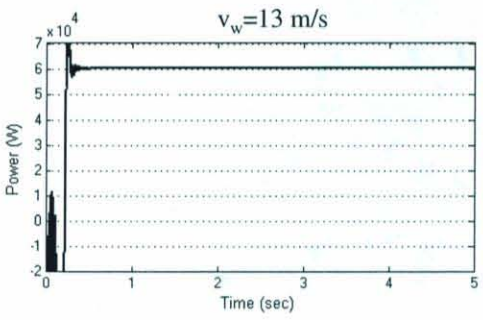
v_w=13 m/s
Power (W)
Time (sec)

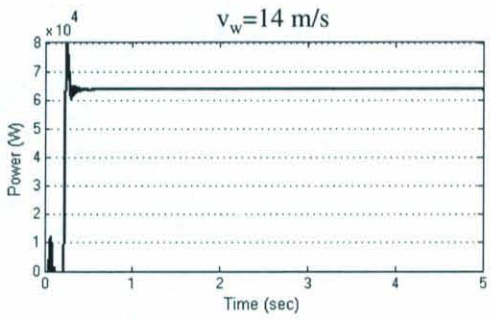
v_w=14 m/s
Power (W)
Time (sec)

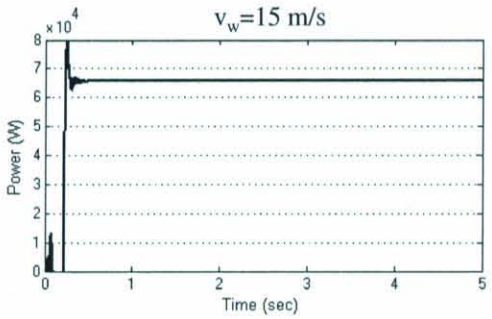

Figure 3.12: Power Generation by 65 kW WECS at Different Wind Speeds

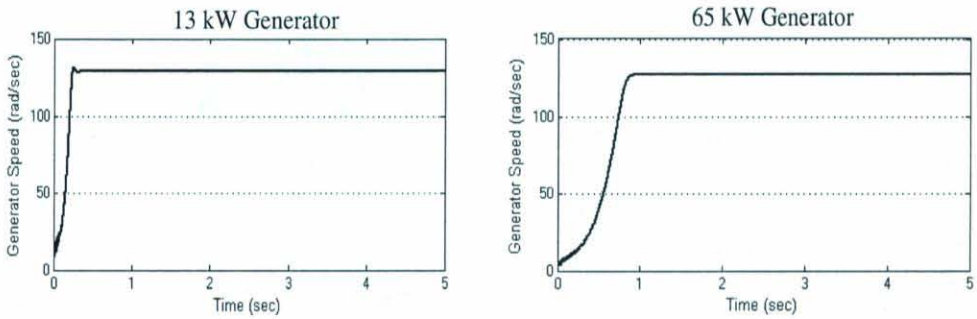

Figure 3.13: Fixed Smaller and Larger Generator Speeds While Producing Power

3.6 Modeling and Simulation of NW100 Wind Turbines

The NW100 is a direct drive permanent magnet synchronous generator based wind turbine. Northwind Power System is their manufacturer. From [54] some specifications regarding such kind of WECS have been obtained which is delineated in Table 3.3.

Parameters	Values/Specifications		Parameters	Values/Specifications
General Configuration			**Drive Train**	
Power Regulation	Variable Speed Stall Control		Generator System	Direct Drive, Permanent Magnet
Rotor Diameter	21 m		Gearbox type	No gearbox
Orientation	Upwind			
Hub Height	37 m		**Braking System**	
Design Life	20 Years		Service Brake Type	Spring Applied Caliper
			Normal Shutdown Brake	Dynamic Brake
Performance				
Rated Electrical Power	100 kW, 480 VAC, 3 Phase		**Control/Electrical System**	
Rated Wind Speed	14 m/s		Controller Type	DSP Micro-processor Based CPU
Rated Rotation Speed	59 rpm		Power Factor	Unity or 0.9 lagging to 0.9 leading selectable
Cut-in Speed	3 m/s			
Cut-out Speed	25 m/s		**Weight**	
Survival Wind Speed	60 m/s		Rotor	1350 kg
			Nacelle	5200 kg

Table 3.3: Specifications of NW100 Wind Turbines

The wind turbine model developed in MATLAB/SIMULINK is revealed in Figure 3.14. This model has been generated based on equations 3.4.1-3.4.4. Basically the C_p-λ curve has been set in such a way that the turbine is constrained by desired characteristics. The power outputs from this model are comparable to that picked from the manufacturer's specification sheet. The simulation results are depicted in Table 3.4 as follows.

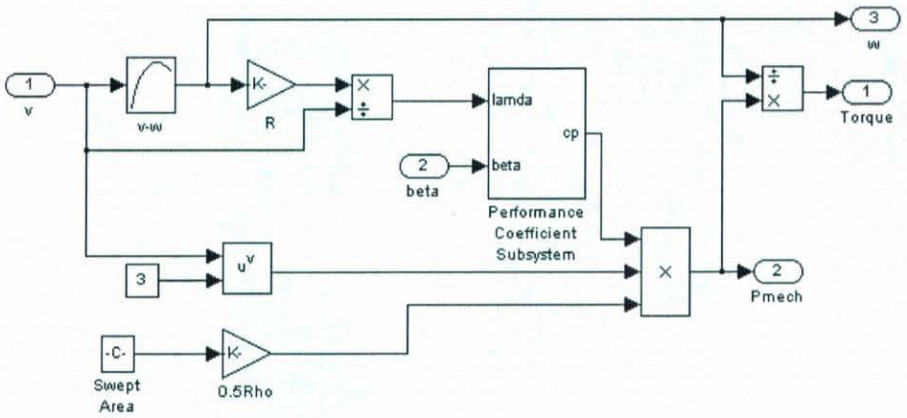

Figure 3.14: 100 kW Wind Turbine Model

Wind Speed (m/s)	Mechanical Power (kW)	Generator Speed (rpm)
4	3.71	26.22
5	10.50	41.66
6	19.00	51.52
7	29.38	59.08
8	41.04	64.71
9	54.27	69.45
10	66.79	71.97
11	77.56	72.41
12	86.48	71.22
13	92.69	68.13
14	99.49	65.08
15	100.20	58.59

Table 3.4: Output Mechanical Power and Generator Speed of NW100 Wind Turbine at Different Wind Speeds

These parameter values are fairly acceptable but the information regarding connection between the permanent magnet synchronous generator and the grid and their control strategies are absent in the specification sheet. Therefore this research considers the 100 kW WECS associated with an induction generator connected directly to grid through an externally excited capacitor bank.

Other than some parameters, the basic configuration of this 100 kW WECS is same as that of 65 kW WECS shown in Figure 3.12. For example, the 100 kW wind turbine is considered to rotate at 60 rpm fixed speed. A gearbox is assumed in the drive train having the gear ratio of 30:1 and hence the generator rated speed has turned to 1800 rpm. The specifications used for simulation is highlighted in Table 3.5 below.

Parameters	Values		Parameters	Values
Turbine			Inertia	0.834 kg-m2
Nominal Mechanical Output Power	100 kW			
Base Power of the Electrical Generator	100 kVA		**3-φ Transformer**	
Base Wind Speed	8 m/s		Nominal Power	150 kVA
Pitch Angle	0 Degree		Primary Winding Voltage	480 V
			Primary Winding Resistance	0.01 pu
65 kW Machine			Primary Winding Inductance	0.01 pu
Stator Resistance	0.0414 Ω		Secondary Winding Voltage	4160 V
Stator Inductance	1.04 mH		Secondary Winding Resistance	0.01 pu
Rotor Resistance	0.1872 Ω		Secondary Winding Inductance	0.01 pu
Rotor Inductance	1.19 mH		Magnetization Resistance	0.5 pu
Mutual Inductance	32.36 mH		Magnetization Inductance	0.2 pu
Pole Pairs	3			

Table 3.5: Parameters of 100 kW WECS Used for Simulation

The simulation results of this WECS at different wind speeds and the fixed generator speed are interpreted in Figure 3.15 and 3.16 as follows. 2.72 kW, 45.22 kW and 96 kW are the generated powers from the wind turbines corresponding to cut-in, base and rated wind speeds respectively from the simulation results. The fixed generator speed has been computed as 1748 rpm.

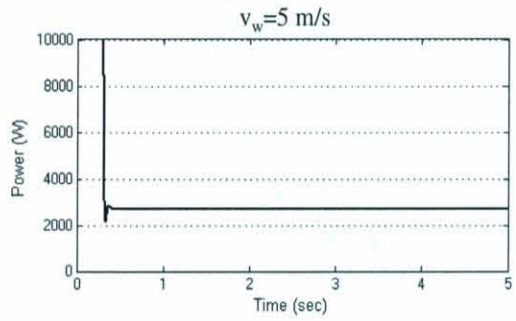
v_w=5 m/s
Power (W)
Time (sec)

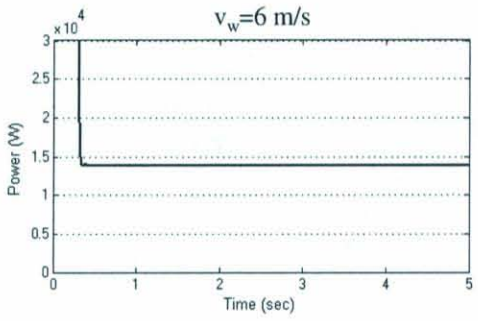
v_w=6 m/s
x 10^4
Power (W)
Time (sec)

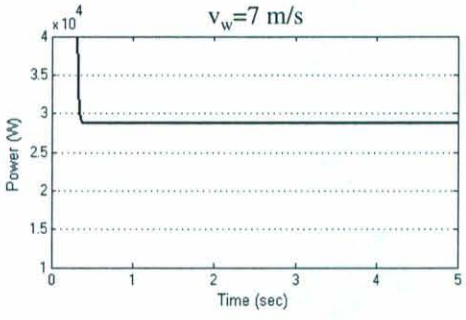
v_w=7 m/s
x 10^4
Power (W)
Time (sec)

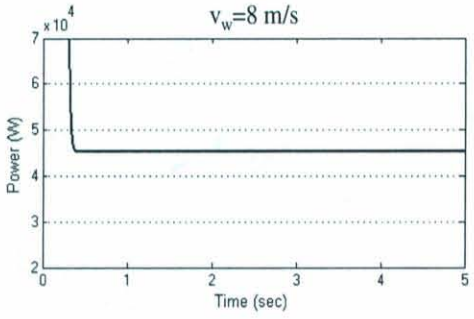
v_w=8 m/s
x 10^4
Power (W)
Time (sec)

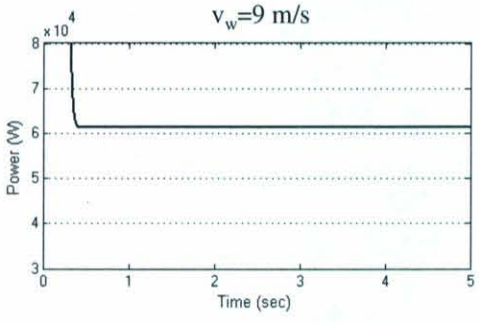
v_w=9 m/s
x 10^4
Power (W)
Time (sec)

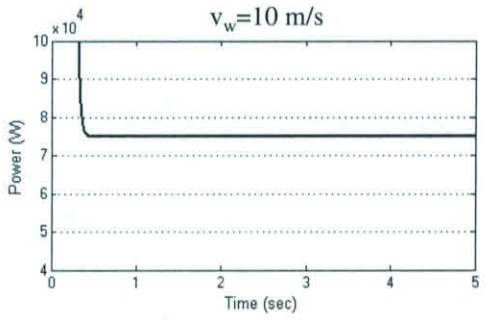
v_w=10 m/s
x 10^4
Power (W)
Time (sec)

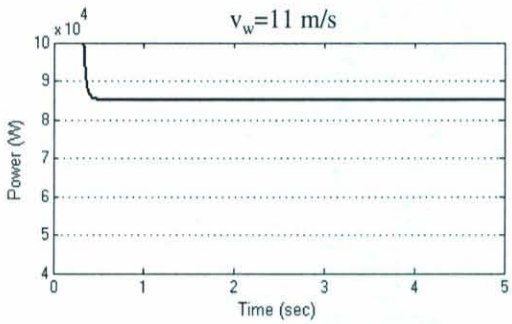
v_w=11 m/s
x 10^4
Power (W)
Time (sec)

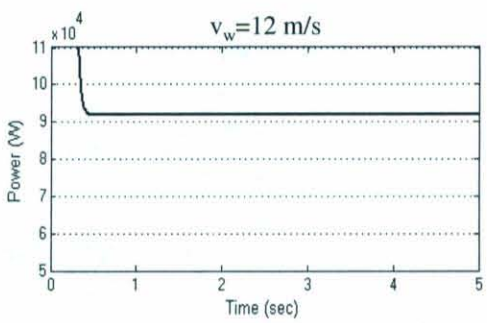
v_w=12 m/s
x 10^4
Power (W)
Time (sec)

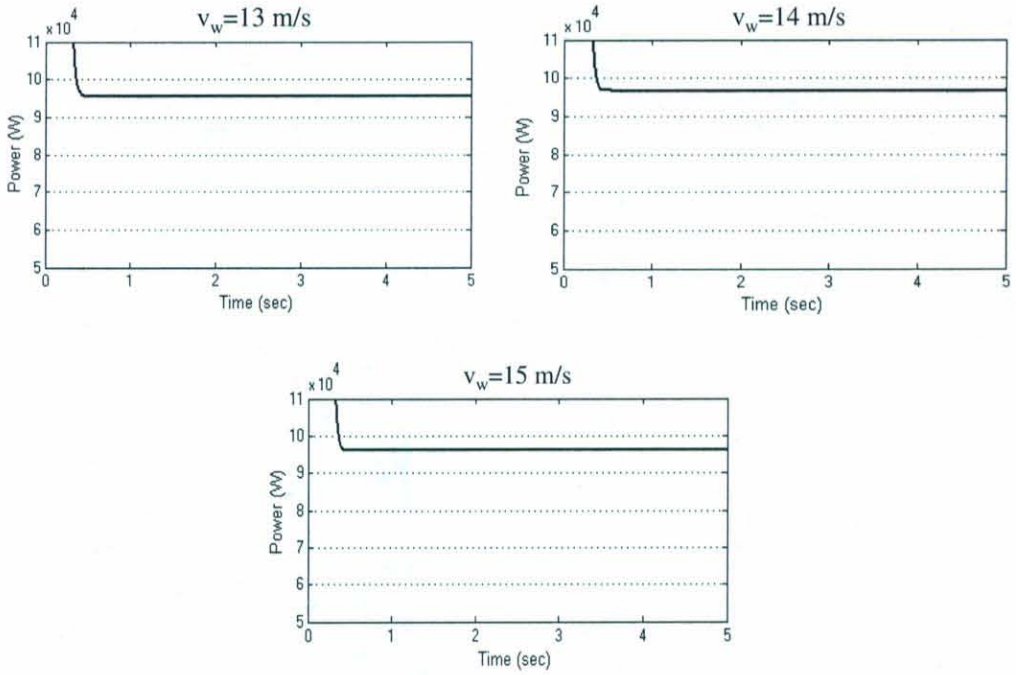

Figure 3.15: Power Generation by 100 kW WECS at Different Wind Speeds

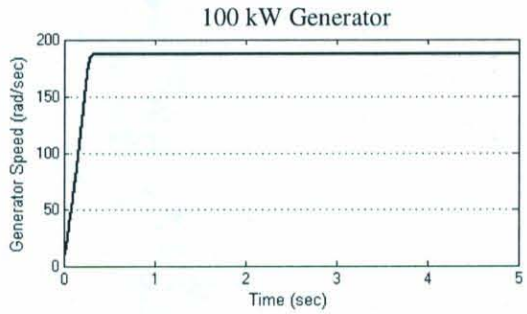

Figure 3.16: Fixed 100 kW Generator Speed While Producing Power

3.7 Summary

This chapter illustrates all about wind energy conversion systems employed in Ramea. The mechanical parts of the WECS, the machines, transformers and capacitor banks have

been expounded with their working principles and their necessities for being used in this system. The authors intended to develop the steady state models of the WECS and determine how those models react with different wind speeds, aiming to compare the power curves found from simulation results and the same provided by the manufacturers. Figure 3.17 and 3.18 elucidate those comparisons.

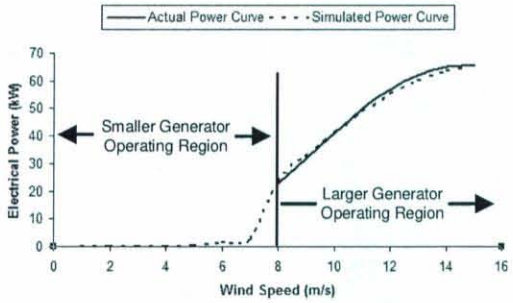

Figure 3.17: Power Versus Wind Speed Curve of 65 kW Wind Turbine

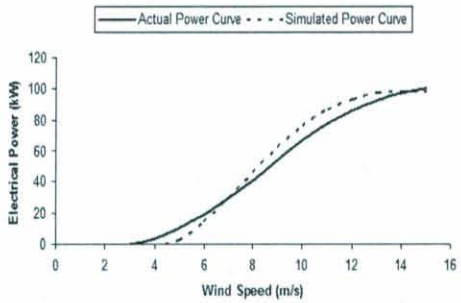

Figure 3.18: Power Versus Wind Speed Curve of 100 kW Wind Turbine

It is quite clear that, the above two figures validate the generated WECS models and they exhibit almost similar characteristics corresponding to what the manufacturer provided. The 65 kW wind turbine, in Figure 3.17, supports dual-speed, i.e. wind speed below 8 m/s allows the smaller generator to run while the larger generator will operate if the wind speed exceeds that value. Figure 3.17 seems that there is no actual power generated from the small generator. But at 5 m/s, 6 m/s and 7 m/s wind speeds, the active power recorded from the simulations are 0.25 kW, 1.48 kW and 3.05 kW respectively. The vertical line is unraveling the two operating regions. In Figure 3.18 the simulated power curve is little bit deviated from the actual curve. Considering different electrical generation scheme might be the reason for slight deflection of the power curve in certain wind speeds.

Chapter 4

Modeling of Hydrogen System

4.1 Hydrogen System in Ramea Network

If the environmental benefits of the long-term development of the hydrogen economy are to be realized, the production of hydrogen via electrolysis from RE sources will be a vital component. Today's commercially available electrolyzers are designed to use the grid electricity, produce well regulated DC power to the electrolysis stack and condition the output hydrogen for applications different than that required by fuel cells or hydrogen generators. The key element in hydrogen production from any electrical source is the electrolyzer stack that converts water and electricity into hydrogen, oxygen and heat. The electrolyzer stack needs a nearly constant, low-voltage DC and also some form of control system and power electronics to connect it to a high voltage, AC source of power.

One of the primary intents of this research work is to design a system capable of running accurately in fluctuating conditions of important system variables. The goal of

the experimental characterization of the stack, under varying conditions and load demands, is to enable an optimized interconnection between the stack and the grid. Such a coupled system specifically designed with the RE sources, would reduce the overall cost of independent stand-alone systems compared to diesel powered systems as illustrated in Chapter 2.

The hydrogen system at Ramea combines the alkaline type electrolyzer, hydrogen tanks, hydrogen engines and generators altogether. Electrical power provided to the electrolyzer in such a system would be the excess wind power provided to the grid. Thus, a combined system would have more dispatch-ability than a wind diesel alone system. Such dispatch-ability might be used to provide the utility with a measure of control the systems. Apart from the diesel generators, using a variable RE source, like wind or PV, to generate the hydrogen gas will guarantee this energy carrier is produced with nearly zero emissions.

4.2 Modeling of Alkaline type Electrolyzer

Hydrogen as an energy carrier and potentially widely-used fuel is attractive because it can be produced easily without emissions by splitting water. In addition, the readily available electrolyzer can be used in a home or business where off-peak or surplus electricity could be used to make the environmentally friendly gas. Two electrolyzer technologies, alkaline and proton exchange membrane (PEM), exist at the commercial level with solid oxide electrolysis in the research phase. However, a number of research projects regarding this technology have already been carried out [62-66] and some are being continued.

Electrolysis is defined as splitting apart with an electric current. Decomposition of the water occurs when a DC current is passed between two electrodes engrossed in water separated by a non-electrical conducting aqueous or solid electrolyte to transport ions and completing the circuit. The voltage applied to the cell must be greater than the free energy of formation of water plus the corresponding activation and ohmic losses before dissolution will proceed. Ion transport through the electrolyte is critical as the purest of water would only contain small amount of ions making it a poor conductor.

The HySTAT^{TM}-A 1000D-30-25 outdoor version 200 kW alkaline type electrolyzer is considered in this research. It has been manufactured by Hydrogenics Corporation [60] and been installed with all its utility equipments at Ramea, Newfoundland in 2009. The cell voltage, Faraday efficiency, energy efficiency, hydrogen production, heat loss, auxiliary cooling demand and some other related parameters are studied and presented below graphically along with their time dependency. The following section will cover the chemical representation of this electrolyzer along with the empirical relations by electro-chemical and thermal point of view.

4.2.1 Chemical Representation

A DC current is required to split the water molecule into hydrogen and oxygen. This current should flow between two electrodes (Anode and Cathode) separated by the electrolyte. Here the electrolyte is 30% wt. KOH. Internal structure is shown in Figure 4.1. The reactions at anode, cathode and the total reaction for water splitting are [33],

Anode reaction:

$$2OH^-(aq) \rightarrow \frac{1}{2}O_2(g) + H_2O(l) + 2e^- \quad (4.2.1)$$

Cathode reaction:

$$2H_2O(l) + 2e^- \rightarrow H_2(g) + 2OH^-(aq) \quad (4.2.2)$$

Total:

$$H_2O(l) \rightarrow H_2(g) + \frac{1}{2}O_2(g) \quad (4.2.3)$$

where, ΔH=286 kJ/mole.

Reversible voltage is the minimum voltage required for starting the water electrolysis. In this study the value of reversible voltage is 1.228V per cell. As water is not a good electric conductor, KOH is added to increase the conductivity level of the electrolyte.

Anode is made of nickel (Ni), cobalt (Co) and iron (Fe) while, cathode is made of nickel and platinum activated carbon catalyst (C-Pt) are used instead of normal electrodes to ensure that those can prevent corrosion in alkaline solution and have good electric conductivity. On the other hand the diaphragm should have low electric resistance; that is why nickel oxide (NiO) is used as diaphragm element. Figure 4.1 also reveals the chemical reactions taking place in the electrolyte.

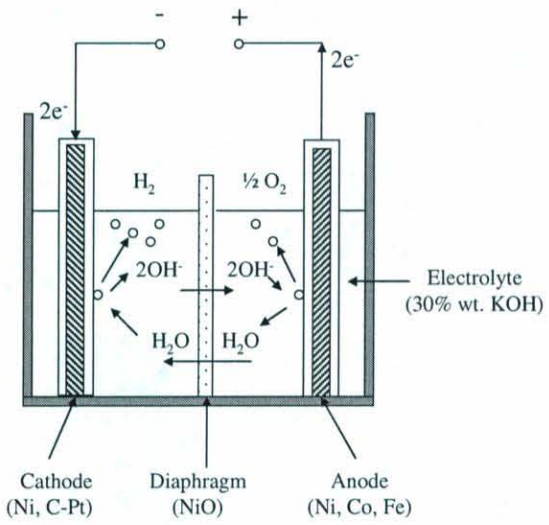

Figure 4.1: Internal Structure of an Alkaline Electrolyzer

4.2.2 Electrochemical Model

The kinetic properties around the electrodes in an electrolyzer cell can be modeled based on empirical data of different proposed I-V curves. The basic relationship between current and cell voltage in a given temperature is,

$$V = V_{rev} + \frac{I}{A} r + s \log(\frac{I}{A} t + 1) \qquad (4.2.4)$$

where I is the current required for the electrolysis, A is the area of electrodes, r is the parameter related to ohmic resistance of the electrolyte, s and t are the over voltage coefficients on electrodes and V_{rev} is the reversible voltage.

The reversible voltage can be expressed as,

$$V_{rev} = \frac{\Delta G}{zF} \tag{4.2.5}$$

where ΔG is Gibb's energy, z is the number of electrons transferred in each reaction (here it is 2) and F is the Faraday constant. In standard condition (25° C and 1 bar), the change of Gibb's energy of water splitting is ΔG° = 237 kJ/mol.

In addition to that, ΔH is the change of enthalpy between reactants and products in a reaction and is related to thermo neutral cell voltage as

$$V_{tn} = \frac{\Delta H}{zF} \tag{4.2.6}$$

The energy required for water splitting in standard condition, ΔH° = 286 kJ/mol.

In order to relate the ohmic resistance parameter, r and over voltage coefficient, t the equation (4.2.4) can be modified in more detailed way as

$$V = V_{rev} + \frac{I}{A}(r1 + r2 \times T) + s\log[\frac{I}{A}(t1 + \frac{t2}{T} + \frac{t3}{T^2}) + 1] \tag{4.2.7}$$

Faraday efficiency is the proportion of the actual and theoretical hydrogen production in the electrolyzer [33]. It will be shown later that one of the parameters that control the hydrogen production is current, so another name of Faraday efficiency is current efficiency. It can be noted that parasitic current increases with the decrement of current density and the increment of temperature resulting the reduction of Faraday efficiency. This phenomenon can be expressed as,

$$\eta_F = \frac{(I/A)^2}{f_1 + (I/A)^2} f_2 \tag{4.2.8}$$

where f_1 and f_2 are the parameters related to Faraday efficiency.

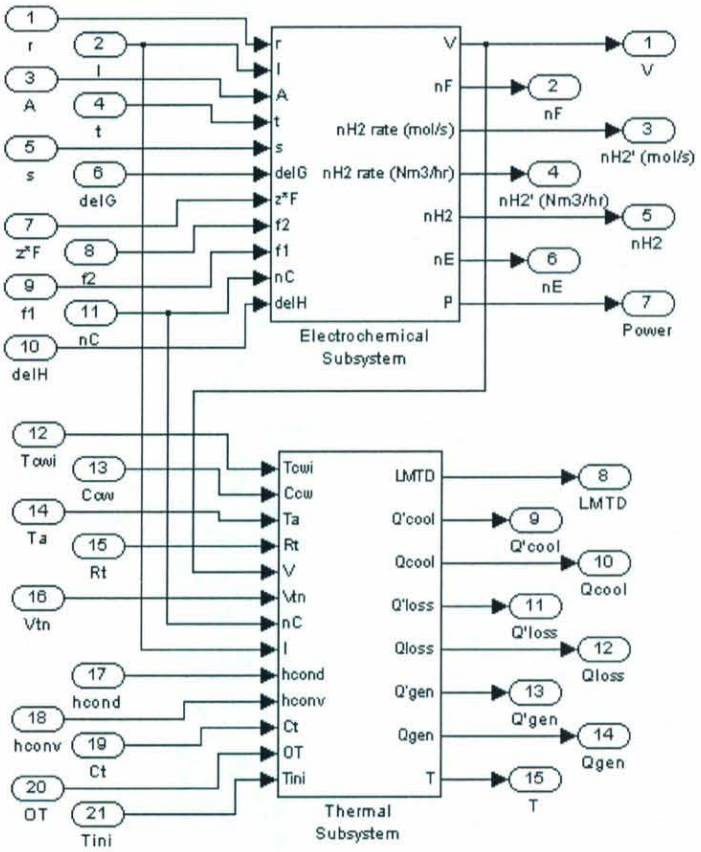

Figure 4.2: Simulink Model of the Electrolyzer

Normally a number of electrolyzer cells are connected in series in a stack and some stacks are connected in parallel. The number of such electrolyzer cells has an impact on the total hydrogen production. The production rate is

$$\dot{n}_{H2} = \eta_F \frac{n_c I}{zF} \tag{4.2.9}$$

where n_c is the number of electrolyzer cells per stack.

Energy efficiency is defined as the ratio of thermo neutral voltage and the cell voltage as follows

$$\eta_e = \frac{V_{tn}}{V} \tag{4.2.10}$$

It is notable that, the electrical inefficiencies result in the unwanted heat generation in the electrolyzer which has an indirect influence on Faraday efficiency. The dynamic model describing electrochemical property is shown in Figure 4.2.

4.2.3 Thermal Model

Like the electrochemical model, the cell temperature can be calculated using either simple or complex thermal model. Considering the electrolyzer as a lumped thermal capacitance model the overall energy balance will be

$$C_t \frac{dT}{dt} = Q'_{gen} - Q'_{loss} - Q'_{cool} \tag{4.2.11}$$

$$Q'_{gen} = n_c I(V - V_{tn}) = n_c VI(1 - \eta_e) \tag{4.2.12}$$

$$Q'_{loss} = \frac{1}{R_t}(T - T_a) \tag{4.2.13}$$

$$Q'_{cool} = C_{cw}(T_{cwi} - T_{cwo}) = VA_{HX} LMTD \tag{4.2.14}$$

where C_t is overall thermal capacity of electrolyzer, T is the temperature in Kelvin, Q'_{gen} is the internal heat generation, Q'_{loss} is the total heat loss to the ambient, Q'_{cool} is the auxiliary cooling demand, R_t is the overall thermal resistance of the electrolyzer, T_a is the ambient temperature, C_{cw} is the thermal capacity of the cooling water, T_{cwi} is the

temperature of the inlet cooling water, T_{cwo} is the temperature of outlet cooling water, VA_{HX} is the overall heat transfer coefficient and area product of heat exchanger and LMTD is the log mean temperature difference.

The log mean temperature difference relates the temperature of electrolyte with that of inlet and outlet cooling water

$$LMTD = \frac{(T - T_{cwi}) - (T - T_{cwo})}{\ln[\frac{(T - T_{cwi})}{(T - T_{cwo})}]} \tag{4.2.15}$$

As this study includes the dynamic modeling, it will be more viable to analyze the differential equations and calculate temperature directly. But before that another unknown parameter, outlet cooling water temperature should be calculated first.

$$T_{cwo} = T_{cwi} + (T - T_{cwi})[1 - \exp(-\frac{VA_{HX}}{C_{cw}})] \tag{4.2.16}$$

Using equation (12), (13), (14) and (16) the overall thermal energy balance from the basic equation (11) will become

$$\frac{dT}{dt} + AT - B = 0 \tag{4.2.17}$$

which has the solution of

$$T(t) = (T_{ini} - \frac{B}{A})\exp(-A \times OT) + \frac{B}{A} \tag{4.2.18}$$

where T_{ini} is the initial temperature of the electrolyzer, OT is its operating time, A and B are the arbitrary constants whose expressions are

$$A = \frac{1}{\tau_t} + \frac{C_{cw}}{C_t}[1 - \exp(-\frac{VA_{HX}}{C_{cw}})] \tag{4.2.19}$$

$$B = \frac{n_c VI(1-\eta_e)}{C_t} + \frac{T_a}{\tau_t} + \frac{C_{cw}T_{cwi}}{C_t}[1-\exp(-\frac{VA_{HX}}{C_{cw}})] \quad (4.2.20)$$

where τ_t is thermal time constant and represented by the product of C_t and R_t.

Empirically it has been found that there is an indirect relationship between VA product and the electrolyzer current. Hence the relationship proposed by the author [1]

$$VA_{HX} = h_{cond} + h_{conv} I \quad (4.2.21)$$

where h_{cond} and h_{conv} are the parameters related to conduction heat transfer and convection heat transfer respectively. Figure 4.2 shows the dynamic thermal model of the electrolyzer in simulink. The subsystems of electrochemical and thermal models are described in Appendix A.

4.2.4 Electrolyzer Simulation Results

The HySTAT^{TM}-A 1000D-30-25 model provided by Hydrogenics Corporation is a 200 kW electrolyzer which is on site already. Its nominal hydrogen flow is 12-30 Nm^3/h, output pressure is 348 PSI and power requirement is 7.4 kWh/Nm^3. There are two stacks and each stack contains 90 electrolyzer cells. Although the dynamic model described here is a generalized model, some input parameters have been chosen in such a way that the output parameters match with the practical model. Some of the input parameters are specified in Table 4.1.

When the electrolyzer is off, the cell voltage will be minimum and will equal to reversible voltage (1.228 V) and when it is on, a large amount of current will flow through the cells resulting increment in voltage (near about 1.72 V) even greater than the

thermo neutral cell voltage (1.48 V) as shown in Figure 4.7. The cell voltage completely depends on current as it is the only variable term related to it [equations (4.2.4) and (4.2.7)]. The Faraday efficiency always represents the value less than 1 (here it is 0.79 in Figure 4.5). The electrolyzer becomes more efficient when the current is stepped up. As the heat generation in the electrolyzer cell is due to its inefficiency so when it remains in operation η_e decreases below 1, in other case this value is greater than 1 as shown in Figure 4.6. It is quite obvious that hydrogen production will be increased as electrolyzer current increases. As shown in Figure 4.4 the hydrogen flow rate is 19 Nm^3/h per stack which falls between the range specified by the manufacturer for the electrolyzer stack current of 650 A (Figure 4.3).

Input Parameters	**Values**
I	650 A
t	0.974 m2/A
s	0.185 V
f1	250 mA2/cm4
f2	0.78
nc	90
Tcwi	287.5 K
Ta	298 K
Ccw	4200 J/K
Rt	0.167 K/W
Vtn	1.473 V
hcond	7 W/K
hconv	0.02 W/K/A
Ct	625000 J/K

Table 4.1: Input Parameters of the Electrolyzer

In thermal model it is easy to state that inlet cooling temperature is less than the outlet cooling temperature, as a result the auxiliary cooling is a negative quantity and the

cooling rate has two steps as shown in Figure 4.11. Thermal resistance is a small quantity leading to a heat loss (see Figure 4.10) while the rate of heat loss is almost constant with time. The electrolyzer temperature is quite stable with time (see Figure 4.8), the reason is the values of arbitrary constants A and B are very small compared to initial temperature. Hence it retains almost the same temperature value for all conditions. Primarily V is less than V_{tn} causing a slight negative value of heat generation, but when the electrolyzer comes into operation as shown in Figure 4.9, the heat generation changes its direction and increases with time. Figure 4.3 shows the relationship between the input current and power consumed by the electrolyzer.

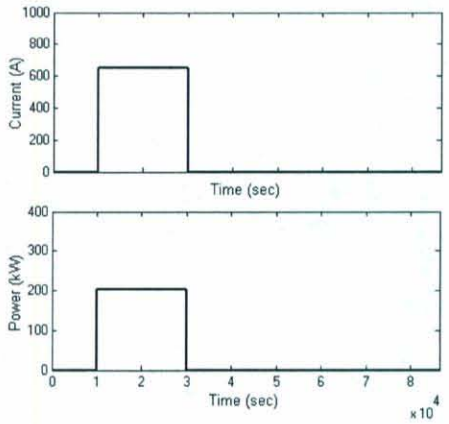

Figure 4.3: Input Current and Power Consumption

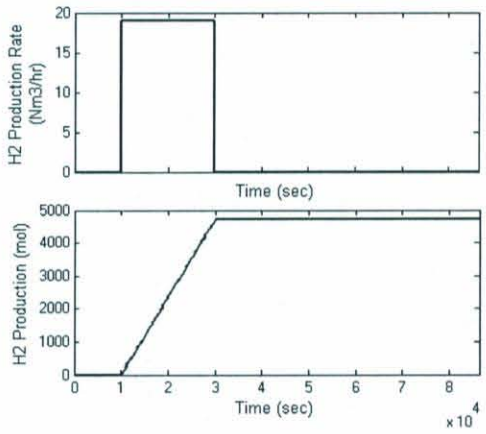

Figure 4.4: Hydrogen Production

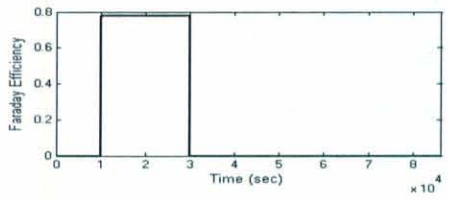

Figure 4.5: Faraday Efficiency

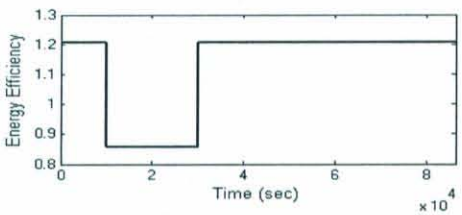

Figure 4.6: Energy Efficiency

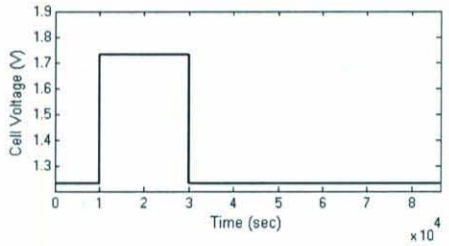

Figure 4.7: Electrolyzer Cell Voltage

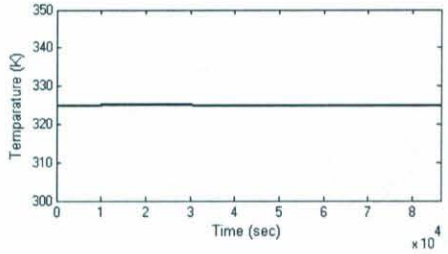

Figure 4.8: Electrolyzer Temperature

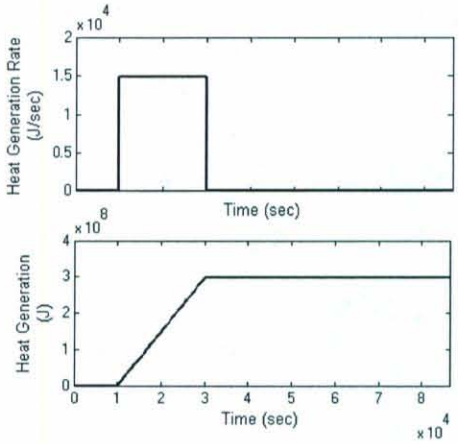

Figure 4.9: Heat Generation

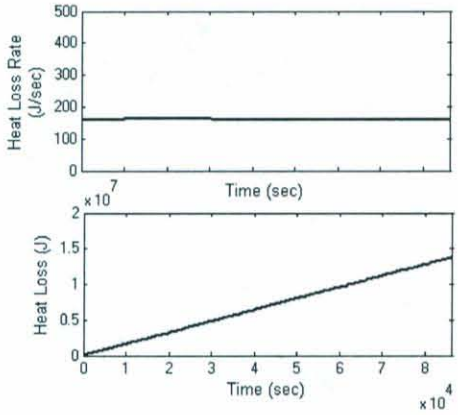

Figure 4.10: Heat Loss

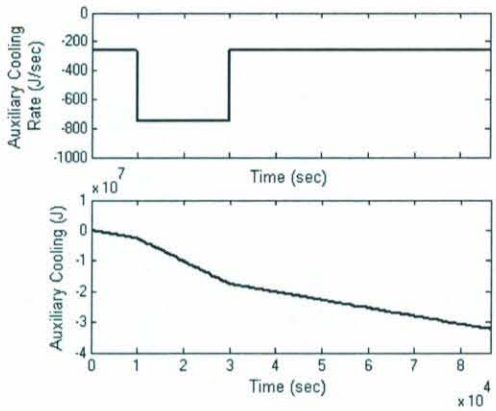

Figure 4.11: Auxiliary Cooling

4.3 Modeling of Hydrogen Tank

To date, the electrolytic production of hydrogen using renewable sources is the only way to produce large quantities of hydrogen without emitting the traditional by-products associated with fossil fuels. The electrolysis of water is an electrochemical reaction requiring no moving parts and a direct electric current, making it one of the simplest ways to produce hydrogen. The electrochemical decomposition of water into its two constituent parts has been shown to be reliable, clean and with the removal of water vapor from the product capable of producing ultra-pure hydrogen (more than 99.99%). Figure 4.12 shows the three hydrogen tanks installed near generation site at Ramea.

4.3.1 Hydrogen Tank Simulink Model

In order to overcome the intermittent behavior of the renewable sources, a stand-alone remote system can be developed where the excess of electrical energy could be converted

Figure 4.12: Three Hydrogen Tanks of 1000 Nm^3 Combined Capacity

to any other form and stored efficiently [67]. Batteries, magnetic fields and super-capacitors are some of the direct means for storing electricity. Among these, batteries are the only practical commercial devices so far but they also suffer from self-discharge and thus are relatively short-term storage devices [68]. Long term energy storage can be achieved with a time independent medium such as hydrogen. Hydrogen, having a high mass energy density, can be stored for long periods with little or no energy loss. This property makes H_2 suitable for long term energy storage.

When there is surplus amount of energy produced from the renewable sources, the electrolyzer will be operating and the hydrogen will be stored in three tanks through compressor. Three tanks have already been installed in Ramea with capacity of 333.33 Nm^3 each. Furthermore, if the deficit of energy occurs, the compressed hydrogen will be driving the generators through the hydrogen engines. There are two techniques for physical hydrogen storage, one is in the form of compressed hydrogen gas and other is the in the form of liquid hydrogen. This study incorporates the former mentioned technology. The developed hydrogen tank model discussed here directly computes the internal pressure using the ratio of hydrogen flow to the tank. It should be noted that all the auxiliary components such as pumps, control valves etc. have been ignored during model generation. The tank pressure dynamics are interpreted by the following two equations [31, 36],

$$P_b - P_{bini} = \int \frac{z\dot{n}_{H2} R T_b}{M_{H2} V_b} dt \qquad (4.3.1)$$

$$\dot{n}_{H2out} = k_f \left(P_b - P_{H2atm} \right) \qquad (4.3.2)$$

where P_b and P_{bini} are tank pressure at any instant and initial tank pressure, z is the compressibility factor of hydrogen, $\dot{n}_{H2}$ is the hydrogen inlet flow rate, R is the Universal gas constant, T_b is the operating temperature in Kelvin, M_{H2} is the molar mass of hydrogen, V_b is the tank volume, $\dot{n}_{H2out}$ is the hydrogen flow rate out of the tank, k_f is the flow constant and P_{H2atm} is hydrogen pressure outside of the tank.

Based on equation 4.3.1 and 4.3.2 the Simulink model of hydrogen tank is shown in Figure 4.13. The detailed subsystem model is presented in Appendix A.

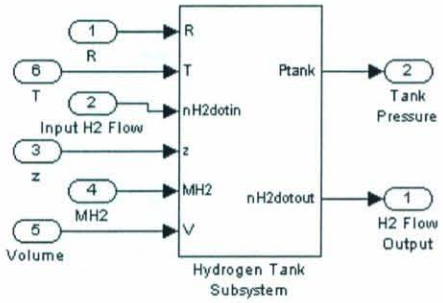

Figure 4.13: Simulink Model of Hydrogen Tank

4.3.2 Simulation Results of Hydrogen Tank

Like the electrolyzer, the hydrogen tank model has been simulated for 86400 seconds. At Ramea if the renewable resource generates additional energy after meeting the local load demand, the electrolyzer will be allowed to produce hydrogen which will be stored in the tank. However, when the electrical generation is less than the load demand, then the hydrogen generators will be operating driven by the stored hydrogen. Hence it is easily

imagined the tank has three phases – first phase when the electrolyzer is operating, second phase when both the electrolyzer and the hydrogen generators are non-operating and third phase when the hydrogen generators are operating.

Figure 4.14 reveals that from 10000 sec to 30000 sec the tank's hydrogen pressure is increased considering the initial pressure as 100 kPa. The second stage occurs between 30000 sec to 40000 sec while the hydrogen pressure remains constant and both the inlet and outlet valves are off. From 40000 sec to 50000 sec the hydrogen is discharged allowing the hydrogen generator to operate and producing energy to cover up the load demand.

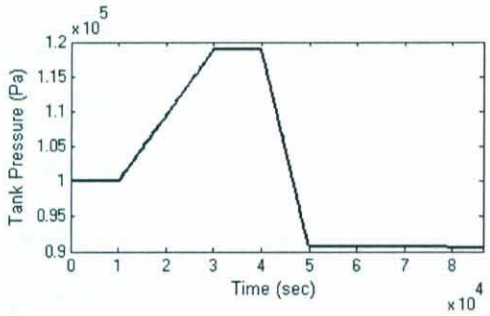

Figure 4.14: Hydrogen Tank Pressure at Different Phase

4.4 Modeling of Hydrogen Engines

Hydrogen engines are slightly modified versions of the conventional diesel engines manufactured by Hydrogen Engine Center Inc. [73]. No particulate level from this fuel represents a clear advantage over the diesel fuels. In addition to a reduction in compression ratio compared to diesel, charge dilution is done to avoid knock at one end and high thermal loads on the other. Furthermore, since these engines are produced as

conversion of diesel engines, high break mean effective pressure (bmep) levels are necessary. An accurate engine model is required for model-based controls since the inherent problem of delay in a throttle body hydrogen engine necessitates a more sophisticated control compared to a gasoline engine using port fuel injection. The engine characteristics have been unveiled by following two figures [73].

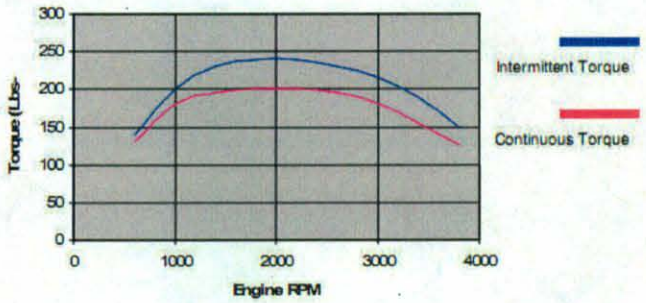

Figure 4.15: Engine Torque Characteristics

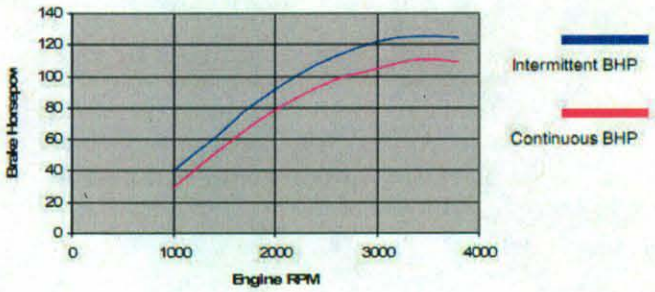

Figure 4.16: Engine Break Horse-power Characteristics

4.4.1 Dynamics of the Throttle Body

Four hydrogen engines coupled to same number of hydrogen generators are soon going to be added in Ramea power systems. The engine speed and the total rated power are 3600 rpm and 250 kW respectively. According to [74] there are three main parts of the engines-

throttle body, intake manifold and the torque production model. The model inputs are throttle opening area and the fuel flow rate. The Simulink model has been established depending on some empirical relationships.

The mixture of compressed hydrogen and air flows through the throttle body. This charge flow ($\dot{m}_i$) depends on the throttle opening area (A_{eq}) which is a function of throttle angle (α). It has been considered that the charge flow is one dimensional steady, compressible and isentropic in behavior. Equations 4.4.1 and 4.4.2 are the representation of the charge flow rate.

$$\dot{m}_i = c_d A_{eq}(\alpha) \frac{P_o \sqrt{k_{eq} M_{eq}}}{\sqrt{RT_o}} \left(\frac{2}{k_{eq}+1} \right)^{k_{eq}+1 / 2(k_{eq}-1)} \quad \text{(Choked)} \tag{4.4.1}$$

$$\dot{m}_i = c_d A_{eq}(\alpha) \frac{P_o \sqrt{M_{eq}}}{\sqrt{RT_o}} \left(\frac{P_m}{P_o} \right)^{1/k_{eq}} \left(\frac{2k_{eq}}{k_{eq}-1} \left[1 - \left(\frac{P_m}{Po} \right)^{k_{eq}-1/k_{eq}} \right] \right)^{1/2} \quad \text{(Un-choked)} \tag{4.4.2}$$

where c_d is discharge coefficient, P_o and P_m are throttle inlet pressure and intake manifold pressure respectively, R is the Universal gas constant, T_o is throttle inlet charge temperature, M_{eq} is equivalent molar weight of air-fuel mixture, k_{eq} is equivalent ratio of specific heats of air-fuel mixture. Here choked and un-choked system is decided by the comparing the ratio (P_m/P_o) with the critical ratio.

An inter-cooler has been considered between the fuel/air mixer and the throttle body. The throttle inlet charge temperature T_o is a function of the cooling process of the heat exchanger. If T_i and T_{amb} are inlet charge temperature to the inter-cooler and ambient

temperature respectively then the static relationship between the temperatures can be depicted below,

$$\frac{T_i - T_0}{T_i - T_{amb}} = 0.8 \tag{4.4.3}$$

4.4.2 Dynamics of the Manifold

In order to model the manifold dynamics, several assumptions have been considered. First, in the intake manifold the air and fuel are assumed as non-reacting and they get mixed completely. This would be a reasonable assumption as the molecular weights of air and hydrogen are comparable. It has also been considered that the amount of fuel and air leaving the intake manifold and entering the cylinders would have the same ratio as that of the mass of fuel and air in the intake manifold at any instant. In case of non-interacting mixtures, the Dalton's law of partial pressures has come up with,

$$\frac{\dot{m}_{fo}}{\dot{m}_{ao}} = \frac{m_f}{m_a} = \frac{P_f}{P_m - P_f}\frac{M_f}{M_a} \tag{4.4.4}$$

where $\dot{m}_{fo}$ and $\dot{m}_{ao}$ are the fuel and air flow rate into cylinders, m_f and m_a are the mass of fuel and air in the intake manifold, P_f and P_m are the partial pressure of fuel in the intake manifold and the intake manifold pressure, M_f and M_a are the molecular weight of fuel and air respectively.

Second, the temperature and pressure remain constant throughout the intake manifold. The intake manifold is modeled with the mass balance equations of air and fuel as mentioned below,

$$\dot{m}_{ao} = \dot{m}_{ai} - \frac{(\dot{P}_m - \dot{P}_f)M_a V}{RT_m} \tag{4.4.5}$$

$$\dot{m}_{fo} = \dot{m}_{fi} - \frac{\dot{P}_f M_f V}{RT_m} \tag{4.4.6}$$

where $\dot{m}_{ai}$ and $\dot{m}_{fi}$ are the air and fuel flow rate over throttle respectively, V is the manifold and port passage volume, T_m is the intake manifold temperature,

Since it is not practically possible to measure the P_a and P_f, it would be more convenient to deduce another differential equation regarding total intake manifold pressure from equations 4.4.4 to 4.4.6.

$$\dot{P}_f\left(\frac{P_m}{P_m - P_f}\frac{VM_f}{RT_m}\right) - \dot{P}_m\left(\frac{P_f}{P_m - P_f}\frac{VM_f}{RT_m}\right) = \dot{m}_{fi} - \dot{m}_{ai}\left(\frac{P_f}{P_m - P_f}\frac{M_f}{M_a}\right) \tag{4.4.7}$$

It is easily assumable that total charge mass entering the intake manifold is the summation of air and fuel entering; therefore the following relationship occurs,

$$\dot{m}_{ai} = \dot{m}_i - \dot{m}_{fi} \tag{4.4.8}$$

where $\dot{m}_i$ is the total charge flow over throttle.

From 4.4.7 and 4.4.8, the following equation can be found,

$$\dot{P}_f - \left(\frac{P_f}{P_m}\right)\dot{P}_m = \left(\frac{P_m - P_f}{P_m} + \frac{M_f P_f}{M_a P_m}\right)\frac{RT_m}{VM_f}\dot{m}_{fi} - \frac{RT_m}{VM_f}\frac{P_f}{P_m}\dot{m}_i \tag{4.4.9}$$

In equation 4.4.9, $\dot{P}_f$ should be eliminated in order to compute the state variable of intake manifold pressure P_m. Hence, another differential equation is needed which includes the same state variables. If $\dot{m}_o$ be the amount of charge mixture that is leaving the intake manifold and entering the cylinders, it can be illustrated by the volumetric efficiency (η_{vol}) and is given by the following speed density formula for a four stroke engine.

$$\dot{m}_o = \frac{n}{120} V_d \eta_{vol} \frac{P_m M_{eq}}{RT_m} \tag{4.4.10}$$

where V_d is the engine displacement and n is engine rotational speed.

Now adding equations 4.4.5 and 4.4.6 and using equation 4.4.10, the following relationship can be established,

$$\dot{P}_f \left(\frac{M_f - M_a}{M_a} \right) + \dot{P}_m = \left(\frac{RT_m}{VM_a} \right) \left[\dot{m}_i - \frac{n}{120} V_d \eta_{vol} \frac{P_m M_{eq}}{RT_m} \right] \tag{4.4.11}$$

By solving equations 4.4.9 and 4.4.11, P_m can be found explicitly as follows,

$$\dot{P}_m = \frac{RT_m}{VM_a} \left(\dot{m}_i - \dot{m}_{fi} \right) + \frac{RT_m}{VM_f} \dot{m}_{fi} - \frac{n}{120} \frac{V_d}{V} \eta_{vol} P_m \tag{4.4.12}$$

The fuel fraction in the manifold can defined as the ratio of fuel to the total charge mass in the intake manifold and expressed as follows,

$$f = \frac{m_f}{m_a + m_f} \tag{4.4.13}$$

The time derivative of the above equation becomes,

$$\dot{f} = \frac{\dot{m}_f}{m_a + m_f} - \frac{m_f(\dot{m}_a + \dot{m}_f)}{(m_a + m_f)^2} \tag{4.4.14}$$

The fuel fraction as a state variable can be related to the ratio of partial pressures in the intake manifold as follows,

$$\frac{P_m}{P_f} = 1 + \frac{M_f}{M_a}\left(\frac{1}{f} - 1\right) \tag{4.4.15}$$

The rate of change of fuel mass in terms of volumetric efficiency can be expressed as,

$$\dot{m}_f = \dot{m}_{fi} - f\dot{m}_o = \dot{m}_{fi} - f\frac{n}{120}V_d\eta_{vol}\frac{P_m M_{eq}}{RT_m} \tag{4.4.16}$$

Again the rate of change of total charge mass in the intake manifold is approximated by,

$$\dot{m} = \frac{VM_{eq}}{RT_m}\dot{P}_m \tag{4.4.17}$$

Substituting the above two relationships into equation 4.4.14,

$$\dot{f} = \frac{RT_m}{VM_{eq}P_m}\dot{m}_{fi} - \frac{n}{120}\frac{V_d}{V}\eta_{vol}f - \frac{f}{P_m}\dot{P}_m \tag{4.4.18}$$

This equation could be further simplified as follows,

$$\dot{f} = \frac{RT_m}{VM_a P_m}\dot{m}_{fi} - \frac{RT_m}{VM_a P_m}f\dot{m}_i \tag{4.4.19}$$

The fuel fraction dynamics is the most vital characteristic which distinguishes the hydrogen engine from the throttle body gasoline engine. The effect of fuel fraction on

thermal efficiency would have greater impact on the engine transient profile since it is directly related to the cylinder A/F ratio.

4.4.3 Rotational Dynamics

The mechanical power generation of the engine can be computed through the thermal efficiency. The differential equation governing the motion of the engine and the associated inertia rotating at same speed as the engine is revealed as follows,

$$\dot{n} = \frac{1}{Jn}\left(H_L \eta_i \{f\dot{m}_o\}\Big|_{(t-\tau_d)} - \left(P_{tf} + P_{pc} + P_b + P_{ext}\right)\right) \qquad (4.4.20)$$

where J is the effective inertia, H_L is the lower heating value of the hydrogen gas, η_i is the thermal efficiency, $\dot{m}_o$ is the charge flow rate from the manifold to cylinders, τ_d is the delay between fuel intake and torque generation, P_{tf} is the total frictional power, P_{pc} is the pumping power correction, P_b is the peripheral load power and P_{ext} is the external load power.

Combining the throttle body, manifold and rotational dynamics together, the engine model developed in Simulink is displayed in Figure 4.17 and the elaborated subsystem model is included in Appendix A.

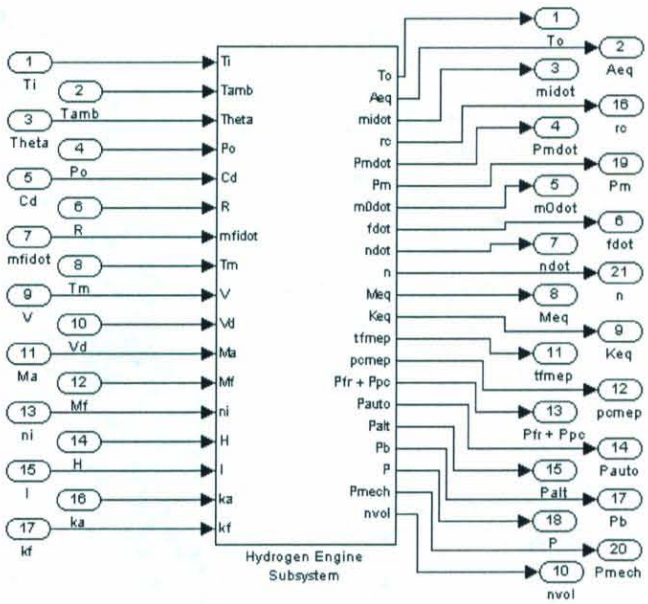

Figure 4.17: Simulink Model of Hydrogen Engine

4.4.4 Simulation Results

Hydrogen is the simplest of atoms, consisting of one proton and one electron also called a protium. As atoms, hydrogen is very reactive and prefers to join into molecular pairs (H_2) and when mixed in sufficient quantities with an oxidant (for example air, O_2, Cl, F, N_2O_4 etc.) becomes a combustible mixture. Like all other fuels, H_2 requires proper understanding and handling to avoid unwanted flammable or explosive environments. Hydrogen is not a primary source of energy; rather it is an energy carrier much like the electricity. Therefore, energy is required to extract hydrogen from substances like natural gas, water, coal or any other hydrocarbons. Table 4.2 represents some of the combustion properties of H_2 at 20 °C and 1 atm [61, 75].

Combustion Properties	Values
Flamability Limits in Air	4-75 %vol
Flamability Limits in Oxygen	4-95 %vol
Detonability Limits in Air	18-59 %vol
Detonability Limits in Oxygen	15-90 %vol
Minimum Ignition Energy in Air	17 μJ
Auto Ignition Temperature	858 K
Quenching Gap in Air	0.064 cm
Diffusion Coefficient in Air	0.061 cm2/sec
Flame Velocity	2.7-3.5 m/s
Flame Emissivity	0.1
Flame Temperature	2318 K

Table 4.2: Selected Combustion Properties of H_2 at 20 °C and 1 atm

As mentioned earlier, the hydrogen flow rate and the mechanical power are the transient input and output parameters of the engine respectively. According to [73] the rated mechanical output power of the engine is 75 kW while drawing the hydrogen at the rate of 1.472 mol/s. However, the rated engine speed is 3600 rpm while coupled to the hydrogen generator in synchronous operation. Table 4.3 shows some of the input parameters associated to the hydrogen engine simulation and Figure 4.18 to 4.20 reveal the simulation results.

Input Parameters	Values
Ti	300 K
Tamb	283 K
Tm	310.78 K
A	15 Degree
Cd	1
V	5.55e-3 m3
Vd	8.3e-3 m3
Ma	28.9644 gm/mol
Mf	2.016 gm/mol
ηi	0.4
H_L	120.1 MJ/kg
J	8000 kg-m2
Ka	1.4
Kf	1.405

Table 4.3: Input Parameters of the Hydrogen Engine

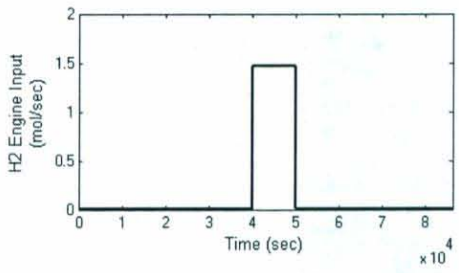

Figure 4.18: Hydrogen Flow Rate Input to the Engine

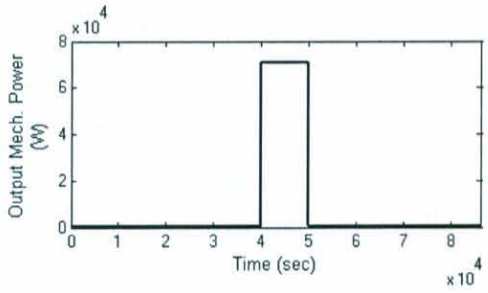

Figure 4.19: Mechanical Output Power from the Engine

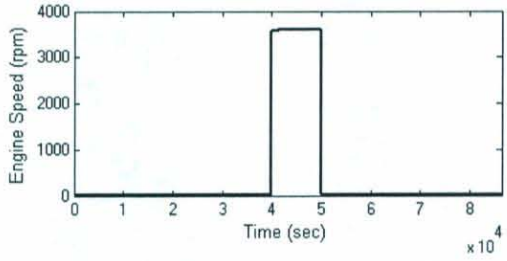

Figure 4.20: Synchronous Speed of the Engine

The simulation results demonstrate that the hydrogen engine operate from 40000 sec to 50000 sec during the day consuming hydrogen at the rate of maximum 1.472 mol/s and producing 75 kW of rated mechanical power. During this interval the engine maintains 3600 rpm synchronous speed.

4.5 Modeling of Electrical Generator coupled to Hydrogen engine

Among the electric machines that run at synchronous speed, the largest and probably the most common are the three-phase synchronous machines. Although the construction of the three-phase synchronous machines is comparatively expensive than that of induction

machines, their efficiency is an advantage at a higher power rating. Three-phase synchronous machines are widely used for power generation and large motor drives.

The stator of a synchronous machine consists of a stack of laminated ferromagnetic core with internal slots, a set of three-phase distributed stator windings placed in the core slots and an outer frame-work with end shields and bearings for the rotor shaft. The turns of the stator windings are equally distributed over pole-pairs and the phase axes are spaced $2\pi/3$ electrical radians apart [76].

4.5.1 Simulink Model of Generator

In order to model the synchronous generator in Simulink environment and to measure the active power from it, an excitation system, a per unit fundamental synchronous machine block, a three-phase V-I measurement block, a three-phase instantaneous active and reactive power block and a load are coupled together. This arrangement is revealed in Figure 4.21.

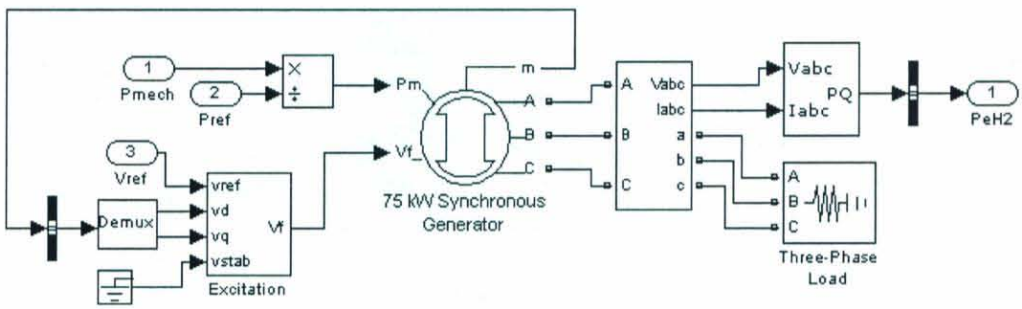

Figure 4.21: Simulink Model of Hydrogen Generator

The excitation system is required to generate a field voltage (V_f) which is further applied to the machine block. A number of parameters are responsible to control this voltage and indirectly govern the output power of the machine. The parameter values corresponding to the excitation system are depicted in Table 4.4.

Combustion Properties	Values
Low Pass Filter Time Constant	20 ms
Regulator Gain	200
Regulator Time Constant	20 ms
Exciter Gain	1
Damping Filter Gain	0.001
Damping Filter Time Constant	100 ms
Regulator Output Limits	0-6 pu

Table 4.4: Excitation System Parameters

Like the asynchronous machines described in Chapter 3, the synchronous machines operate in either generator or motor mode depending on the sign of the mechanical power applied. For the negative mechanical power, this machine will run as a generator. The electrical part of the machine is represented by a sixth-order state-space model. This generator model takes the dynamics of stator, field and damper windings into account. Moreover, all the rotor parameters and electrical quantities are viewed from the stator and the equivalent circuit of the model is expressed in rotor reference frame (d-q frame). The equivalent electrical part of this machine in d-q reference frame is depicted in Figure 4.22 [57].

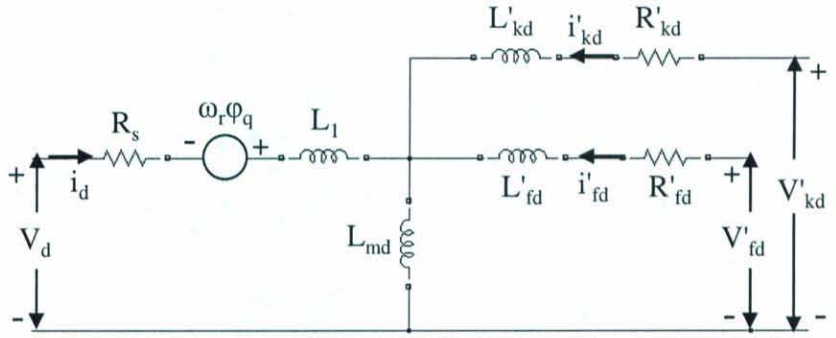

d axis equivalent circuit

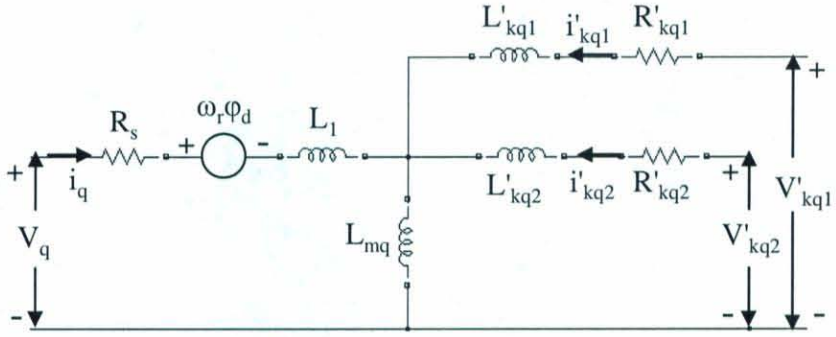

q axis equivalent circuit

Figure 4.22: Hydrogen Generator Equivalent Circuit

The emf expressions result from the d-q frame equivalent circuits can be shown below,

$$V_d = R_s i_d + \frac{d}{dt}\varphi_d - \omega_r \varphi_q \tag{4.5.1}$$

$$V_q = R_s i_q + \frac{d}{dt}\varphi_q + \omega_r \varphi_d \tag{4.5.2}$$

$$V'_{fd} = R'_{fd} i'_{fd} + \frac{d}{dt}\varphi'_{fd} \tag{4.5.3}$$

$$V'_{kd} = R'_{kd} i'_{kd} + \frac{d}{dt}\varphi'_{kd} \tag{4.5.4}$$

$$V'_{kq1} = R'_{kq1} i'_{kq1} + \frac{d}{dt}\varphi'_{kq1} \tag{4.5.5}$$

$$V'_{kq2} = R'_{kq2} i'_{kq2} + \frac{d}{dt}\varphi'_{kq2} \tag{4.5.6}$$

where V_d and V_q are d and q axis voltages, R_s is the stator resistance, i_d and i_q are d and q axis currents, φ_d and φ_q are d and q axis fluxes, ω_r is the rotor rotational speed, V'_{fd}, R'_{fd}, i'_{fd} and φ'_{fd} are d axis field winding voltage, resistance, current and flux respectively. In the same way V'_{kd}, R'_{kd}, i'_{kd} and φ'_{kd} are d axis damper winding voltage, resistance, current and flux respectively. In q axis there is no field quantity, rather two damper quantities exist. Therefore, V'_{kq}, R'_{kq}, i'_{kq} and φ'_{kq} are q axis damper winding voltage, resistance, current and flux. Subscript 1 and 2 represent the first and second damper windings.

All the flux components depending on the d-q axes inductances and currents and are expressed as follows,

$$\varphi_d = L_d i_d + L_{md}\left(i'_{fd} + i'_{kd}\right) \tag{4.5.7}$$

$$\varphi_q = L_q i_q + L_{mq} i'_{kq} \tag{4.5.8}$$

$$\varphi'_{fd} = L'_{fd} i'_{fd} + L_{md}\left(i_d + i'_{kd}\right) \tag{4.5.9}$$

$$\varphi'_{kd} = L'_{kd} i'_{kd} + L_{md}\left(i_d + i'_{fd}\right) \tag{4.5.10}$$

$$\varphi'_{kq1} = L'_{kq1} i'_{kq1} + L_{mq} i_q \tag{4.5.11}$$

$$\varphi'_{kq2} = L'_{kq2} i'_{kq2} + L_{mq} i_q \tag{4.5.12}$$

The synchronous machine block computes the mechanical characteristics described by the following equations,

$$\Delta\omega(t) = \frac{1}{2H}\int_0^t (Tm - Te)dt - Kd\Delta\omega(t) \tag{4.5.13}$$

$$\omega(t) = \Delta\omega(t) + \omega_0 \tag{4.5.14}$$

where $\Delta\omega$ is the speed variation with respect to the speed of operation, H is the inertia constant, Tm and Te are the mechanical and electromagnetic torque respectively, Kd is the damping factor, $\omega(t)$ is the mechanical speed of rotor and ω_0 is the speed of operation.

When the machine is connected to an infinite network, the disparity of the machine power angle (δ) resulting from a change of mechanical power (Pm) can be approximated by the following second order transfer function,

$$\frac{\delta}{Pm} = \frac{(\omega_s / 2H)}{(s^2 + 2\zeta\omega_n s + \omega_n^2)} \tag{4.5.15}$$

$$\omega_n = \sqrt{\omega_s P_{\max} / (2H)} \tag{4.5.16}$$

$$\zeta = (Kd/4)\sqrt{2/(\omega_s \cdot H \cdot P_{\max})} \tag{4.5.17}$$

$$P_{\max} = \frac{V_t \cdot E}{X} \tag{4.5.18}$$

where δ is the power angle (angle between the terminal voltage, V_t and the internal voltage, E), Pm is the mechanical power, ω_n is the frequency of electromechanical oscillations, ζ is the damping ratio, ω_s is the electrical frequency and P_{max} is the maximum power transmitted through the reactance X.

The three-phase V-I measurement block is used to determine the three-phase voltages and currents in a circuit. While connected in series with a three-phase element, it

computes the three phase-to-phase or phase-to-ground voltages and the three line currents in SI unit or pu values. This measuring block has been developed depending on the following two equations,

$$V_{abc}(pu) = \frac{V_{abc}(volts)}{\left(\frac{V_{baseLL}}{\sqrt{3}} \cdot \sqrt{2}\right)} \tag{4.5.19}$$

$$I_{abc}(pu) = \frac{I_{abc}(amperes)}{\left(\frac{P_{base}}{V_{baseLL}\sqrt{3}} \cdot \sqrt{2}\right)} \tag{4.5.20}$$

where V_{baseLL} is the base line-to-line voltage in volts rms P_{base} is the three-phase base power in volts-amperes.

The three-phase instantaneous active and reactive power block determines the real and reactive powers according to the following expressions,

$$P = V_a I_a + V_b I_b + V_c I_c \tag{4.5.21}$$

$$Q = \left(1/\sqrt{3}\right)\left(V_{bc} I_a + V_{ca} I_b + V_{ab} I_c\right) \tag{4.5.22}$$

4.5.2 Hydrogen Generator Simulation Results

Similar to the electrolyzer, hydrogen tank and hydrogen engine, the hydrogen generator is simulated for 24 hours span where it is allowed to run from 40000 sec to 50000 sec. When the hydrogen is consumed at the rate of 1.472 mol/s and the engine mechanical power output is 70.7 kW, the synchronous machine will generate 68.5 kW electrical power. Figure 4.23 shows the simulation result of hydrogen gensets.

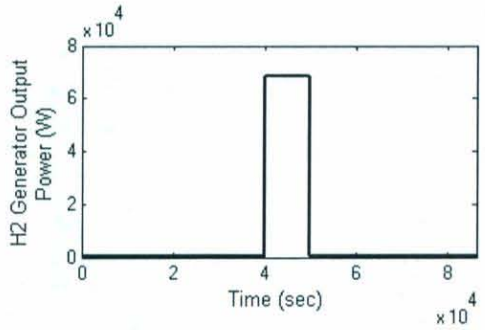

Figure 4.23: Hydrogen Generator Output Power

The hydrogen gensets will produce energy according to the load demand and the generation by other sources. Therefore the amount of stored hydrogen consumed by the engines varies with the generator output. In order to find the consequence between hydrogen flow rate to engine, engine mechanical power and the generator electrical power, several simulations have been conducted and their results are highlighted in the Table 4.5 as follows,

Tank Output Flow Rate (mol/s)	Mechanical Power from Hydrogen Engine (kW)	Electrical Power Hydrogen Generator (kW)
1.472	70.70	68.5
1.300	62.50	60.5
1.150	55.25	53.5
1.000	48.00	46.5
0.850	40.83	39.6
0.700	33.63	32.6
0.550	26.42	25.6

Table 4.5: Relationship between H_2 Consumption, Engine Mechanical Power and Generator Electrical Power

The parameters assigned for the hydrogen gensets for running the simulations are tabulated below,

Parameters	Values	Parameters	Values
Rs	0.5461 pu	Lkd	0.7733 pu
Ll	0.08 pu	Rkq1	0.04402 pu
Lmd	2.56 pu	Lkq1	0.04147 pu
Lmq	1.13 pu	H	0.1225 s
Rf	0.01909 pu	F	0.02352 pu
Lfd	0.2456 pu	p	1
Rkd	0.2708 pu		

Table 4.6: Assigned Parameters for Hydrogen Generators

4.6 Summary

The objective of utilizing the hydrogen system at Ramea is to ensure the energy storage in long term basis. It eliminates the necessity of any short term energy storage like conventional battery. Hydrogen is stored when adequate amount of wind is available and captured through the wind turbines and consumed through the engines when the load remains high and wind resource is not that much plentiful. The hydrogen storage system is advantageous in couple of ways as explicated earlier. The Simulink models for electrolyzer, hydrogen tank, engine and generator have been presented in this chapter along with their simulation results. The dynamic simulations of the combined system will be covered in the chapter that follows.

Chapter 5

Transient Analysis of Ramea Hybrid Power System

5.1 Energy Generation for Stand-Alone Applications

Until the advent grid connected networks, all power systems were decentralized, energy have been being produced at the locations where it was required. In the case of wind power, milling, pumping and irrigation were the trendy applications. Electricity has accomplished the development of the grid networks with centralized generating capacity resulted the demise of many isolated power systems. Even then, due to remoteness and cost, it is unlikely that a main grid connection will ever be established in such communities, although they are in need of energy.

Precisely mentioning, there are three types of application [77] for remote electrical power,

- Power for specialized applications in isolated areas, e.g., communication, irrigation, control etc.

- Community power generation in developing countries and
- Power for remote communities in industrialized countries and on islands.

Each of them has its own particular necessities and design constraints. For instance, system reliability might be more expected than cost of energy in unmanned locations, whilst for communities in developing countries simplicity of maintenance is a prime consideration whereas communities in industrialized countries quickly developed high expectations of power quality and availability as well as competitiveness. As an island, Ramea belongs to the latest mentioned category of power application.

5.2 Potential of Wind-Diesel-Hydrogen Systems

The obvious way out to the problem of using wind power capacity at a remote territory would be to compensate for the unpredictability of the wind by using a diesel electric generator to make up any shortfall. Such a system would have the advantage of using the free wind resource, of saving on existing levels of fuel consumption and of providing power on demand meeting the consumer load. Ideally the diesel could be used to provide firm power during periods of deficient wind and the wind turbine could be used to save diesel fuel when wind energy is abundant. Such basic Wind-Diesel systems supply firm power while fuel is being saved. However, as will be shown next couple of sections some combination of long term hydrogen storage and dump load will often improve power quality and fuel savings.

5.3 Ramea Hybrid Power System

Individual modeling and the characteristic of each constituent of Ramea power system have been explicated in Chapter 3 and Chapter 4. This chapter will highlight the combined behaviors of the system with Simulink-SimPower model. Figure 5.1 reveals the complete power system including the generation, storage and load systems.

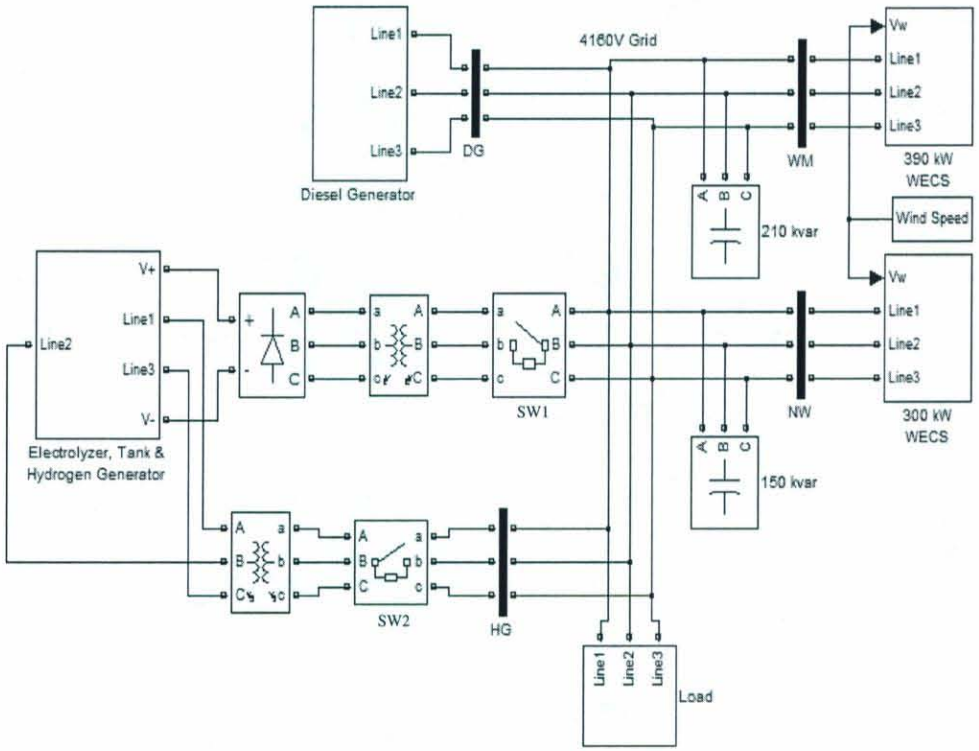

Figure 5.1: Ramea Wind-Diesel-Hydrogen Hybrid Power System

From the above figure, three 100 kW and six 65 kW wind turbines, belonging to the wind energy conversion system, including the 925 kW diesel generators form the generation system of the Ramea community. The generator in the hydrogen system falls in the generation system too. The storage system comprises of the remaining parts of the

hydrogen system. The load system is the conjunction of the community load and the dump load which is often used for ensuring the system stability. The preceding chapters cover descriptions of all components except the diesel generation and the dump load system. Therefore, this stage of literature necessitates the illustration of those subsystems.

5.4 Modeling of Diesel Generator

The working principle of diesel generator is similar to the hydrogen gensets discussed in section 4.5.1 except the governor and engine system. Desired and actual speeds are the two inputs to the engine block and the mechanical power is the output from the block which will further be coupled to the synchronous generator. The engine's characteristics are based on two transfer functions as follows [57],

Controller transfer function, $$H_c = \frac{(1+T_3 \cdot s)K}{(1+T_1 \cdot s+T_1 \cdot T_2 \cdot s^2)} \quad (5.4.1)$$

Actuator transfer function, $$H_a = \frac{(1+T_4 \cdot s)}{[s \cdot (1+T_5 \cdot s) \cdot (1+T_6 \cdot s)]} \quad (5.4.2)$$

where K is the regulator gain, T_1, T_2 and T_3 are the regulator time constants and T_4, T_5 and T_6 are the actuator time constants. Here the excitation system is functioning nothing different from that of hydrogen generator system. The diesel engine and excitation system parameters are specified in Table 5.1 and 5.2. However, their SimPower subsystem model is depicted in Figure 5.2. The subsystem model of the diesel engine will be expounded in Appendix A.

Engine Parameters	Values
Regulator Gain, K	30
Regulator Time Constants (T1, T2, T3)	0.01, 0.02, 0.2
Actuator Time Constants (T4, T5, T6)	0.25, 0.009, 0.0384
Torque Limit	0 - 1.1
Engine Time Delay, Td	2.4 ms

Table 5.1: Diesel Engine System Parameters

Excitation Parameters	Values
Low Pass Filter Time Constant	10 ms
Regulator Gain	200
Regulator Time Constant	20 ms
Exciter Gain	1
Damping Filter Gain	0.1
Damping Filter Time Constant	1.5 s
Regulator Output Limits	0-6 pu

Table 5.2: Diesel Excitation System Parameters

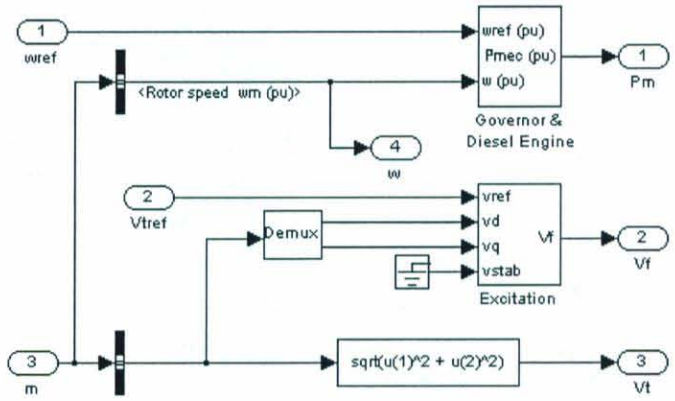

Figure 5.2: Engine and Excitation System of Diesel Generator

The rated power of diesel generator is 925 kW. Mechanical power and field voltage are the inputs to this generator block and electrical energy according to the demand produced from this block. The SimPower model of the diesel generator

associated with the excitation and the engine systems is shown in Figure 5.3 and the generator specifications are presented in Table 5.3.

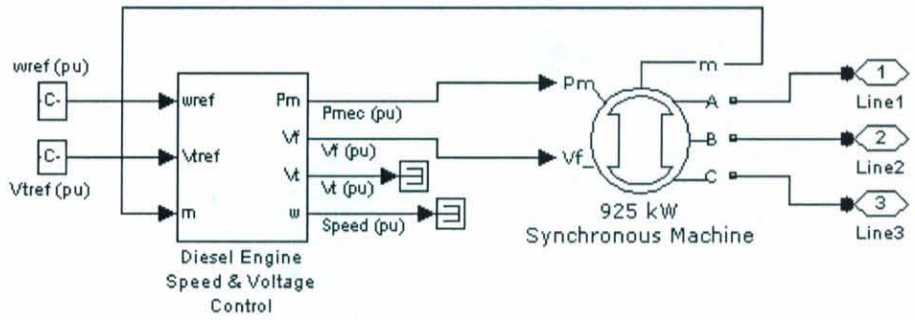

Figure 5.3: SimPower Model of Diesel Generator

Parameters	Values	Parameters	Values
Rs	0.0010615 pu	Lkd	4.5675 pu
L1	0.06 pu	Rkq1	0.4939 pu
Lmd	2.86 pu	Lkq1	6.548 pu
Lmq	1.98 pu	H	0.6469 s
Rf	0.005759 pu	F	0.005327 pu
Lfd	0.0355 pu	p	2
Rkd	2.4 pu		

Table 5.3: Diesel Generator System Parameters

5.5 Modeling of Dump Load

The eight-step variable load (dump/secondary load) block implements a three-phase resistive load. This load variation uses an eight bit binary sequence so that the load power can be varied by steps from assigned initial value to the maximum 446.25 kW. There are

eight three-phase equal valued resistors connected in series with ideal switches simulating forced-commutated power electronic switches. The pulse input is a vector containing the eight binary bits controlling the eight switches resulting in step change of the load. The SimPower model of the dump load is expressed in Figure 5.4. Appendix A will include the switch and resistive load subsystems.

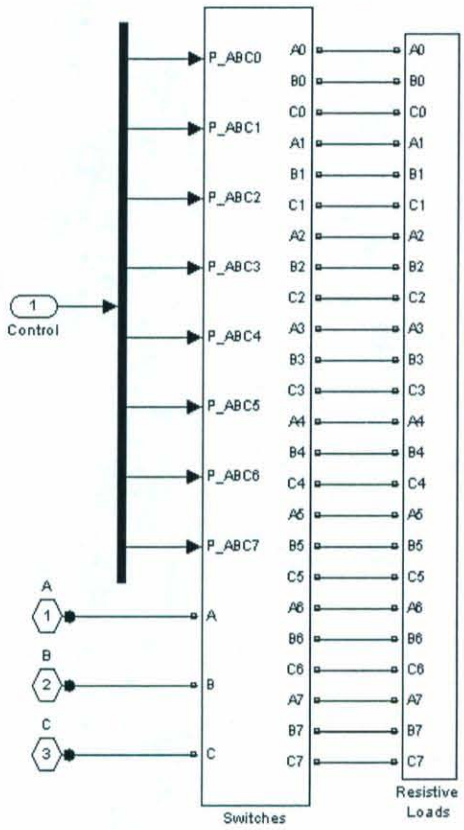

Figure 5.4: SimPower Model of the Dump Load

Apart from the diesel power generation, the power system might become unstable due to variable wind speed and/or variable load demand. Sometimes it is very hard to

harmonize the overall power generation and consumption. The dump load, in the simulation, has been incorporated to mitigate this problem.

5.6 Simulation of the Hybrid System

The whole power system simulation has been analyzed with five different case studies. The simulation is allowed to run for 30 seconds and variable step stiff/Mod. Rosenbrock solver [57] has been chosen. However, the non-adaptive algorithm for zero crossing has also been considered during simulation execution. The following subsections will highlight the case studies with corresponding results in details.

5.6.1 Case Study I: Simulation with Variable Load

The behaviors of all generating systems have been observed while changing the community load. The first 10 seconds have been accorded for acquiring the results. At 3rd second the load has shifted up from 1200 kW to 1600 kW and at 6th second it has returned to the initial value. Figure 5.5 reveals the simulation results regarding power ups and downs. Both the WM15S and NW100 wind turbines generate the maximum power at their rated wind speed and ensure the constant power generation ignoring small spikes regardless of the load fluctuations. The diesel generator and the secondary load respond to the main load variation as expected. At 6 second, as the main load is reduced by 400 kW, the secondary load is increased up to 400 kW to make the system stable. During 6 second to 10 second the secondary load current has been recorded as 0.8 pu. As the secondary

load voltage does not change, the current will rise with increment of the secondary load and vice versa.

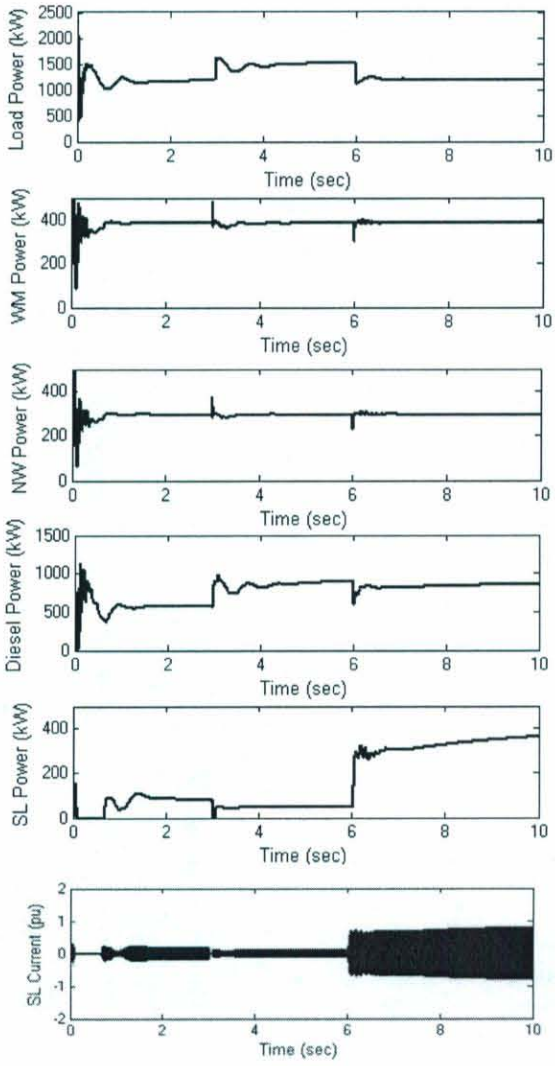

Figure 5.5: Simulation Results with 1200/1600/1200 kW Load Variation

5.6.2 Case Study II: Simulation with Variable Wind Speed

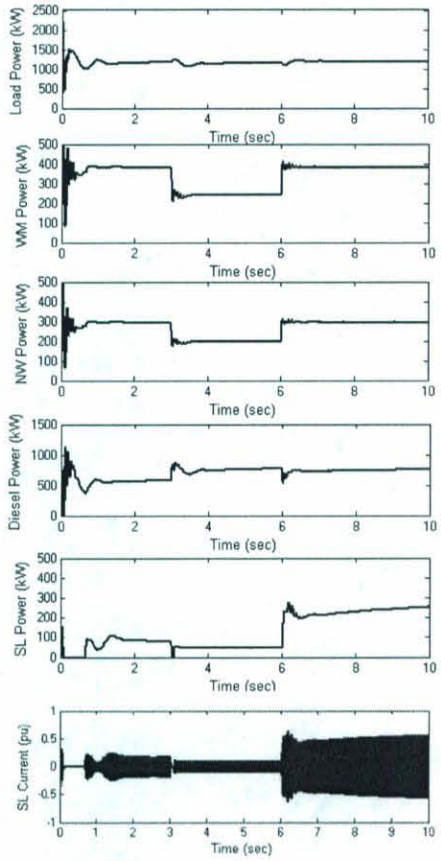

Figure 5.6: Simulation Results with Wind Speed Variation with 15/10/15 m/s and 1200 kW Fixed Load

In this case the main load remains constant and the wind speed is allowed to vary. At 3rd second the wind speed slumps from 15 m/s to 10 m/s and elevated to 15 m/s again at 6th second. From Figure 5.6 it can be noticed that the load power is almost constant and both types of wind turbines retort according to the wind speed change. As the wind generations drop during 3 second to 6 second, the additional load is met up by the diesel energy as shown the results. Moreover, the secondary load has been found dilating up to 250 kW maintaining the current around 0.55 pu during 6 second to 10 second restricting

the diesel energy to droop, rather retaining the same value. This condition has been occurred because after 6th second the wind generation increases but the load remains fixed and to keep the system stable, the secondary load has to be bigger.

Another scenario has been introduced with 500 kW constant load and wind speed rises from 7 m/s to 8 m/s. Both the electrolyzer and the hydrogen generators are considered to be idle. The wind speed increment is occurred in 5th second. The simulation results are depicted in Figure 5.7 where the diesel and secondary load powers automatically adjust the transient effects.

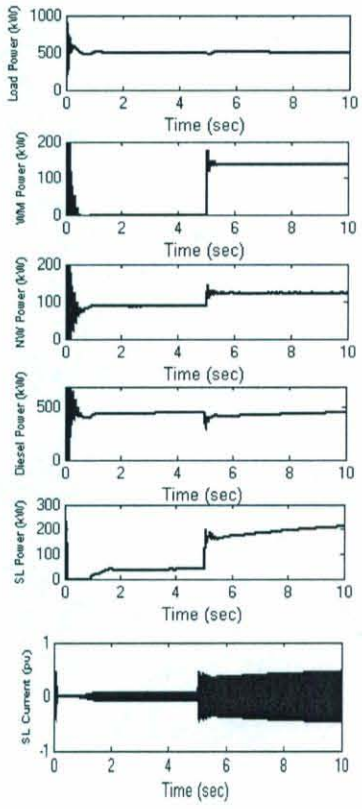

Figure 5.7: Simulation Results with 500 kW Load and Wind Speed Varies from 7-8 m/s

The above figure reveals that the wind generations distend significantly with the rise of wind speed. For 7 m/s wind speed although the Windmatic power looks to be zero but exactly it is around 15 kW. This happened because during that period the smaller generator of each WECS runs (referring to Section 3.5). After the 5th second the WM power comes from the larger generator and leaps to around 144 kW. The diesel generation remains almost constant while the dump load consumes the additional energy to maintain the system stable. After the 5th second the secondary load current reaches around 0.5 pu.

In order to observe the functions of all components of Ramea power system, a different transient circumstance has been considered. In this instance wind speed is allowed to vary from 12 m/s to 13 m/s and the community load is steady at 300 kW. Like the previous example the hydrogen system is again considered to be non-operating. The components' behaviors are more prominent in Figure 5.8.

Figure 5.8 unveils that the load is fixed at 300 kW and the wind turbines respond appropriately to the change of wind speed at 5th second. It is important to realize that the high wind speed and the small load demand keep the diesel generation significantly low and conversely turn the dump load consuming maximum amount of energy. As the wind generations are elevated at 5th second, the diesel generation expectedly declines to certain scale as the secondary load is in its rated capacity from the very beginning. For this reason the SL current reaches to 1 pu. just after the initial transients. As the load is very low compared to the wind generations, the secondary power is found to be fluctuating from the very beginning. This could be eliminated by introducing a larger dump load.

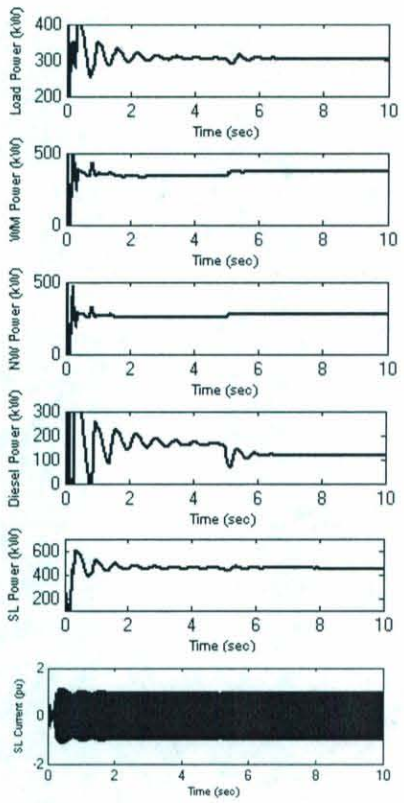

Figure 5.8: Simulation Results with 300 kW Load and Wind Speed Varies from 12-13 m/s

5.6.3 Case Study III: Simulation with Electrolyzer in Operation

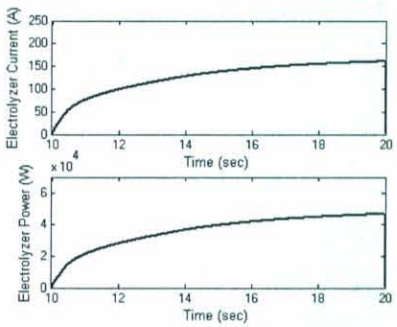

Figure 5.9: Electrolyzer Power and Current

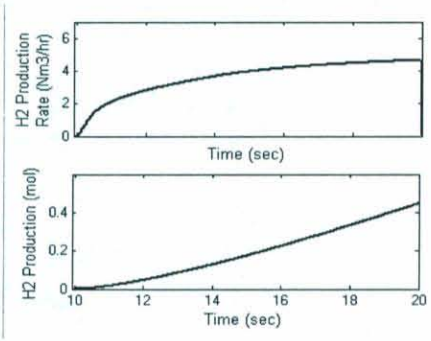

Figure 5.10: Electrolyzer H_2 Production

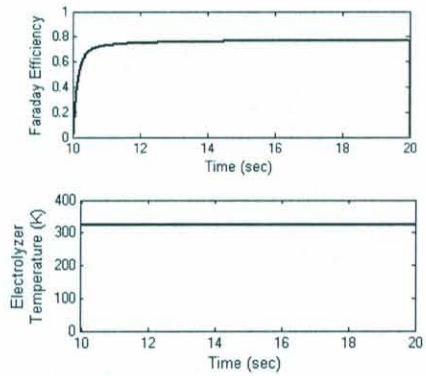

Figure 5.11: Electrolyzer Faraday Efficiency and Temperature

The electrolyzer is allowed to operate during 10 second to 20 second. The other associated considerations are the wind turbines run at rated speed, the load remains almost constant and the diesel generator operates at its rated capacity. Figure 5.9 to 5.12 uncover that while the electrolyzer is operating it consumes about 45 kW power (in Figure 5.9) in conjunction with 1200 kW of main load and 400 kW of secondary load (in Figure 5.12). However the NW100 and WM15S wind turbines generate 300 kW and 390 kW rated powers respectively and the diesel generation is maximum 925 kW have been found in Figure 5.12. A DC current of 160A (in Figure 5.9) passing through the electrolyzer stacks govern the electrolysis and producing hydrogen at the rate of 4.6 Nm^3/hr (in Figure 5.10). The Faraday efficiency and the temperature of this electrolyzer have been found to be 78% and 325 K sequentially (in Figure 5.11). These simulation results are not exactly same but close to those found in section 4.2.4. The reason is, unlike the input current applied to the electrolyzer in Chapter 4, here the input current is not a square wave rather it changes exponentially.

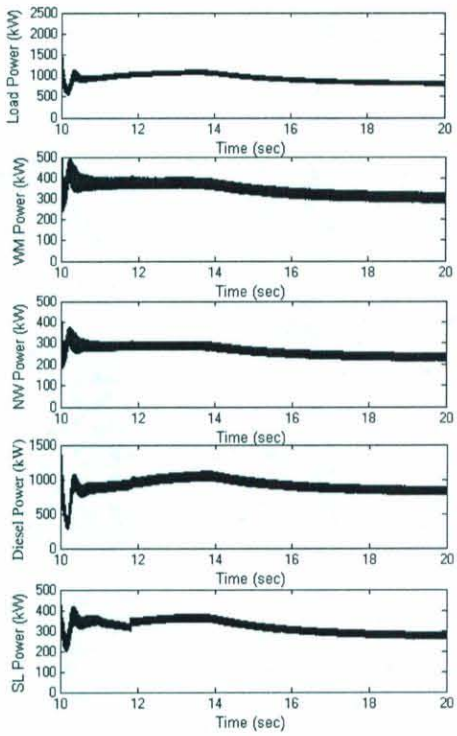

Figure 5.12: Simulation Results with Electrolyzer Operation

5.6.4 Case Study IV: Simulation with hydrogen Generators in Operation

In this stage the hydrogen generators serve as the generating system along with the diesel generators. This occurs during 25 second to 27 second simulation interval. Before that i.e., from 20 second to 25 second it has been considered that both the electrolyzer and the hydrogen generators remain non-operating condition keeping the tank pressure constant. The wind speed is also assumed below cut-in speed and hence the wind generation is insignificant. The main load and the secondary load have been reported as 200 kW and 60 kW respectively unveiled in Figure 5.13 and 5.14 while both the diesel and the hydrogen

generators produce 130 kW each. The mechanical power from the hydrogen engine is found as 140 kW and therefore machine loss is approximately 10 kW. The three-phase secondary load current is obtained as 0.5 pu and the engine speed as 3600 rpm as desired.

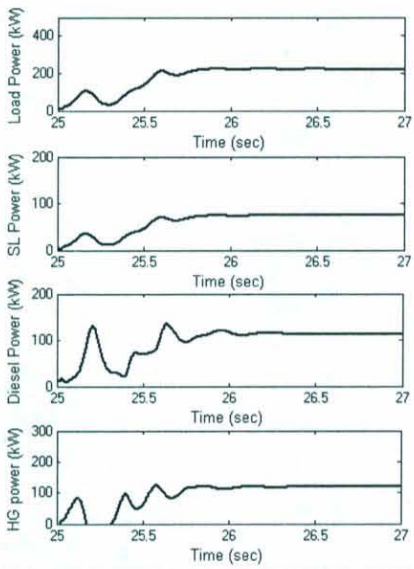

Figure 5.13: Simulation Results with Hydrogen Gensets in Operation

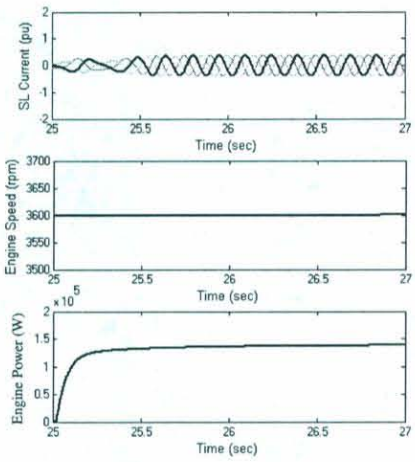

Figure 5.14: Secondary Load Current, Engine Speed and Mechanical Power

5.6.5 Case Study V: Simulation with only Diesel Generator in Operation

This condition might occur when there is no wind and all stored hydrogen is used up. In this case diesel is the only means to produce energy. Figure 5.15 illustrates the transients of diesel power and secondary load power with variable load. It can be observed that the load is initially 500 kW, at 3rd second it goes up to 700 kW and drops to 500 kW again at 6th second. The diesel generator is precisely following the load except from the 2nd step change. The sharp rise of the dump load binds the diesel generator to stepping down to initial level. From this instant the secondary load remains around 180 kW and a trifling declination of the diesel energy is found. The reason behind the change of dump load is to mitigate the effects of sudden slump of community load on the whole system.

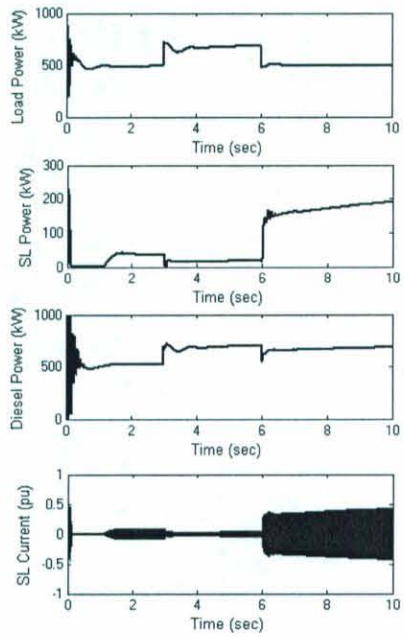

Figure 5.15: Simulation Results with only Diesel Generator is Operating

5.7 Summary

The Ramea Wind-Diesel-Hydrogen hybrid power system has been simulated with five different stages. Unlike the simulations of Chapter 3 and 4 where they have been carried out for 86400 seconds, this chapter's simulations are conducted for only 30 seconds. The reason is the size of the model, i.e. the complete Ramea power system is so complex that it is just about impossible to run for that long period. As the Ramea power system practically includes the dump load, a SimPower model of the dump load has been incorporated to the main system. Furthermore, properly controlled dump load model ensures the system stability as well. As the preceding case studies have not discussed the hydrogen tank dynamics, certain characteristics of the tank have been revealed in Figure 5.16 and 5.17 as follows.

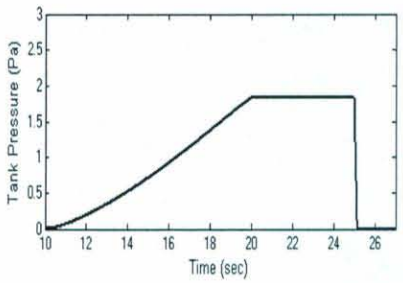

Figure 5.16: H_2 Tank Pressure

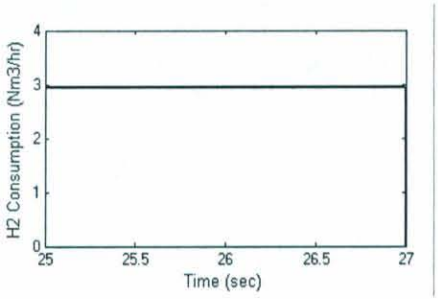

Figure 5.17: H_2 Consumption rate by the H_2 Engine

Figure 5.16 illustrates that from 10 second to 20 second while the electrolyzer is operating and hydrogen is produced, the tank pressure distends. It remains unchanged from 20 second to 25 second as both the electrolyzer and the hydrogen generators are out

of operation. With the hydrogen generator operation, tank pressure diminishes abruptly after 25 second. During this interval the hydrogen engines require 3 Nm^3 of hydrogen per hour as displayed in Figure 5.17. Summarizing all simulation results it can easily clinched that the complete Simulink-SimPower model of Ramea power system runs successfully and performs as apprehended.

Chapter 6

Conclusions and Recommendations

6.1 Summery of This Research

There are more than 300 isolated communities around Yukon, Nunavut and coastal islands where approximately 0.2 million people are living [78]. The electric distribution grids have not reached to those places to connect the technical installations, tourist facilities, farms and plants. This is the result of economic pronouncements related to the cost of transmission and distribution lines over the vast terrains. These detached territories are usually powered by diesel fuel. Large electric power plants such as gas, hydro, nuclear, wind etc. are even cheaper than that of diesel power plants. However, the significantly higher fuel transport cost should be added to the operating cost. Not only that, they are responsible for million of tons of harmful gas emissions. The positive thing is, as most of the remote communities are located near the coastal regions, they are blessed by the wind resources.

Ramea, like others, is a small island where the exploitation of the wind resource could depreciate the negative impacts of using fossil fuels. This research is about wind-diesel-hydrogen based power system modeling, simulation and analysis. The Ramea power system employed three 925 kW diesel generators, among them one is always operating and other two are kept in standby. Six WM15S wind turbines of 65 kW each and three NW100 wind turbines of 100 kW each are now brought into operation in order to utilize the wind resource. Another energy generation component is the hydrogen generator plant of 250 kW rated capacity which is composed of five hydrogen gensets, four are operating and the fifth one is on standby.

However, for the increment of power system efficiency and reduced switching, some storage system is required. Several research works are being carried out to determine the feasibility of different means of storage. Although battery is the most popular storage device so far, it has been proved to be inconceivable in terms of long term energy storage. Pumped hydro, flywheel and hydrogen are some of the suitable provisions for the energy storage. This research is on the hydrogen storage technique by employing a 200 kW electrolyzer and three hydrogen tanks of 1000 Nm^3 combined capacity coupled to the hydrogen engines. The early chapters explicate the steady state models of individual constituents of this system and finally they are coupled together and simulated to examine their characteristics and dynamic behavior. The next section will briefly adduce the contribution of this research.

6.2 Research Contribution

- The Ramea power system has been presented along with the projections of wind resource in that region. Some papers related to permanent magnet synchronous generator based wind turbines, squirrel cage induction generator based wind turbines and economy, cost analysis, operation and performance of hybrid energy systems have been highlighted. Moreover, the subject matters of these papers assisted this research as well.
- HOMER has been used for sizing, economic and electrical aspects analysis of the Ramea hybrid energy system. Besides designating the different parts and on hand resources, some of the probabilistic scenarios have been depicted by surface plots (Figure 2.12 to 2.16). The proposed configuration assures negligible amount of unmet load and capacity shortage. The explication regarding the reduction of green house gas emissions from this system is another important issue.
- All the ins and outs of wind energy conversion systems have been elucidated with a set of empirical expressions. The generators have been described solely by d-q reference frame. The Simulink-SimPower models of WECS have been simulated with different wind speeds to compute the energy produced by them and power curves have been validated by comparing them with that provided by the manufacturers.
- The hydrogen systems, composed of electrolyzer, storage tanks, hydrogen engines and generators, have been modeled and simulated in order to determine their characteristics. The hydrogen engine model differs from the conventional internal combustion engine in terms of applications and operating performance. Modeling and simulation of this device is therefore another success of this research as the results

from the simulation match with information found in manufacturer specification sheets. Mechanical powers from the engine and electrical powers from the generator corresponding to the hydrogen flow rates coming out from the tank were found consistent with the manufacturer data and confirm the validity of the presented model.

- Finally the transient behavior of each component has been determined for a number of probable conditions. For instance, during first ten seconds in the simulation the energy outputs from the WECS have been analyzed with variable load and variable wind speed conditions. From 11 second to 20 second, it is assumed that some surplus energy is available after meeting the load which manipulates the water electrolysis and stores the hydrogen in the tank. During 21 second to 25 second both the electrolyzer and the hydrogen generators are surmised to be in non-operating condition and hence the hydrogen tank pressure remains invariant. After that period as there is some increment of load occurs, the hydrogen generators would come into operation in conjunction with the WECS and the diesel generator. The 26^{th} and 27^{th} second of the simulation interpret this dynamics.

6.3 Conclusions

Long term operational point of view reveals that a power system with hydrogen storage runs more efficiently and economically than that without any storage system. This statement has been proved true in the discussions of Chapter 2 also. Therefore it is viable to incorporate the electrolyzer, tank and gensets to the existing power system. There

might have some contingency of discrepancy in simulation results as in Matlab the combined system was run for a few seconds to limit unnecessary delay. But this has been overcome by choosing appropriate values of the coefficients used in empirical expressions. In order to make the proposed system more practical, a 446.25 kW dump load has been introduced which is controlled by an eight bit binary signal to control the step change of the load. However, this component plays an important role in system stability.

A number of transformers have employed to match the generated voltage with the local grid potential. For each asynchronous generator a capacitor bank was also found to ensure the reactive power for its own excitation. System control in a smaller extent has been accomplished by using some switches and breakers in the Simulink-SimPower model. Apart from measuring the energy production from the generators, their operating speeds have also been monitored and observed almost accurate as desired. The simulation results in Chapter 5 speak in favor of the successfulness, certainty and precision of the proposed model. Although this system has been designed in the perspective of Ramea community, but this infrastructure can also be adapted in other remote territories with minor modifications.

6.4 Future Works

- This research does not show the permanent magnet generator modeling as there is lack of information regarding power electronic control mechanisms. The converter-

inverter set and their proper control can assist to attain the successful simulation model.

- Although this research employs some extent of control during modeling of wind energy conversion systems, but does not aim at precise control of the whole power system of Ramea. The energy generation from the components was computed without controlling. It is possible to set the threshold for these components and accomplish better results.
- The hydrogen tanks have been contemplated as the storage medium of the Ramea power system. Besides this, flywheel and pumped hydro are some of the worthwhile means of energy storage. Those techniques could be studied thoroughly, modeled appropriately and their comparative discussions are left open.
- The sizing of power system components was beyond the scope of this research, but the proposed model can be the basis of designing the systems for other isolated communities depending on resource availability such as wind, solar, hydro etc.
- Thirty second simulation time is really small to comprehend all the transient characteristics of the constituents of this power system. Some competitive software might be put to use for a longer duration of simulation to obtain better results.
- The simulation results in Chapter 5 reveal that a significant amount of energy is consumed by the secondary load. This energy along with the exhaust heat from the power system could be reused in different purposes like water heating, room heating etc. However this approach would increase system efficiency as well. Further research might aim at investigating these important issues.

References

[1] http://www.darvill.clara.net/altenerg/fossil.htm

[2] http://www.canwea.ca/windvision_e.php

[3] Morel Oprisan, "Introduction of Hydrogen Technologies to Ramea Island", IEA Wind-KWEA Joint Workshop, April, 2007.

[4] James Glennie, "Wind-Diesel Project", WEICan for Carl Brothers P.Eng, Frontier Power Systems, International Wind-Diesel Workshop, April 23-25, 2008.

[5] RETScreen International "Case Study: Isolated Island Community/Newfoundland, Canada" URL: www.retscreen.net

[6] http://www.windatlas.ca/en/index.php

[7] Shuhui Li and Timothy A. Haskew, "Transient and Steady-State Simulation Study of Decoupled d-q Vector Control in PWM Converter of Variable Speed Wind Turbines", The 33rd Annual Conference of the IEEE Industrial Electronics Society (IECON), pp. 2079-2086, November 5-8, 2007, Taipei, Taiwan.

[8] Feng Wu, Xiao-Ping Zhang and Ping Ju, "Modeling and Control of the Wind Turbine with the Direct Drive Permanent Magnet Generator Integrated to Power Grid", DPRT2008, pp. 57-60, 6-9 April, 2008, Nanjing China.

[9] T. Tafticht, K. Agbossou, A. Chériti and M.L. Doumbia, "Output Power Maximization of a Permanent Magnet Synchronous Generator Based Stand-alone Wind Turbine", IEEE ISIE 2006, pp. 2412-2416, July 9-12, 2006, Montreal, Quebec, Canada.

[10] Md. Arifujjaman, M. Tariq Iqbal, John E. Quaicoe and M. Jahangir Khan, "MODELING AND CONTROL OF A SMALL WIND TURBINE", CCECE/CCGEI, Saskatoon, pp. 778-781, May 2005.

[11] Xibo Yuan, Fred Wang, Rolando Burgos, Yongdong Li and Dushan Boroyevich, "Dc-link Voltage Control of Full Power Converter for Wind Generator Operating in Weak Grid Systems", This work made use of ERC Shared Facilities supported by the National Science Foundation under Award Number EEC-9731677, Applied Power Electronics Conference and Exposition, pp. 761-767, Feb 24-28, 2008.

[12] Bogdan S. Borowy and Ziyad M. Salameh, "Dynamic Response of a Stand-Alone Wind Energy Conversion System with Battery Energy Storage to a Wind Gust", IEEE Transactions on Energy Conversion, Vol. 12, No. 1, pp. 73-78, March 1997.

[13] Shuhui Li and Tim A. Haskew, "Characteristic Study of Vector-Controlled Direct Driven Permanent Magnet Synchronous Generator in Wind Power Generation", Power and Energy Society General Meeting – Conversion and Delivery of Electrical Energy in the 21st Century, 2008 IEEE, pp. 1-9, July 20-24, 2008.

[14] Anca D. Hansen and Gabriele Michalke, "Modelling and Control of Variable-speed Multi-pole Permanent Magnet Synchronous Generator Wind Turbine", WIND ENERGY, Wind Energ. 2008, 11:537–554, Published online 12 May 2008 in Wiley Interscience. (www.interscience.wiley.com) DOI: 10.1002/we.278.

[15] Loraind Szabo, Kairoly Agoston Biro, Cosmina Nicula and Florin Jurca, "Simulation of Wind Turbine Driven Autonomous Squirrel Cage Induction Generators", INES 2007 - 11th International Conference on Intelligent Engineering Systems - 29 June - 1 July 2007 - Budapest, Hungary, pp. 213-218.

[16] Emilio J. Bueno, Santiago Cobreces, Francisco J. Rodriguez, Alvaro Hernandez and Felipe Espinosa, "Design of a Back-to-Back NPC Converter Interface for Wind Turbines With Squirrel-Cage Induction Generator", IEEE TRANSACTIONS ON ENERGY CONVERSION, VOL. 23, NO. 3, PP. 932-945, SEPTEMBER 2008.

[17] Yuri Ulianov Lopez and Jose Antonio Dominguez Navarro, "Small Signal Stability Analysis of Wind Turbines with Squirrel Cage Induction Generators", IEEE conference 2008.

[18] Alexander Hamlyn, Helen Cheung, Lin Wang, Cungang Yang and Richard Cheung, "Adaptive Protection and Control Strategy for Interfacing Wind-Power Electricity Generators to Distribution Grids", IEEE conference 2008, pp. 1-8.

[19] T. Aboul-Seoud and A. M. Sharaf, "A Novel Dynamic Voltage Regulator Compensation Scheme for a Standalone Village Electricity Wind Energy Conversion System", IEEE conference 2009, pp. 117-121.

[20] R. Jayashri and R.P. Kumudini Devi, "Effect of tuned unified power flow controller to mitigate the rotor speed instability of fixed-speed wind turbines", Renewable Energy, 34 (2009), pp. 591–596.

[21] Tarek Ahmed, Osamu Noro, Eiji Hiraki and Mutsuo Nakaoka, "Terminal Voltage Regulation Characteristics by Static Var Compensator for a Three-Phase Self-Excited Induction Generator", IEEE TRANSACTIONS ON INDUSTRY APPLICATIONS, VOL. 40, NO. 4, PP. 978-988, JULY/AUGUST 2004.

[22] D.A. Bechrakis, E.J. McKeogh and P.D. Gallagher, "Simulation and operational assessment for a small autonomous wind–hydrogen energy system", Energy Conversion and Management, 47 (2006), pp. 46–59.

[23] S.R. Vosen and J.O. Keller, "Hybrid energy storage systems for stand-alone electric power systems: optimization of system performance and cost through control strategies", International Journal of Hydrogen Energy, 24 (1999), pp. 1139-1156.

[24] Mohammad Saad Alam and David W. Gao, "Modeling and Analysis of a Wind/PV/Fuel Cell Hybrid Power System in HOMER", Second IEEE Conference on Industrial Electronics and Applications, 2007, pp. 1594-1599.

[25] Kodjo Agbossou, Mamadou L. Doumbia and Adil Anouar, "Optimal Hydrogen Production in a Stand-Alone Renewable Energy System", Industry Applications Conference, Oct 2-6, 2005, 40th IAS Annual Meeting, vol. 4, pp. 2932-2936.

[26] Tomonobu Senjyu, Eitaro Omine, Daisuke Hayashi, Hideomi Sekine and Toshihisa Funabashi, "Application of Decentralized Control for Remote Power System Stabilization by Installing Renewable Energy Power Plant", IEEJ Trans 2008, vol 3, pp. 473–481.

[27] M.J. Khan and M.T. Iqbal, "Dynamic modeling and simulation of a small wind–fuel cell hybrid energy system", Renewable Energy, vol. 30, 2005, pp. 421–439.

[28] Vincenzo Cataliotti, Giorgio Graditi and Giuseppe Scrivano, "Preliminary Tests On A Miniaturized Hybrid Pv-Pemfc System", IEEE Conference, 2007, pp. 736-740.

[29] Guillaume Doucet, Claude Etievant, Christophe Puyenchet, Serguey Grigorievb and Pierre Millet, "Hydrogen-based PEM auxiliary power unit", INTERNATIONAL JOURNAL OF HY DROGEN ENERGY, Vol. 34 (2009), pp. 4983–4989.

[30] Th.F. El-Shatter, M.N. Eskandar and M.T. El-Hagry, "Hybrid PV/fuel cell system design and simulation", Renewable Energy, 27 (2002), pp. 479–485.

[31] Haluk Görgün, "Dynamic modelling of a proton exchange membrane (PEM) electrolyzer", International Journal of Hydrogen Energy, 31 (2006), pp. 29–38.

[32] Munich Airport Sustainability Report 2008.

URL: http://www.munich-airport.de/sustainability

[33] Øystein Ulleberg, "Modeling of advanced alkaline electrolyzers: a system simulation approach", International Journal of Hydrogen Energy, 28 (2003), pp. 21–33.

[34] Hung-Cheng Chen, Jian-Cong Qiu and Chia-Hao Liu, "Dynamic Modeling and Simulation of Renewable Energy Based Hybrid Power Systems", DRPT2008, 6-9 April, 2008, Nanjing Chaina, pp. 2803-2809.

[35] A. Bilodeau and K. Agbossou, "Control analysis of renewable energy system with hydrogen storage for residential applications", Journal of Power Sources, 162 (2006), pp. 757–764.

[36] M. Uzunoglu, O.C. Onar and M.S. Alam, "Modeling, control and simulation of a PV/FC/UC based hybrid power generation system for stand-alone applications", Renewable Energy, 34 (2009), pp. 509–520.

[37] Chun-Hua Li, Xin-Jian Zhu, Guang-Yi Cao, Sheng Sui and Ming-Ruo Hu, "Dynamic modeling and sizing optimization of stand-alone photo voltaic power systems using hybrid energy storage technology", Renewable Energy, 34 (2009), pp. 815–826.

[38] Mamadou Lamine Doumbia, Kodjo Agbossou and Évelyne Granger, "Simulink Modelling and Simulation of a Hydrogen Based Photovoltaic/Wind Energy System", EUROCON 2007, The International Conference on "Computer as a Tool", Warsaw, September 9-12, pp. 2067-2072.

[39] R. Chedid, F. B. Chaaban and R. Shihab, "A Simplified Electric Circuit Model for the Analysis of Hybrid Wind-Fuel Cell Systems", Power Engineering Society General Meeting 2007, IEEE, Tampa, FL, June 24-28, 2007, pp. 1-6.

[40] O.C. Onar, M. Uzunoglu and M.S. Alam, "Dynamic modeling, design and simulation of a wind/fuel cell/ultra-capacitor-based hybrid power generation system", Journal of Power Sources, 161 (2006), pp. 707–722.

[41] S. Kelouwani, K. Agbossou and R. Chahine, "Model for energy conversion in renewable energy system with hydrogen storage", Journal of Power Sources, 140 (2005), pp. 392–399.

[42] James D. Maclay, Jacob Brouwer and G. Scott Samuelsen, "Dynamic analyses of regenerative fuel cell power for potential use in renewable residential applications", International Journal of Hydrogen Energy, 31 (2006), pp. 994–1009.

[43] M.T. Iqbal, "Simulation of a small wind fuel cell hybrid energy system", Renewable Energy, 28 (2003), pp. 511–522.

[44] Alejandro J. del Real, Alicia Arce and Carlos Bordons, "Hybrid Model Predictive Control of a Two–Generator Power Plant Integrating Photovoltaic Panels and a Fuel Cell", 46th IEEE Conference on Decision and Control, New Orleans, LA, USA, Dec. 12-14, 2007, pp. 5447-5452.

[45] https://analysis.nrel.gov/homer

[46] http://www.nlh.nl.ca

[47] J. Cotrell and W. Pratt, "Modeling the Feasibility of Using Fuel Cells and Hydrogen Internal Combustion Engines in Remote Renewable Energy Systems", National Renewable Energy Laboratory (NREL), 1617 Cole Boulevard, Golden, Colorado 80401-3393, September 2003. URL: http://www.osti.gov/bridge

[48] http://www.fallingrain.com/world/CA/05/Ramea.html

[49] John Flynn, "Ramea Wind-Hydrogen-Diesel Project", NECEC Conference, November 2007, 180 Holiday Inn, Portugal Cove Road, St. John's, Newfoundland, Canada.

[50] http://en.wikipedia.org/wiki/Ramea,_Newfoundland_and_Labrador

[51] http://maps.google.ca

[52] Siegfried Heier, "Grid Integration of Wind Energy Conversion Systems", John Wiley & Sons Ltd., Baffins Lane, Chichester, West Sussex, England, ISBN: 047197143X, 1998.

[53] Erich Hau, "Wind turbines: Fundamentals, Technologies, Application, Economics", Springer Verlag Berlin Heidelberg New York, ISBN: 3-540-57064-0, 2000.

[54] Northern Power Systems, 29 Pitman Road, Barre, VT 05641, United States.
URL: www.northernpower.com

[55] Frontier Power Systems, Attn: Carl Brothers, 392 Church Street, Alberton, PEI C0B 1B0, Canada. Email: carl.brothers@pei.sympatico.ca

[56] S.N. Bhadra, D. Kastha, S. Banerjee, "Wind Electrical Systems", Oxford University Press, YMCA Library Building, Jai Singh Road, New Delhi 110001, ISBN-10: 0-19-567093-0, 2005.

[57] MATLAB/SIMULINK and MATLAB/SimPower Systems are the products of The MathWorks, 3 Apple Hill Drive, Natick, MA 01760-2098, USA.
URL: http://www.mathworks.com

[58] Mohd. Abdus Salam, "Fundamentals of Electric Machines", Alpha Science International Ltd., 7200 The Quorum, Oxford Business Park North, Garsington Road, Oxford, OX4 2JZ, U.K., ISBN: 1-84265-275-3, 2005.

[59] Seyoum, D., Rahman, M.F. and Grantham, C., "Terminal voltage control of a wind turbine driven isolated induction generator using stator oriented field control," Proceedings of the Eighteenth Annual IEEE Applied Power Electronics Conference and Exposition (APEC '03), Miami Beach (FL, USA), vol. 2, 2003, pp. 846-852.

[60] Hydrogenics Canada, 5985 McLaughlin Road, Mississauga, ON, Canada L5R 1B8.

[61] Licht, Stuart, "Solar Hydrogen Generation: Toward a Renewable Energy Future", Springer, 2008, ISBN: 978-0-387-72809-4.

[62] J.M. Vidueira, A. Contrerasa, T.N. Veziroglu, "PV autonomous installation to produce hydrogen via electrolysis, and its use in FC buses", International Journal of Hydrogen Energy, pp. 927– 937, 28 (2003).

[63] Keliang Zhou, J.A. Ferreira, S.W.H. de Haan, "Optimal energy management strategy and system sizing method for stand-alone photovoltaic-hydrogen systems", INTERNATIONAL JOURNAL OF HYDROGEN ENERGY, pp. 477 – 489, 33 (2008).

[64] Gerhard Peharz, Frank Dimroth, UrsulaWittstadt, "Solar hydrogen production bywater splitting with a conversion efficiency of 18%", International Journal of Hydrogen Energy, pp. 3248 – 3252, 32 (2007).

[65] D.A. Bechrakis, E.J. McKeogh, P.D. Gallagher, "Simulation and operational assessment for a small autonomous wind–hydrogen energy system", Energy Conversion and Management, pp. 46–59, 47 (2006).

[66] Kodjo Agbossou, Mohanlal Kolhe, Jean Hamelin, and Tapan K. Bose, "Performance of a Stand-Alone Renewable Energy System Based on Energy Storage as Hydrogen", IEEE TRANSACTIONS ON ENERGY CONVERSION, pp. 633-640, VOL. 19, NO. 3, SEPTEMBER 2004.

[67] Zhou K, Ferreira J.A, De Haan S.W.H, "Optimal energy management strategy and system sizing method for stand-alone photo voltaic-hydrogen systems. Int. J. Hydrogen Energy 2008, volume 33, pp. 477–89.

[68] Bergen A, Schmeister T, Pitt L, Rowe N, Djilali N, Wild P, "Development of a dynamic regenerative fuel cell system", J. Power Sources 2007, volume 164, pp. 624-630.

[69] Bockris JO'M, "Hydrogen economy in the future", Int. J. Hydrogen Energy 1999, volume 24, pp. 1–15.

[70] Momirlan M, Veziroglu TN, "Current status of hydrogen energy", Energy Rev. 2002, volume 6, pp. 141-179.

[71] Sherif SA, Barbir F, Veziroglu TN, "Wind energy and the hydrogen economy-review of the technology", Sol Energy 2005, volume 78, pp. 647-660.

[72] Gandıa LM, Oroz R, Ursua A, Sanchis P, Dieguez PM, "Renewable hydrogen production: performance of an alkaline water electrolyzer working under emulated wind conditions", Energy & Fuels 2007, volume 21, pp. 1699–1706.

[73] Hydrogen Engine Center Incorporation, 2502 E Poplar Street, Algona, IA 50511, USA. URL: http://www.hydrogenenginecenter.com

[74] Anupam Gangopadhyay, Peter Meckl, "Modeling and Validation of a Lean Burn Natural Gas Engine", Journal of Dynamic Systems, Measurement, and Control, Vol. 123, pp. 425-430, September 2001.

[75] "Safe Use of Hydrogen and Hydrogen Systems", NASA Training Center, 2006.

[76] Chee-Mun Ong, "Dynamic Simulation of Electric Machinery Using Matlab/ Simulink", Prentice Hall, One lake Street, Upper Saddle River, New Jersey 07458, USA, 1998, ISBN: 0-13-723785-5.

[77] Ray Hunter and George Elliot, "Wind-Diesel Systems: A Guide to the Technology and its Implementation", Cambridge University Press, 1994, The Pitt Building, Trumpington Street, Cambridge, CB2 1RP.

[78] Hussein Ibrahim, Adrian Ilinca, Rafic Younès, Jean Perron and Tammam Basbous, "Study of a Hybrid Wind-Diesel System with Compressed Air Energy Storage", IEEE Canada, Electrical Power Conference 2007, Renewable and Alternative Energy Resources, EPC2007, Montreal, Canada, October 25-26, 2007.

Appendix A

Simulink and SimPower Subsystem Blocks

This Appendix comprises of a number of Simulink and SimPower subsystem blocks which are the illustration of corresponding blocks in Chapter 3, Chapter 4 and Chapter 5. Most of the input and output parameters are denoted by the similar symbols as expressed in those chapters. It is important to note that, some of the inputs are linked with the preceding blocks and rests are constant values or coefficients. In order to provide a better idea about the subsystem blocks, the corresponding units are also given in the diagrams.

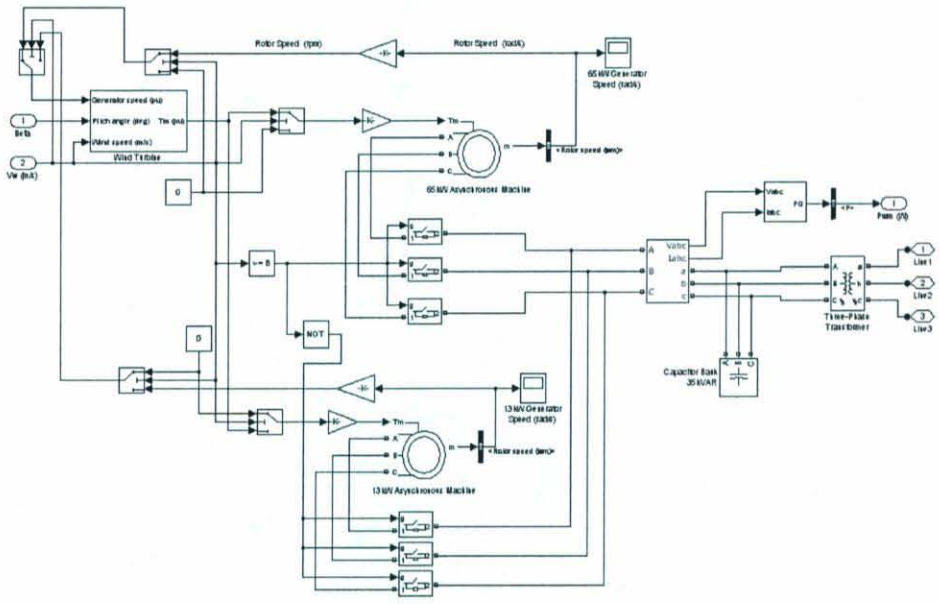

Figure A.1: Subsystem 'SS: WM15S Model'

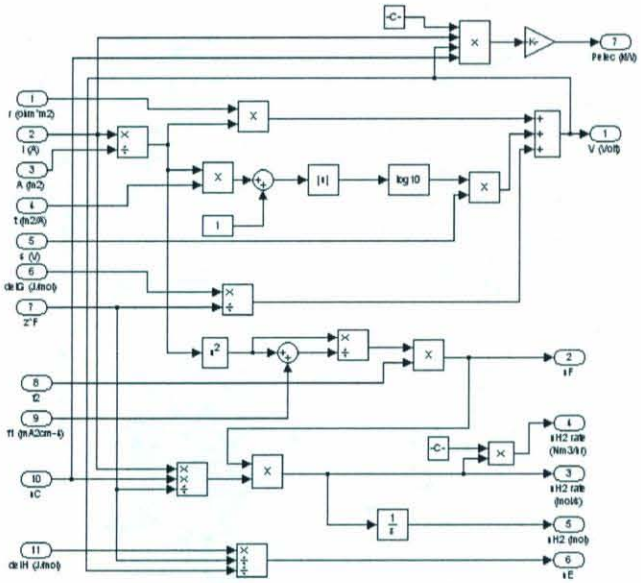

Figure A.2: Subsystem 'SS: Electro-chemical Model of the Electrolyzer'

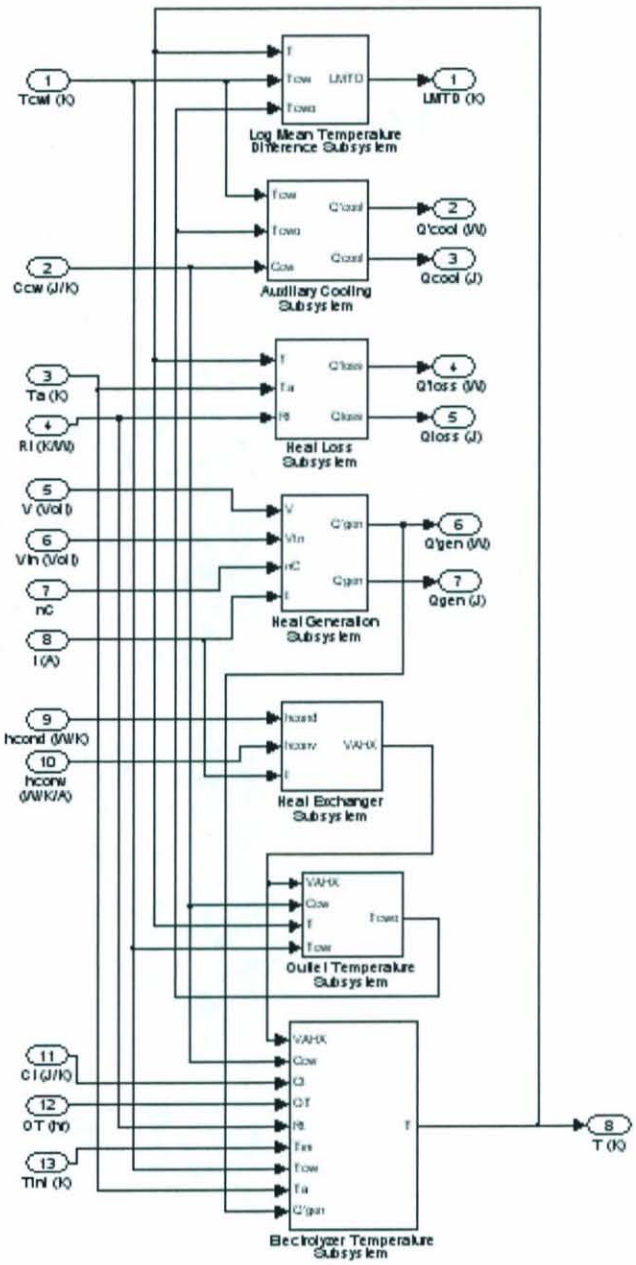

Figure A.3: Subsystem 'SS: Thermal Model of the Electrolyzer'

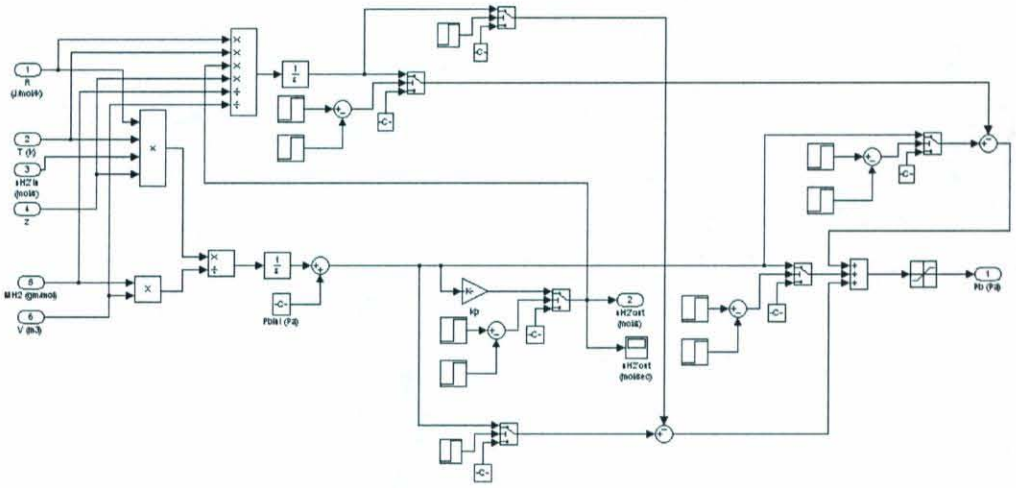

Figure A.4: Subsystem 'SS: Hydrogen Tank'

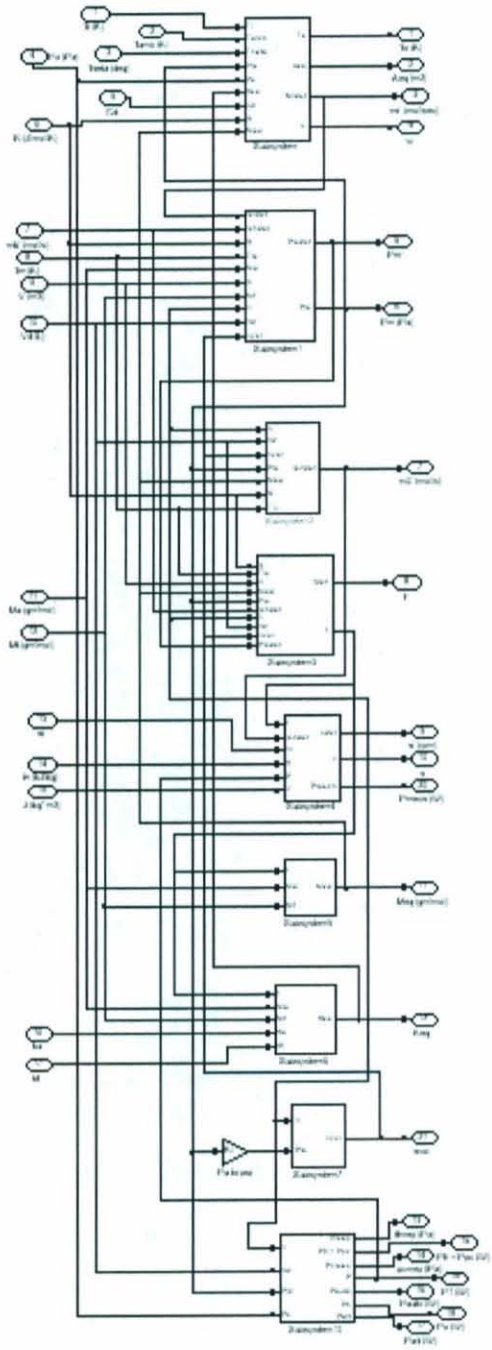

Figure A.5: Subsystem 'SS: Hydrogen Engine'

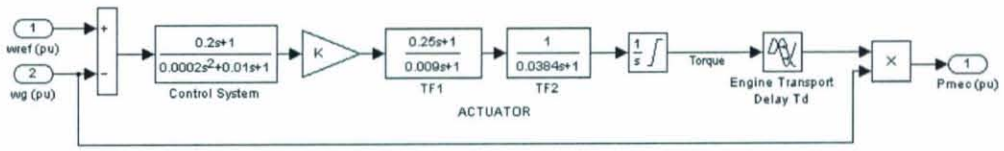

Figure A.6: Subsystem 'SS: Diesel Engine'

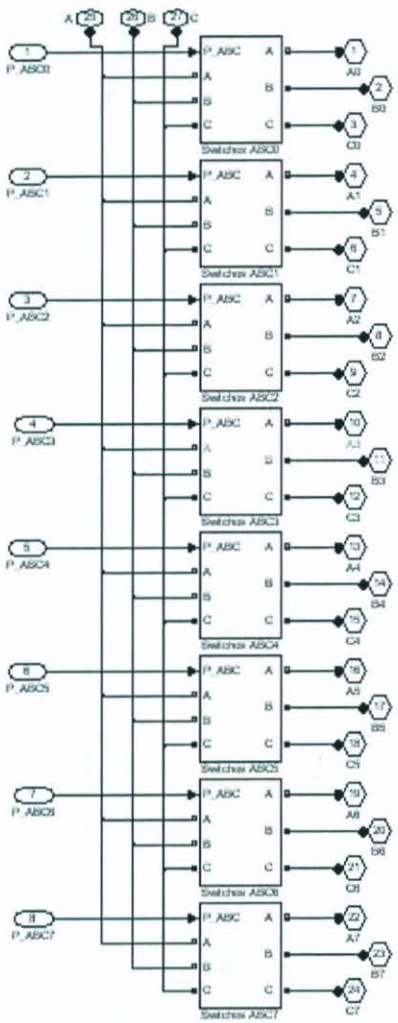

Figure A.7: Subsystem 'SS: Secondary Load Switch'

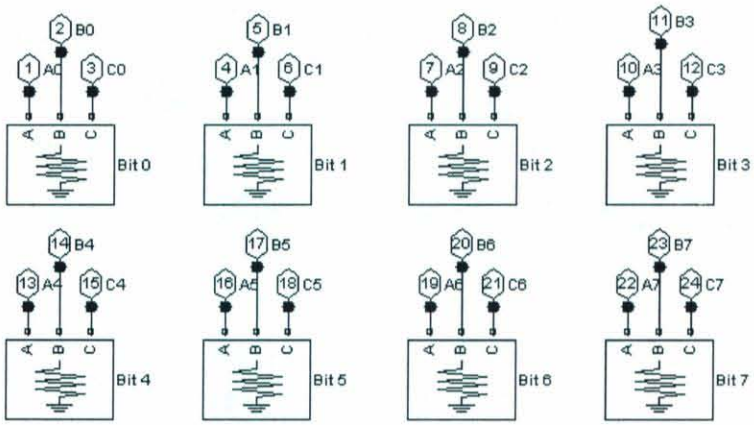

Figure A.8: Subsystem 'SS: Secondary Resistive Load'

Appendix B

List of Research Papers

In this Appendix some conference, poster and journal papers are enlisted which have been written during this masters program. The first two are conference papers; Paper 1 and 2 have been published and presented in IEEE conferences and Paper 3 is soon going to be presented. The fourth one is the journal paper which will be submitted shortly.

Paper 1 Md. Maruf-ul-Karim and M.T. Iqbal, "Dynamic Modeling and Simulation of Alkaline Type Electrolyzers", presented at 22nd Canadian Conference on Electrical and Computer Engineering 2009, May 3-6, Delta St. John's, St. John's, NL, Canada.

Paper 2 Md. Maruf-ul-Karim and M.T. Iqbal, "Dynamic Modeling and Simulation of a Remote Wind-Diesel-Hydrogen Hybrid Power System", presented at Electrical Power and Energy Conference 2010, August 25-27, Halifax, NS, Canada.

Paper 3 Md. Maruf-ul-Karim and M.T. Iqbal, "Simulation and Dynamic Modeling of an Isolated Wind-Diesel-Hydrogen based Hybrid Energy System", will be presented in WESNet Student Poster Session and Competition, Tuesday November 2, 2010, Montreal, Quebec, Canada.

Paper 4 Md. Maruf-ul-Karim and M.T. Iqbal, "Dynamic Modeling and Simulation of an Isolated Wind-Diesel-Hydrogen based Hybrid Power System", will be submitted for Journal publication in Renewable Energy, September 2010.